LBL-8948

Lawrence Berkeley Laboratory
UNIVERSITY OF CALIFORNIA, BERKELEY, CA

Materials & Molecular
Research Division

STUDIES OF ELECTRON CORRELATION IN THE PHOTOIONIZATION PROCESS

Richard Allen Rosenberg
(Ph. D. thesis)

March 1979

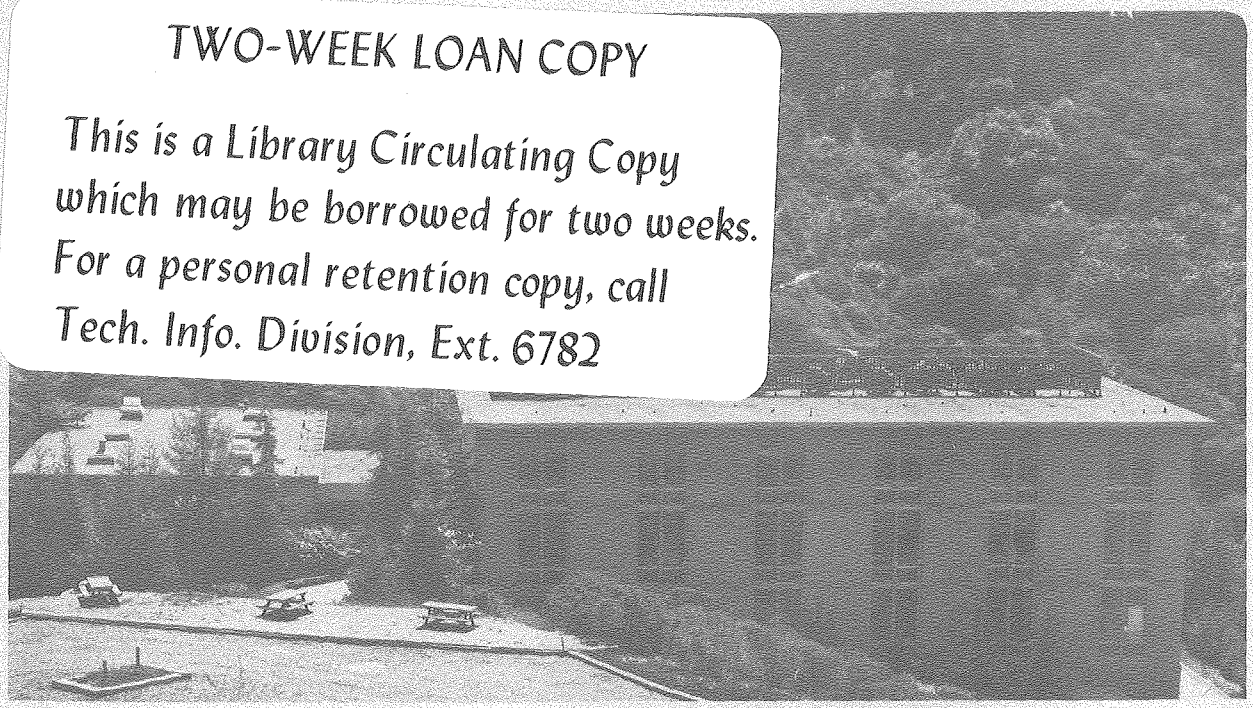

Prepared for the U. S. Department of Energy
under Contract W-7405-ENG-47

DISCLAIMER

STUDIES OF ELECTRON CORRELATION IN THE PHOTOIONIZATION PROCESS

Contents

STUDIES OF ELECTRON CORRELATION IN THE PHOTOIONIZATION PROCESS

Richard Allen Rosenberg

ABSTRACT

Electron correlation is a result of the interaction of two or more electrons confined in a region of space, and may conveniently be treated under the formalism of configuration interaction (CI). Photoionization provides a rather direct experimental method for studying configuration interaction. The types of CI involved in the photoionization process can be divided into three categories: initial state configuration interaction (ISCI), final ionic state configuration interaction (FISCI), and continuum state configuration interaction (CSCI). This thesis deals with experimental studies which reveal how the various types of CI may become manifested in photoionization.

The experimental methods utilized in this work are photoelectron spectroscopy (PES), electron impact spectroscopy (EIS), and time-resolved fluorescence spectroscopy. The EIS was carried out following the discovery that the UV lamp on a Perkin-Elmer photoelectron spectrometer could be utilized as a source of low energy electrons. The time-resolved fluorescence work utilized both the tunability and the time structure of the radiation available at the Stanford Synchrotron Radiation Laboratory (SSRL). A commercial photoelectron spectrometer equipped with a conventional UV lamp (HeI, NeI) was employed for some

of the PES studies, and a novel time-of-flight photoelectron spectrometer was developed for the PES work performed using synchrotron radiation.

The PES of Ba, Sm, Eu, and Yb was studied using both HeI (22.22 eV) and NeI (16.85 eV) radiation. Satellite structure observed in these spectra using NeI (and for Yb, HeI also) radiation could be satisfactorily explained by ISCI alone. The HeI spectra of Sm, Eu, and, in particular, Ba showed dramatic changes in the satellite population which could only be explained by a new mechanism, autoionization, which is a special form of CSCI. The detailed nature of this mechanism was explored in Ba using synchrotron radiation. It was found that the autoionizing level decays preferentially via an Auger type mechanism.

Further insight into autoionization was gained in the electron impact/ejected electron spectra of Ba ($5p^6 6s^2$) and Yb ($5p^6 4f^{14} 6s^2$). It was found that autoionizing levels excited <u>above</u> the first $(5p)^{-1}$ threshold decay primarily in a two-step Auger process, leading to a relatively large number of doubly charged ions. For autoionizing states below the $(5p)^{-1}$ limit, decay appears to go to ground and excited states of the singly charged ion.

The first experimental determination of the lifetime of the XeII $5s5p^6\ ^2S_{1/2}$ state yielded a value of 34.4(6) nsec. Reasonable agreement with theory could only be reached by including both FISCI and relativistic effects in calculating the lifetime.

I. INTRODUCTION

Ionization takes an atom or molecule from an initial state, consisting of N bound electrons, to an N-electron final state, where one or more of the electrons is free. Characterization of the ionization process is therefore very sensitive to the detailed nature of the wave functions describing the initial state, ψ_i, and final state, ψ_f. In particular both ψ_i and ψ_f may be influenced by electron-electron correlation, i.e. the correlated motion of two or more electrons confined in a region of space.

In the "independent particle" model such effects are not accounted for and the wave functions are described by properly antisymmetrized products of one-electron orbitals. This is known as the Hartree-Fock approximation. One way to deal with electron correlation while still retaining the use of the Hartree-Fock orbitals is the method known as "Configuration Interaction" (CI). The effect of electron-electron repulsion is dealt with by allowing additional configurations to become mixed with the primary state. Thus, the actual wave function is written as a linear combination of all possible configurations of the same symmetry, i.e. $\psi^m = \sum_j C_j^m \phi_j$. In most cases, one of the C_j^m will be near unity, giving rise to what is called the main configuration.

Manson[1] has broken down the CI process in photoionization into three categories: Initial State Configuration Interaction (ISCI), Final Ionic State Configuration Interaction (FISCI), and Continuum State Configuration Interaction (CSCI). In ISCI and FISCI, the mixing occurs among all <u>bound</u> orbitals of the same symmetry; as such, they are usually amenable

to calculations.[2] In CSCI, the ionized electron is coupled to the core configuration to give the proper symmetry (as determined by dipole selection rules) and then the mixing is done. This process is much more difficult to calculate and has only been performed for the simplest of systems. CSCI effects are normally not important for photon energies much above threshold (>100eV).

When a discrete level imbedded in the continuum is excited, that level may interact with the continuum, leading to the ejection of one or more electrons; this process is known as autoionization. Autoionization is a particular form of CSCI that has dramatic effects on the photoionization process. In particular, the autoionization level may interact strongly with certain final states, thus drastically altering their partial cross-sections.

Numerous methods exist for studying the photoionization process, including photoabsorption spectroscopy, photoionization mass spectroscopy, photoionization fluorescence spectroscopy, electron impact spectroscopy, and photoelectron spectroscopy (PES). This thesis includes work done utilizing the latter three techniques. The motivation for these studies was to examine how the different types of CI become manifested in the photoionization process.

Of all the techniques, PES is probably the most sensitive to effects of electron correlation. If monochromatized light with energy $h\nu$ interacts with a sample, it may ionize that sample, giving off an electron with kinetic energy, K.E. given by the well known Einstein relationship:

$$K.E. = h\nu - B.E. \qquad (2)$$

where B.E is the binding energy of the electron corresponding to a specific final state of the ion, i.e.

$$B.E.= \langle \psi_f | \mathcal{H} | \psi_f \rangle - \langle \psi_i | \mathcal{H} | \psi_i \rangle \qquad (3)$$

where $\mathcal{H}$ is the Hamiltonian of the system. In PES, the number of electrons is scanned as a function of K.E.; peaks appear at energies corresponding to different final states of the ion. The matrix element governing this process is in the dipole approximation, $\langle \psi_i | \bar{r} | \psi_f \rangle$. By examination of the relative intensities in the PES spectrum, one may come to definite conclusions regarding the extent of CI in ψ_i and ψ_f.

As mentioned earlier, autoionizing resonances cause dramatic variations in the peak intensities. Ideally, one would like a photon source which could be tuned to each of these resonances. With the advent of synchrotron radiation, this has now become possible and much of the work included here utilizes this light source. However, these experiments are inherently difficult due to the low signals encountered in these experiments and the necessity for doing them away from the laboratory in a limited amount of time. A complementary method for studying autoionization is by electron impact/ejected electron spectroscopy. Excitation is done via electron impact and peaks will appear for electrons with kinetic energies given by

$$K.E - E_a - E_f \qquad (4)$$

Here E_a is the energy of the autoionizing level and E_f is the energy of the final ionic state. Due to the continuous nature of the electron source employed in this work, it is not possible to determine how much energy has gone into excitation. An additional complication comes from the use of low energy electrons which vitiates the dipole selection rules

utilized in photoabsorption. However, through a detailed analysis of the ejected electron spectrum one may reach definite conclusions regarding both the symmetry and the decay channels of the autoioizing level.

If an atom is ionized and left in an excited state (ψe), that level may decay to a lower ionic state (ψe) through emission of a photon. By monitoring the time dependence of this fluorescence, it is possible to determine the lifetime of the excited state. The lifetime is given by

$$\tau^{-1} = \sum_{\ell} A_{e\ell} \tag{5}$$

where $A_{e\ell} \alpha \langle \psi_e | \bar{r} | \psi_\ell \rangle^2$ and the summation is over all lower levels. Although not as direct as PES, such measurements do yield information on the composition of the ionic states and on the degree to which FISCI is a factor. This is especially apparent when such measurements are interpreted in light of information obtained from PES and theoretical calculations. In particular, the lifetime is sensitive only to FISCI, while the cross-sections observed in PES contain contributions from both ISCI and FISCI.[2]

ISCI has been found to be important in the PES of the alkaline earths, Ca, Sr, Ba[3] (nominal configuration ns^2) as revealed through the existence of "satellite lines". The origin of these lines is easily understood if we note that the "exact" initial state wave function can be written as

$$\psi_i = c_1 |ns^2\rangle + c_2 |(n-1)d^2\rangle + c_3 |np^2\rangle + \tag{6}$$

where n=4, 5, and 6 for Ca, Sr, and Ba respectively. Satellite peaks

arise for each admixed configuration, with intensities roughly proportional to the c_i^2 modulated by the partial photoionization cross-section. Chapter III deals with the analogous phenomena observed in Sm, Eu, and Yb using NeI (16.67/16.85eV) radiation and the autoionization observed in Ba, Sm, and Eu due to resonant excitation by HeI (21.22 eV) radiation.

Chapter IV discusses effects of FISCI in conjunction with the lifetime of the XeII ($5s5p^6\ ^2S_{1/2}$) state. In addition, relativistic effects are found to play a major role in the description of this state.

Through the use of synchrotron radiation, it is possible to selectively excite different autoionizing levels. This procedure was utilized to study autoionization in Ba, and the resulting spectra and decay mechanisms are discussed in Chapter V.

Chapter VI presents the ejected electron spectra of Ba and Yb. These complex spectra are analyzed using mechanisms proposed to explain the PES spectra of Ba in chapters III and V.

The next chapter is devoted to the experimental details of this work. It will concentrate on those aspects of the experiments on which I have been a major contributor and which are not presented elsewhere.

REFERENCES

1. S. T. Manson, J. Electron Spectrosc. and Rel. Phen., 9, 21 (1976)

2. R. L. Martin, Ph.D. Thesis, University of California, LBL-5167 (1976)

3. S. Süzer, S. T. Lee, and D. A. Shirley, Phys. Rev. A, 13, 1842 (1976)

II. EXPERIMENTAL

A. History

No description of the experimental apparati utilized in this work would be complete without some mention of the background behind it. The intent of this section is to provide the reader with the proper perspective to follow the experimental developments. In addition, much of the work was done at the Stanford Synchrotron Radiation Laboratory (SSRL) located at the storage ring SPEAR. This section should also give a feeling for what it's like to do gas-phase UV experiments at SSRL, while trying to meet what often seemed like vague and arbitrary regulations of the SSRL and SPEAR staffs.

I first became interested in studying electron correlation in the Fall of 1975 when I collaborated with Drs. Shuit-Tong Lee and Sefik Süzer in experiments with Ba, Sm, Eu, and Yb[1] (Ch. III). The aspect of these studies that really fascinated me was the dramatic change in the spectra brought about by autoionization at HeI (21.22 eV) as compared to NeI (16.67/16.85 eV) radiation. During that period, we also discovered that our glow discharge lamp could be used as a low energy electron impact source[2] (next section). Although this work shed new light in many areas, it was apparent that the frontier in this field lay with the use of synchrotron radiation. Only by use of a tunable photon source could the type of autoionization seen in Ba at HeI be systematically explored. At that time I did not think this was a realistic possibility during my graduate career.

The following winter a visiting scientist, Dr. Eckart Matthias, with the help of Erwin Poliakoff, initiated a program of time-resolved

spectroscopy of gases at SSRL, the ultimate goal being to observe quantum beats in the fluorescence. Upon passing my preliminary exams in April, I became fully involved in these studies with the intent of learning and participating in some very interesting science while gaining the necessary experience to establish a gas phase PES program at SSRL.

The solid state portion of our group had been involved with PES experiments at SSRL for several years. Gas phase spectroscopy is inherently more difficult due to the relatively high ($>10^{-6}$ torr) pressure involved, which must somehow be isolated from the ultra-high vacuum (UHV $\sim 10^{-9}$ torr) of the beam line, and the lower counting rates. The initial experiments utilized a 1 mm thick LiF window to separate the UHV and experimental chamber. The chamber itself was pumped by "clean" pumps, i.e. a cryo-pump/ion pump arrangement. Our first confrontation with the SSRL/SPEAR bureaucracy came that summer (1976) when we requested permission to substitute a trapped diffusion pump for the ion pump. It was only then that the vacuum staff became aware of the gaseous nature of our experiments. After much ado, we were finally granted permission to use the diffusion pump; this ultimately led to the measurement of excited state lifetimes in Kr and Xe[3] and the successful observation of quantum beats[4] in the fall of 1976. We also began experiments on the Xe excimer system.

During this period Mike White, who was also interested in establishing a PES program at SSRL, joined our little gas phase cadre. We realized the next step in this venture would be an extension of the usable energy range of the 8° line. Use of a LiF window restricted us to energies less than 11.8 eV. There were two possible ways of achieving higher energies:

1. A differentially pumped system, consisting of two regions separated by capillaries and pumped by turbomolecular pumps (TMP's).
2. Use of thin (∿1500Å) metallic windows, in particular, Aℓ ($h\nu > 17$eV) and In ($12 < h\nu < 17$eV).

We chose the latter alternative, because it was a less radical change for the SPEAR/SSRL staff to adjust to and seemed achievable in a reasonable length of time.[5] We therefore began designing the system and submitted an equipment modification proposal in early 1977, aiming for implementation during a three-week May run. After several meetings, our apparatus was approved and a testing procedure established. One contingency of this approval was that the entire apparatus be electropolished before use. Since the first two weeks of the run were devoted to LiF experiments, this meant having a spare apparatus ready and disassembly and assembly of the entire structure during the run. An additional complication was caused by there being only three people involved in this run and we were trying a varied number of projects; by the time the switch-over to the Al window system arrived, we were already quite drained. We managed to meet all the requirements and successfully implemented the apparatus by measuring the lifetime of the $B^2\Sigma_u^+$ state of N_2^+.

With this barrier overcome, we decided to tackle PES of gases. Based on our timing experience, we decided to take advantage of the timing properties of SPEAR again and build a time-of-flight (TOF) electron analyzer. By the following fall we had a preliminary design for a chamber which we hoped could eventually contain two (or three) TOF analyzers,

to simultaneously measure the angular distribution of the electrons. The chamber was also designed to accommodate a commercial cylindrical mirror analyzer (CMA) in the unhappy event that the TOF system proved unworkable.

With the assistance of Dick Escobales in mechanical engineering and George Gabor for electrical design, work went fairly smoothly. One major snag was caused by the two turbo-molecular pumps (TMP) needed for the relatively heavy gas load. Our first choice for these was the Alcatel 450 ℓ/sec air-bearing TMP which had previously been used by R.Z. Bachrach at SSRL; they were oil-free and required no forepump. Unfortunately, the delivery date kept getting pushed further and further back, until finally it was apparent they weren't coming. A suitable replacement was needed quickly. We found that the Airco-Temescal 500 ℓ/sec TMP could be delivered on time. Unfortunately, this pump required oil for its bearings and a forepump; therefore, we had to persuade the vacuum people that it was safe for use on the beam lines. After several days of testing and considering the Al window to be a fairly effective conduction barrier, they agreed to let us try them on our TOF run in June (1978). I should also note that none or our equipment is ever "officially approved"; we are only given tacit consent to use it.

In the meantime, research in other areas was moving forward. We had begun studies of photodissociation of XeF_2 and ICN. Mike and I were continuing laboratory work on the PES of the non-volatile IV-VI compounds.[6] In the fall (1977) run we completed our studies on Xe_2, which included the use of monochromatized fluorescence for the first time.[7] Also, at this time, using the Al window system, we made the first measure-

ment of the lifetime of the XeII $5s5p^6\ ^2S_{\frac{1}{2}}^8$ state. This was an important measurement in its own right; however, what I was really looking for was to see if a slowly moving electron, produced just above threshold, could influence the lifetime of a state. This is similar to the post-collisional interaction (PCI) which has been observed in autoionization and Auger decay. Unfortunately, no definite effect was observed, but the experiment was far from rigorous. In the future, I hope to be able to do a more definitive experiment.

Construction, assembly, and testing of the TOF apparatus continued to go well. In fact, we were ready several weeks prior to our mid-June run. The run itself went better than expected. The resolution of the analyzer was roughly what we predicted and the counting rates were much higher. The only flaw came when we discovered that the transmission was oddly peaked around 2 eV kinetic energy electrons. Later, we realized this was caused by the drift tube being constructed out of μ-metal, which tended to concentrate magnetic field lines near the interaction region. For the November (1978) run, this was modified so the drift tube was made out of aluminum and a coaxial μ metal cylinder provided the magnetic shielding.

About midway through this two-week run, (June) we learned that we could have an additional week of beam time, a week after the run ended. I decided that this could be a golden opportunity to try to study the autoionization in Ba and the lanthanides. During the week between the two runs, I modified a Perkin-Elmer type oven (this oven will be described in the following section) into an effusive beam source. The last two

days of the run were to be devoted to this venture, and it didn't work. There were two reasons for this:

1. The oven produced thousands of background counts caused by thermal electrons; these were uncorrelated in time and completely swamped the spectrum.
2. The Perkin-Elmer oven was wound non-inductively around the slit; this is not the case for electrons produced near the edges, as they were in the effusive beam source.

In addition, the beam was so uncollimated that metal was sprayed everywhere - one of our viewpoints became a vacuum deposited Yb mirror! I determined to correct these deficiencies by the next run (November, 1978).

The problem of inductive effects was solved by using a non-inductively wound heater cable, which was suggested by Jim Pollard and Dennis Trevor. To improve our resolution, we planned to utilize a retarding grid; this would also take care of the thermal electrons. In the event that this wasn't ready in time, the oven was designed so that it could be floated at a positive potential and trap the thermal electrons. Collination of the beam was achieved by the use of a micro-capillary array directed at a liquid-nitrogen cooled cold finger.

During laboratory tests of the apparatus, a set of detector channel plates became unstable; this was attributed to contamination by Ba vapor. Also, a TMP became fouled at this time. We thought the Ba vapor might be responsible for this, but it seemed unlikely since the pump was situated far from the oven and at right angles to it. Two heater coils were also burned out during the testing. This was caused by the temperature

vs. power curves given for the heater cables were intended to be applied to use in air; much less power was required in vacuum.

Almost too late, we discovered that our conjecture of Ba contamination of the TMP was correct - this occurred with the second pump two days into the run. Thus, we were left without any pumps. In desperation, we attached our 60 ℓ/sec ion pump and the 30 ℓ/sec ion pump from the SSRL pump stand to the chamber. Although this arrangement considerably lengthened the pump-down time, the experiments were now possible. As a result, the spectra presented in Chapter V were obtained and my fantasy of using synchrotron radiation to explore the autoionization in Ba had become a reality.

Obtaining a Ph.D. in science is much more than just Introduction, Experimental, Results, Discussion, and Conclusion. I hope the preceding section illustrated some of these intangibles. The next sections will encompass the more basic aspects of the experimental work.

REFERENCES

1. S.-T. Lee, S. Süzer, E. Matthias, R. A. Rosenberg, and D. A. Shirley, J. Chem. Phys. 66, 2496 (1976)

2. S.-T. Lee, R. A. Rosenberg, E. Matthias, and D. A. Shirley, J. Electron Spec. and Rel. Phen., 10, 203 (1977)

3. E. Matthias, R. A. Rosenberg, E. D. Poliokoff, M. G. White, S.-T. Lee, and D. A. Shirley, Chem. Phys. Lett., 52, 239 (1977)

4. E. Matthias, M. G. White, E. D. Poliokoff, R. A. Rosenberg, S.-T. Lee, and D. A. Shirley, Chem. Phys. Lett., 54, 30 (1978)

5. Only this past fall has a proposal for a differentially pumped beam line been approved. It is still at least a year away, though.

6. M. G. White, R. A. Rosenberg, S.-T. Lee, and D. A. Shirley, to be published, J. Electron Spec. and Rel. Phen.

7. G. Thornton, E. D. Poliakoff, E. Matthias, S. H. Southworth, R. A. Rosenberg, M. G. White, and D. A. Shirley, to be published J. Chem Phys.

8. R. A. Rosenberg, M. G. White, E. D. Poliakoff, G. Thornton, and D. A. Shirley, J. Phys. B. 11, L719 (1978)

B. Laboratory Experiments

1. Photoelectron Spectroscopy of High Temperature Vapors

The highly modified model PS-18 Perkin-Elmer Photoelectron Spectrometer utilized in this work has been described in detail previously[1], so only a brief description will be given here. The spectrometer and associated electronics are shown schematically in Figures 1 and 2 respectively. Metallic samples are vaporized in a non-inductively wound boron nitride oven (Fig. 3). Electrons produced by ionization of the vapor by HeI or NeI radiation are energy analyzed by a 127° cylindrical analyzer. Voltage to the analyzer is supplied by a digital addresser and counts corresponding to each voltage (kinetic energy) are stored in the appropriate address of a multi-channel analyzer (MCA). The information stored in the MCA is then transferred to magnetic tape and data reduction is done via the lab's CDC 7600 computer.

REFERENCES

1. Sefik Süzer, Ph.D. Thesis, University of California, LBL-4922 (1976).

FIGURE CAPTIONS

Fig. 1. Schematics of the PS-18 Spectrometer.

Fig. 2. Schematics of the Digital Data Collection of the PS-18 Spectrometer.

Fig. 3. Schematic of the oven and ionization chamber.

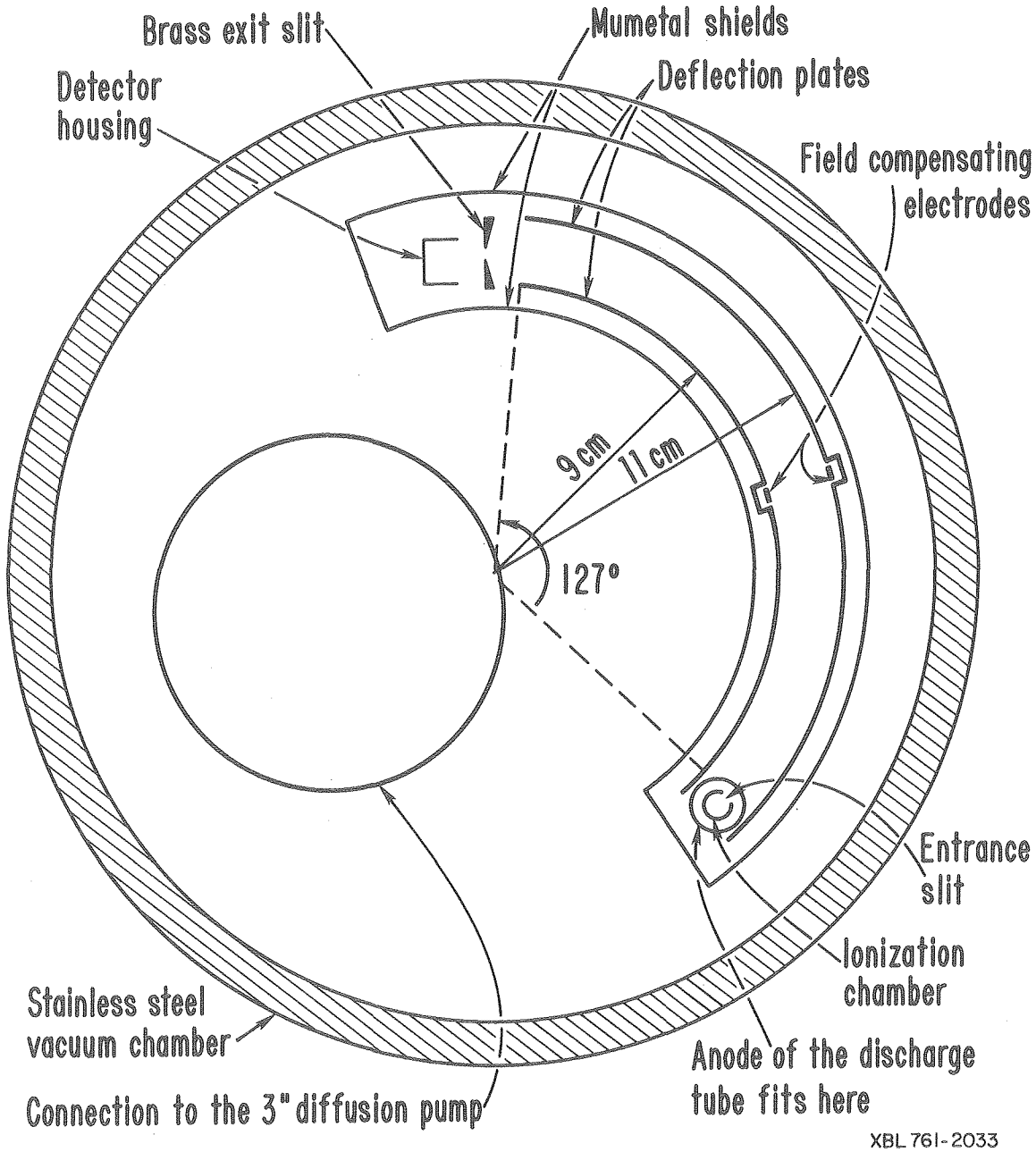
Brass exit slit
Mumetal shields
Detector housing
Deflection plates
Field compensating electrodes
9 cm
11 cm
127°
Entrance slit
Ionization chamber
Stainless steel vacuum chamber
Anode of the discharge tube fits here
Connection to the 3" diffusion pump
XBL 761-2033

Fig. 1

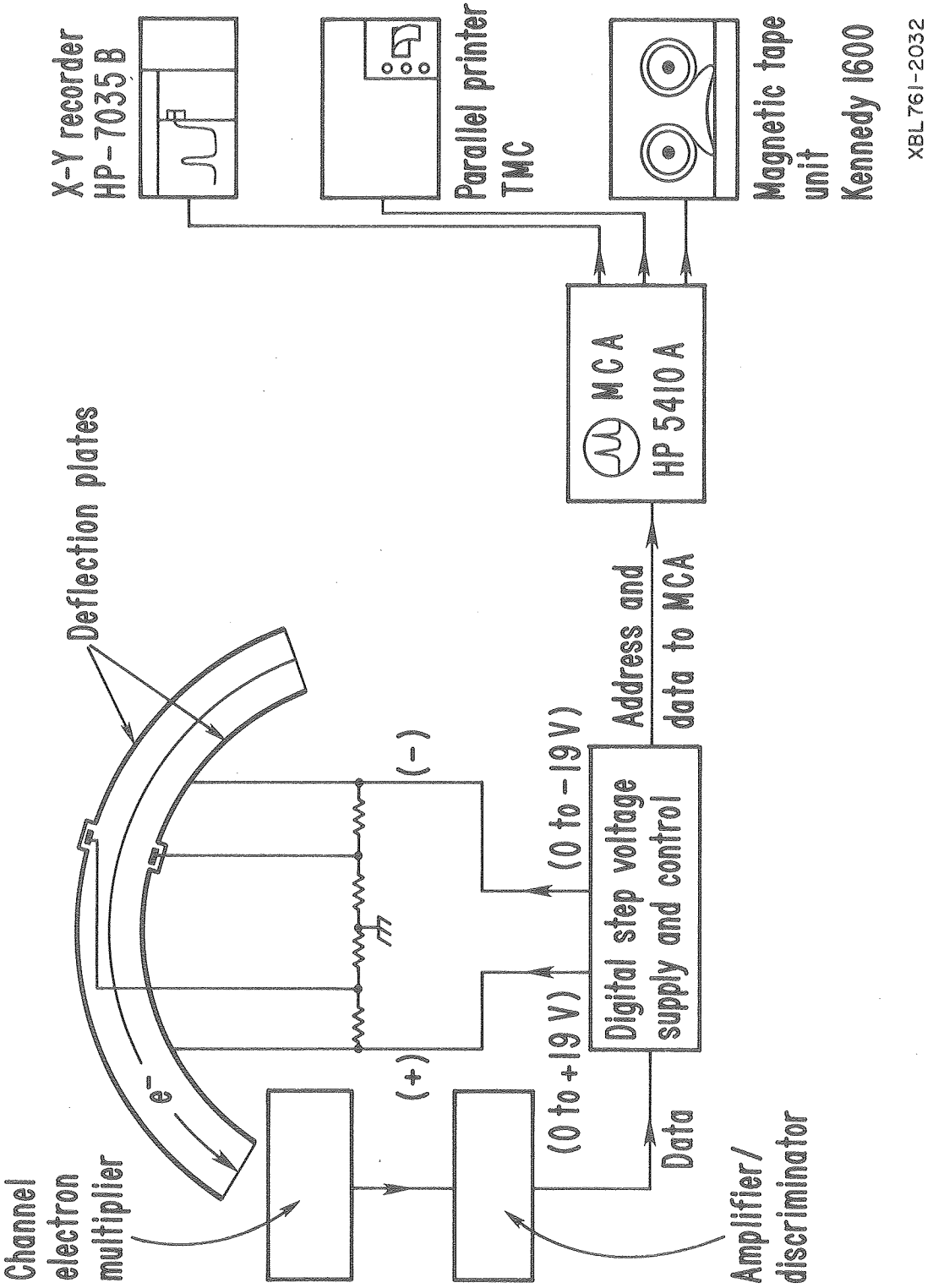

XBL761-2032

Fig. 2

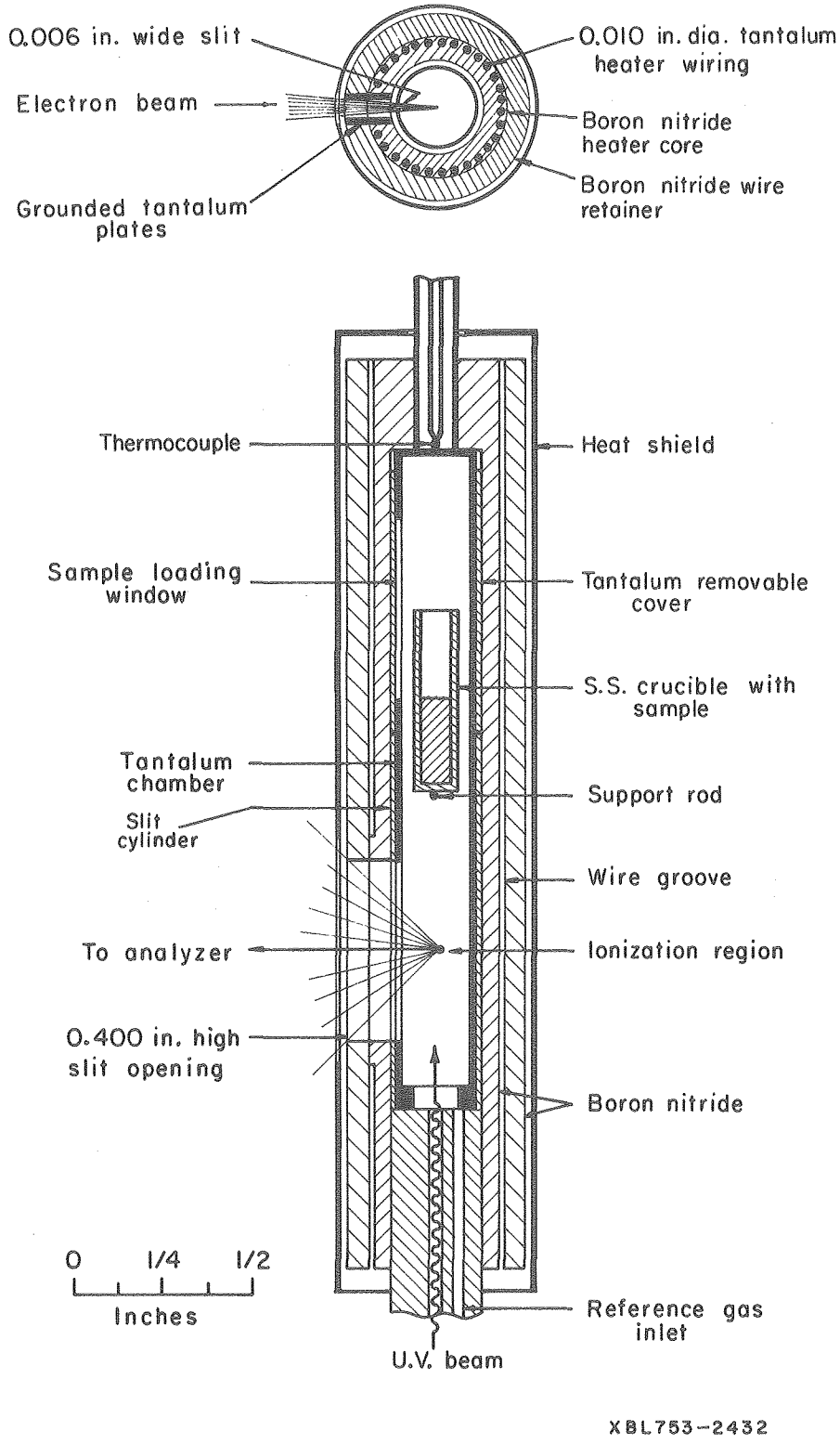
0.006 in. wide slit
Electron beam
Grounded tantalum plates
0.010 in. dia. tantalum heater wiring
Boron nitride heater core
Boron nitride wire retainer
Thermocouple
Heat shield
Sample loading window
Tantalum removable cover
S.S. crucible with sample
Tantalum chamber
Support rod
Slit cylinder
Wire groove
To analyzer
Ionization region
0.400 in. high slit opening
Boron nitride
0 1/4 1/2
Inches
Reference gas inlet
U.V. beam
XBL753-2432

Fig. 3

2. Electron Impact Studies

The electron impact work utilized the same spectrometer described in the previous section. The only modification was based on the discovery that when the discharge lamp was operated at sufficiently low pressures, it could be utilized as a relatively intense source of low energy electrons. The following section details the characteristics of this source.*

a. Introduction

Electron impact spectroscopy utilizes hot filament guns as source of electrons. The electrons generated in this way are quite monochromatic with an inherent energy spread of the order of the thermal energy (kT). Thus an electron beam of width less than 0.5 eV is readily obtainable. This bandwidth is important for electron loss impact studies in which a high flux of monochromatic electrons is required. However, in certain areas of electron impact studies in which the role of electrons is in excitation or ionization, it is not necessary for the electrons to be monochromatic. The ejected electron spectroscopy of autoionizing and Auger processes[1] falls in this latter category.

It is well known that the plasma of any gas discharge provides a copious source of electrons. The energy of the electrons in the plasma follows a Maxwellian distribution,[2] with a mean energy rarely exceeding one-third of the first ionization potential of the gas involved. These characteristics of the electron plasma have led to its use as a high flux electron gun in high pressure CO_2 lasers.[3,4] It seems possible

---

*This section was published previously with co-authors S.-T. Lee, E. Matthias, and D. A. Shirley, J. Electron Spec. and Rel. Phen., 10, 203 (1977).

that the electron plasma can be used as an electron source in ejected electron spectroscopy as well. We have found this to be the case, and in this paper, some preliminary results will be presented about the use of a cold cathode plasma electron gun in electron impact studies.

Ejected electron spectroscopy following electron impact detects electrons of discrete energies and, as a consequence, the monochromatic electrons can easily be distinguished from the abundant continuous background. Electrons ejected from autoionizing states or Auger transitions satisfy this condition, and can therefore be detected and studied with broad-band electron sources. In Auger, work, ionization by electrons rather than photons is frequently preferred because a higher flux of electrons is more readily obtainable and the energy of the exciting source can be varied at will to maximize cross sections. In the study of autoionization processes, excitation by (especially low energy) electron impact is employed to take further advantage of the less stringent selection rules. Consequently, autoionizing states may be observed corresponding to optically forbidden transitions.

Ejected electron spectra of several metal atomic vapors, excited by electron impact using filament emission, have recently been reported. The list includes the alkali metals Na,[5] K,[6] Rb,[7] and Cs,[8] and the Group II element Mg[9] and Cd.[10] The study of free atoms is fundamental and appealing, because direct comparison with theory is possible. There are two immediate complications involved in the study of metal vapors. Firstly, an oven is required to maintain the required vapor pressure. Secondly, the metal vapors are generally detrimental to the

hot filaments. A special high-temperature oven developed in this laboratory[11] has enabled us to heat our samples up to $\sim 800^{\circ}$ C. By employing a cold cathode plasma electron gun, we have circumvented the second complication. In this paper, we present spectra of Na and K obtained by utilizing this new method, and compare them with those obtained by a conventional electron gun.

b. Experimental

The experiments were carried out with a Perkin-Elmer PS-18 photoelectron spectrometer modified for high temperature work.[11,12] Except for the operation of the discharge lamp, the spectrometer was used in exactly the same manner as for the measurement of photoelectron spectra.

The PS-18 spectrometer uses a D.C. high-voltage cold cathode capillary discharge for generating HeI or other atomic resonance radiation. The cross-sectional view of the lamp is shown in Fig. 1. The upper end of the capillary in the lamp is about 10 cm below the entrance slit of the 127° cylindrical electron analyzer. When the lamp is operated to produce HeI radiation, a pressure of 200 - 500 microns is used. In this pressure range electrons from the discharge plasma cannot reach the entrance slit because of inelastic collisions. Maintaining this condition is mandatory in PES work, because electrons from the lamp can increase the noise level and lower the quality of the photoelectron spectra. In contrast, to operate the lamp as an electron gun, the plasma was intentionally diluted to increase the mean free path of the electrons and enable them to enter the ionization chamber. This was accomplished by lowering the pressure in the discharge while monitoring the background electron counts. By adjusting the pressure, an optimum condition for signal-to-background

ratio, signal intensity and resolution in the ejected electron spectrum can usually be obtained. Depending upon the cleanliness and exact geometry of the lamp and the sample used, the helium lamp was found to operate as an electron gun in the pressure range of 25 - 150 microns, with a discharge current of ca. 50 ma.

For lamp pressures in an intermediate range, both the ejected electron and photoelectron spectra can be obtained simultaneously, and the relative intensities of the two spectra can be varied with pressure. Thus the calibration of the ejected electron spectra can usually be accomplished by referring to the known energies of photoelectron signals of the samples. Where necessary, additional calibration gases such as Xe, Kr, N_2, etc. can also be used. The ejected electron spectra to be presented later were normally recorded with the photoelectron signals completely suppressed. In the following, we shall distinguish between low-pressure and high-pressure discharges as electron and photon modes of the lamp, respectively.

c. Performance of the Plasma Electron Gun

The characteristics of the cold cathode plasma and its potential as a source for electron impact studies are exemplified by the following measurements, in which our spectra are compared to those obtained using hot filament electron guns.

i. Low Energy Auger Spectra of Xe and Kr

Figure 2 shows the $N_{4,5}00$ Auger spectra of Xe recorded using five different plasma discharges operated in the electron mode. In Figure 3 the $M_{4,5}NN$ Auger spectrum of Kr obtained with the He lamp is displayed. Included for comparison in both figures are the corresponding spectra reported by Werme et al.,[13] who used a filament electron gun. The fact

that identical electron spectra of Xe were obtained, irrespective of the gases in the lamps, is expected because only the electron plasmas are responsible for the excitation of the spectra. Among the five lamps tested (He, Ne, Ar, H_2, and N_2), the helium lamp was consistently more stable, and it gave spectra of better signal-to-background ratio. The superiority of the helium discharge may be generally attributed to helium having the highest ionization potential and the lowest inelastic cross sections, among the five gases,[14] for electrons with energy in the range of 0 - 10^3 eV, which covers the energy distribution of the plasma electrons. Consequently, the helium lamp can be operated in the electron mode at the highest pressure,[15] while delivering the plasma with the largest mean energy.[1] For these reasons, the helium lamp was used for all subsequent studies.

Comparison of our results with the spectra obtained by Werme et al.[13] (Fig. 2 and 3) shows that they are almost identical in the positions and relative intensities of the Auger peaks. Furthermore, the strong autoionization electron peaks lying between 8 - 10 eV in the Xe spectrum of Werme et al. also are present in all the spectra obtained by plasma electrons. Naturally, the spectra obtained by normal electron gun are much superior in signal-to-background ratio. The higher background in our spectra is mainly due to poor focusing of the electron plasma and immense scattering of electrons from the ionization chamber. The signals are much stronger in the electron plasma spectra which was partially achieved at the expense of resolution. Still larger signals can usually be obtained by lowering the pressure or increasing the current of the lamp as long as the discharge is stabilized.

ii. Electron Spectra of the Autoionizing States of K and Na

Figure 4 depicts the autoionization electron spectrum of K vapor at 220 ± 20° C. The kinetic energies of the observed peaks are set out in Table I, where the results of other workers are also included for comparison. The spectrum corresponds to the autoionizing states of K with a 3p-electron excited by electron impact. Similar spectra have been reported recently[6] using electron beams of energy 500 and 29 eV. Most of the states detected in the electron spectra have also been observed in the 3p absorption spectrum of K.[16] Because of the lower resolution in the electron spectra, each electron line may actually correspond to several closely-spaced states observed optically, and in Table I only the prominent absorption peaks are listed along with the corresponding electron lines. The assignment of the individual autoionizing states have been discussed in detail by Mansfield.[16]

Our spectrum of K is remarkably similar in the energies of the observed peaks to the composite of the two spectra of Ottley and Ross,[6] excited by electron beams of 500 and 29 eV, respectively. The small difference in the number of peaks in previous and present spectra may be simply a consequence of a difference in energy resolution. The peaks numbered 4 - 8 in our spectra were observed to vary in intensities relative to the others in two separate runs, and in some spectra these peaks were hardly detectable. This intensity variation may be attributed to a difference in the energy distribution of the plasma as a result of a change in the condition of the lamp. This observation goes together with the fact that peaks 4 - 8 were detected with large intensities only following excitation by low energy electrons, and thus must be regarded as

optically forbidden transitions.[6,16] The broad peak 1 has not been reported before, but appeared to be present in Figure 1 of Reference 6. We have found that the intensity of this peak to increase with the temperature of the oven, and thus it is tentatively assigned to potassium dimer, K_2. With the binding energy of K_2 at 4.0 eV,[17] the excitation energy of this autoionizing state is 17.9 eV. The peaks labeled by I are the inelastic loss peaks of lines 2 and 3 corresponding to 4s → 4p excitation in K.

Figure 5 shows the autoionizing states in Na have been observed by photoabsorption[19,20] and projectile-electron spectroscopy.[21] The relevant results of these studies are also included in Table II for comparison. Except for peaks 1, 2, and 5 (see below), the spectrum of Na corresponds to the autoionizing states of Na following the excitation of a 2p electron. Peaks 3 and 4 are associated with the spin-orbit (s-o) doublets of the $2p^5 3s^2$ state of Na. The peaks between 28 and 30 eV are optically forbidden states of configuration $2p^5 3s3p$, observed previously only in Na^+-He-collisions.[21] Peaks above 30 eV have been observed in photoabsorption, and in this energy region there is a large number of closely-spaced lines in the absorption spectra which correspond to states of configuration $2p^5 3snd$, with $n \geq 3$.[19,20] Because of the limited resolution in our electron spectrum, each peak may actually be associated with several lines in the absorption spectrum.

The electron intensity around peaks 1 and 2 is due to $L_1L_{2,3}M_1$ Coster-Kronig transitions, i.e. $Na^+(2s2p^6 3s;\ ^{1,3}S) \rightarrow Na^{++}(2s^2 2p^5;\ ^2P_{1/2,3/2}) + 3$. This assignment is supported by the following energy

considerations. Using the equivalent-core approximation, the binding energy of the 3s-electron in the $2s2p^6 3s$ configuration of Na^+ can be equated to that of the 3s electron in the state $2s^2 2p^6 3s$ of Mg^+, which is 15.0 eV.[22] With $Na^{++}(2s2p^6)$ at 85.2 eV above the ground state of Na,[22] the 2s binding energy of Na is thus estimated to be 70.2 eV. With the configuration $2s^2 2p^5$ of Na^{++} at 52.5 eV,[22] the $L_1L_{2,2}M_1$ transition should then lie around 17.7 eV, which is close to the experimental value 18.7 eV. Furthermore, the observed half width, 0.7 eV, of peaks 1 and 2 is in accord with the energy spread expected from the contributions of the multiplet splitting of the $Na^+(2s2p^6 3s;\ ^{1,3}S)$ and the s-o splitting of $Na^{++}(2s^2 sp^5;\ ^2P_{1/2,3/2})$ states, which are 0.39 eV[23] and 0.17 eV[22] respectively. The electron intensity around peak 5 cannot be satisfactorily attributed to autoionizing states with the excitation of a 2p-electron. Again through energy consideration, it is tentatively assigned to the $L_1L_{2,3}N_1$ Coster-Kronig transition, i.e., $Na^+(2s2p^6 4s;\ ^{1,3}S) \rightarrow Na^{++}(2s^2 2p^5;\ ^2P_{1/2,3/2}) + e$. The energy difference between the $2s2p^6 4s$ and $2s^2 2p^6 3s$ configuration of Mg^+, which is 8.7 eV.[22] This value agrees reasonably well with the energy difference between peak 5 and the center of the peaks 1 and 2, i.e., 7.9 eV. The peaks designated I are attributed to inelastically scattered electrons resulting from the 3s → 3p transition in Na.

In the course of this work, a concurrent study of Na[9b] using 2 keV electrons and with much higher resolution came to our attention. Overall there is very good agreement between the two studies. Comparing the two spectra shows much larger relative intensities of peaks 6, 7, and 8 in our spectrum. This observation is consistent with the fact that these

peaks are associated with optically forbidden states and transitions to them are more probable by excitation with low energy electrons[6] found in the discharge plasma.

d. Discussion

As was pointed out earlier poor collimation and scattering from surfaces of the plasma electrons are partly responsible for the high background in the electron spectra. Also contributing to the background is the continuous energy distribution inherent in the plasma electrons, whose energies normally follow a Maxwellian distribution.[1] In addition, the maximum intensity of the background distribution in most of the spectra measured lies at around 5 - 6 eV, which is less than one-third of the binding energy of He as expected from earlier investigations.[1] In light of this and with the neglect of the difference in excitation cross sections the signal-to-background (S/B) ratio should become smaller as the energy of excitation increases, since a smaller fraction of the plasma electrons will have sufficient energy for excitation. This is indeed observed; the S/B ratio in the spectra deteriorates in the order K>Na>Xe>Kr, which is also the order of increasing energy of excitation. In the same context, the most energetic excitation so far observed is around 90 eV in the $M_{4,5}NN$ Auger spectrum of Kr. Another drawback of the electron source is that it needs careful tuning. Specifically, the pressure at which the electron mode is operable depends on the condition of the lamp, and so does the energy distribution of the electrons. This behavior probably derives from the nonreproducibility of electrode surfaces as a result of sputtering.

Despite these shortcomings, the plasma electrons do provide certain advantages over the conventional filaments. First, the plasma source shows very good resistance to poisoning. An immediate application of this property would be found in the study of reactive vapors, which are detrimental to filaments. We have used the discharge source to excite the autoionization electron spectra of Ca, Sr, Ba, and other high temperature metal vapors.[24] The use of filaments in these instances would have required considerable technical manipulations, such as differential pumping for the filaments, to alleviate the problem. Secondly, the electron mode of the lamp is much easier to operate than the filament electron gun, which usually requires an elaborate focusing lens system and clean vacuum conditions. A further merit of the lamp is its potential to produce higher currents.

The discharge lamp has so far been used only in its original design (see Fig. 1) to act as an electron source. It seems certain there is ample room for improvement. For instance, the background can be reduced considerably by better focusing of the electrons and directing the beam away from the sample holder.[25] Better focusing will have the additional bonus of increasing the usable portion of the plasma source. Finally, acceleration of the electrons may be used to study more energetic excitations.

e. Conclusions

It has been demonstrated that, with proper pressure conditions, the plasma in the D.C. capillary discharge of a UV lamp can be used as an electron source in electron impact studies, when monochromatic electrons

are not required. It seems reasonable to hold similar expectation for the plasma in other types of UV lamps. The present findings therefore establish the capacility of a molecular UV photoelectron spectrometer of also doing low energy electron impact studies of autoionization processes. We have made use of this capability in our Perkin-Elmer PS-18 spectrometer, and have studied a number of high temperature metal vapors.[24] In light of the present results, one should be cautious about the presence of autoionizing electron lines in the photoelectron spectra, especially of those compounds containing heavy elements, when recorded in a Perkin-Elmer spectrometer. It seems worthwhile pointing out that in the photoelectron spectra of Ca and Sr, autoionizing electrons have been detected with appreciable intensities with the He lamp operating at a pressure as high as 200 micron. On the other hand, it should prove very useful to study autoionization spectra in UV spectrometers simply by lowering the pressure.

References

1. In principle, Auger processes can be regarded as autoionization of an ion state. Thus there is no fundamental reason to separate the two. However, the term autoionization is generally reserved for the transition of a neutral state into the continuum. In this paper, we have, for the sake of simplicity, used autoionization to include Auger transitions as well.

2. K. T. Compton, Rev. Mod. Phys. 2, 123 (1930).

3. B. B. O'Brien, Appl. Phys. Lett. 23, 503 (1973).

4. R. G. Garnsworthy, L. E. S. Mathias, and C. H. H. Carmichael, Appl. Phys. Lett. 19, 506 (1971).

5. a) H. Hillig, B. Cleff, W. Mehlhorn, and W. Schmitz, Z. Physik 268, 225 (1974).

   b) E. Breuckmann, B. Breuckmann, W. Schmitz, and W. Mehlhorn, Abs. of contributed paper to the 2nd Int. Conf. on Inner Shell Ionization Phenomena, Freiburg, March/April 1976.

6. T. W. Ottley and K. J. Ross, J. Phys. B 8, L249 (1975).

7. K. J. Ross and T. W. Ottley, Phys. Letters 54A, 57 (1975).

8. K. J. Ross, W. R. Newell, T. W. Ottley, and S. H. Al-Shamma, J. Phys. B 8, L113 (1975).

9. a) B. Breuckmann and V. Schmidt, Z. Physik 268, 235 (1974).

   b) B. Breuckmann, V. Schmidt, and W. Schmitz, Abs. of contributed paper to the 2nd Int. Conf. on Inner Shell Ionization Phenomena, Freiburg, March/April 1976.

10. W. R. Newell, K. J. Ross, and J. B. Wickes, J. Phys. B 6, L337 (1973).

11. S. Süzer, M. S. Banna, and D. A. Shirley, J. Chem. Phys. 63, 3473 (1975).

12. a) S. Süzer, S.-T. Lee, and D. A. Shirley, Phys. Rev. A, 13, 1842 (1976).

    b) S. Süzer, S.-T. Lee, and D. A. Shirley, J. Chem. Phys. 65, 412 (1976).

13. L. O. Werme, T. Bergmark, and K. Siegbahn, Physica Scripta 6, 141 (1972).

14. L. J. Kieffer, Atomic Data 1, 19 (1969).

15. The pressure of the lamp is monitored by a thermocouple pressure gauge in the PS-18 spectrometer. Since the gauge has not been calibrated for the individual gases, the difference in our pressure readings had only qualitative significance.

16. M. W. D. Mansfield, Proc. R. Soc. Lond. A346, 539 (1975).

17. P. J. Foster, R. E. Lackenby, and E. J. Robbins, J. Phys. B 2, 478 (1969).

18. J. B. Mann, Los Alamos Scientific Report, LA 3691 (1968).

19. H. W. Wolff, K. Radler, B. Sonntag, and R. Haensel, Z. Physik 257 353 (1972).

20. J. P. Connerade, W. R. S. Garton, and M. W. D. Mansfield, the Astrophysical Journal 165, 203 (1971).

21. D. J. Pegg, H. H. Haselton, R. S. Thoe, P. M. Griffin, M. D. Brown, and I. A. Sellin, Phys. Rev. 12, 1330 (1975).

22. C. E. Moore, Natl. Bur. Stand. (U.S.) Circ. 467, Vol. 1 (1949).

23. To first approximation ^1S:^3S states would be split by $2G^2(2s, 3s)$ by Van Vleck's Theorem, Phys. Rev. 45, 405 (1934).

24. R. A. Rosenberg, et al., to be published.

25. In the present setup of the ionization chamber, the electron beam hits head-on with the bottom of the sample holder; see Ref. 11 for the diagram of the ionization chamber.

Table I. Kinetic Energies (eV) of the Peaks Observed in the Autoionization Electron Spectrum of K

Peak	This Work[a]	Ottley & Ross[b]		Mansfield[c]
		500 eV	29 eV	
1	13.90 (broad)			
2	14.38	14.38		14.383
3	14.66	14.64		14.640
4	15.44		15.43	15.419; 15.458
5	15.75			15.796
6	15.85	15.85	15.85	15.870
7	16.17	16.27	16.17	
8	16.46	16.36	16.36 16.46	
9	17.10	17.06 17.13	17.06	17.085
10	17.38		17.58	
11	17.75			
12	18.05	18.05	18.05	18.046; 18.075
13	18.40	18.38		18.389; 18.415
14	18.49	18.51		18.516; 18.616
15	18.96	18.94		18.945
		19.29		
		19.34		19.334
16	19.46	19.45 19.52		19.452; 19.455 19.497
17	19.66	19.62 19.70		19.619 19.707
18	19.98	20.04		20.034; 20.049

(continued)

Table I. (continued)

a) Experimental error is estimated to be ±0.05 eV. In the region between peaks 15 and 18, only the peak maxima are listed, though the intensity distribution suggests the presence of more than four peaks.

b) Ref. 6 gave spectra excited by electron beams of 500 eV and 29 eV.

c) Ref. 16; the kinetic energies listed are the excitation energies minus 4.339 eV, the 4s binding energy of K.

Table II. Kinetic Energies (eV) of the Peaks Observed in the Autoionization Electron Spectrum of Na

Peak	This Work[a]	Pegg et al[b]	Wolff et al[c]
1	18.47		
2	18.94		
3	25.63	25.63	25.630
4	25.80	25.86	25.796
5	26.64		
6	28.38	28.24	
7	28.80	28.76	
8	29.59	29.65	
9	30.70	30.66	30.630
10	30.99	30.96	30.991
11	31.54		
12	31.86	31.68	
13	32.25	32.2	
14	32.46	32.4	
15	32.79	33.0	

a) Experimental error is estimated to be ±0.05 eV.

b) Ref. 21

c) Ref. 19; the kinetic energies listed are the excitation energies minus 5.104 eV, the 3s binding energy of Na. There is a large number of closed spaced peaks observed in absorption in the energy region spanned by peaks 11 - 15, thus no entries are included here.

FIGURE CAPTIONS

Fig. 1. Schematic diagram of the discharge lamp.

Fig. 2. The $N_{4,5}00$ Auger spectra of Xe excited by electrons produced from hot filaments (a) and the plasmas of different discharge lamps as indicated (b) - (f).

Fig. 3. The $M_{4,5}NN$ Auger spectra of Kr excited by electrons produced from hot filaments (a) and the plasma of the He lamp (b).

Fig. 4. The autoionization electron spectrum of K vapor.

Fig. 5. The autoionization electron spectrum of Na vapor.

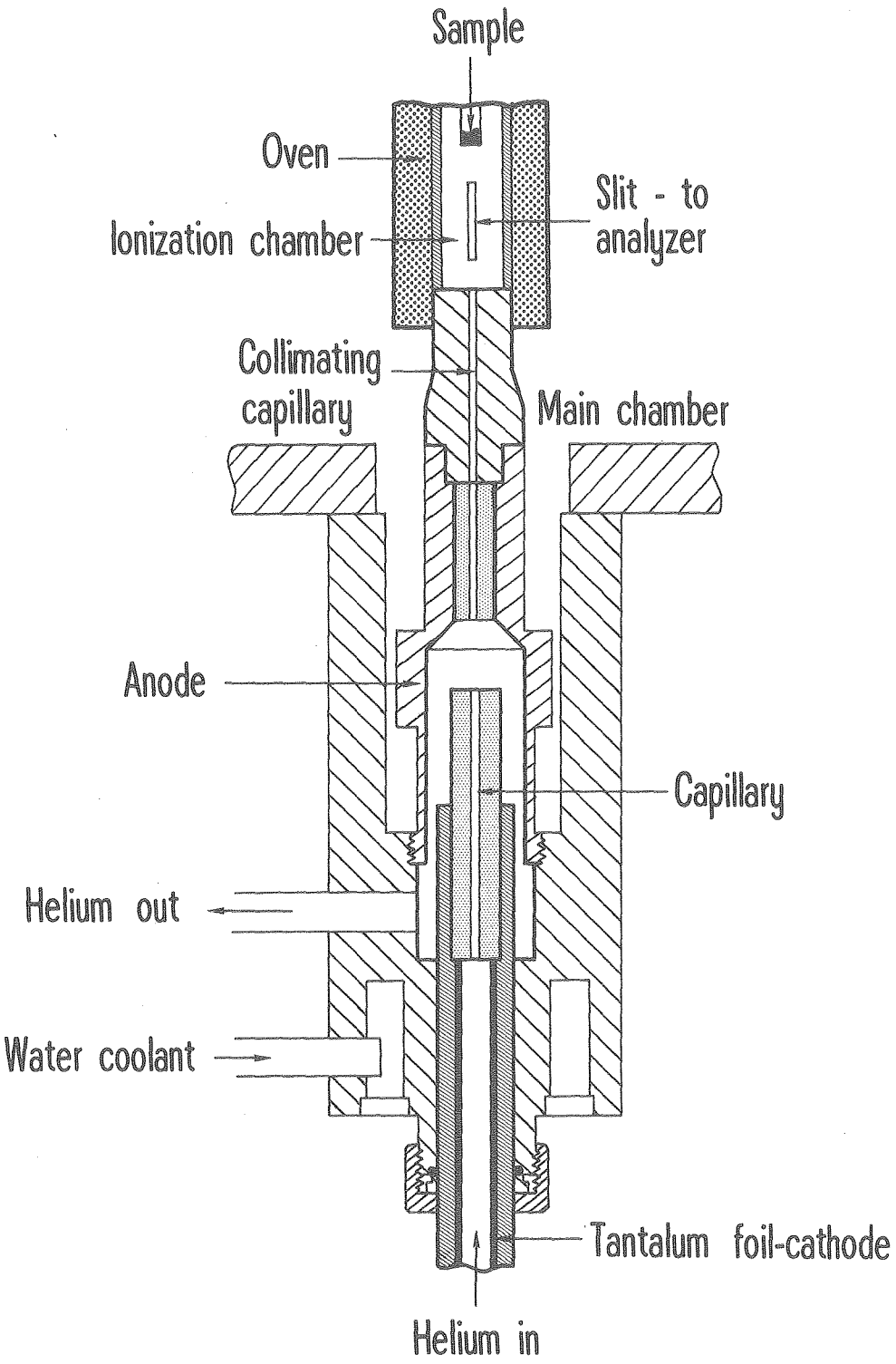

XBL 764-2762

Fig. 1

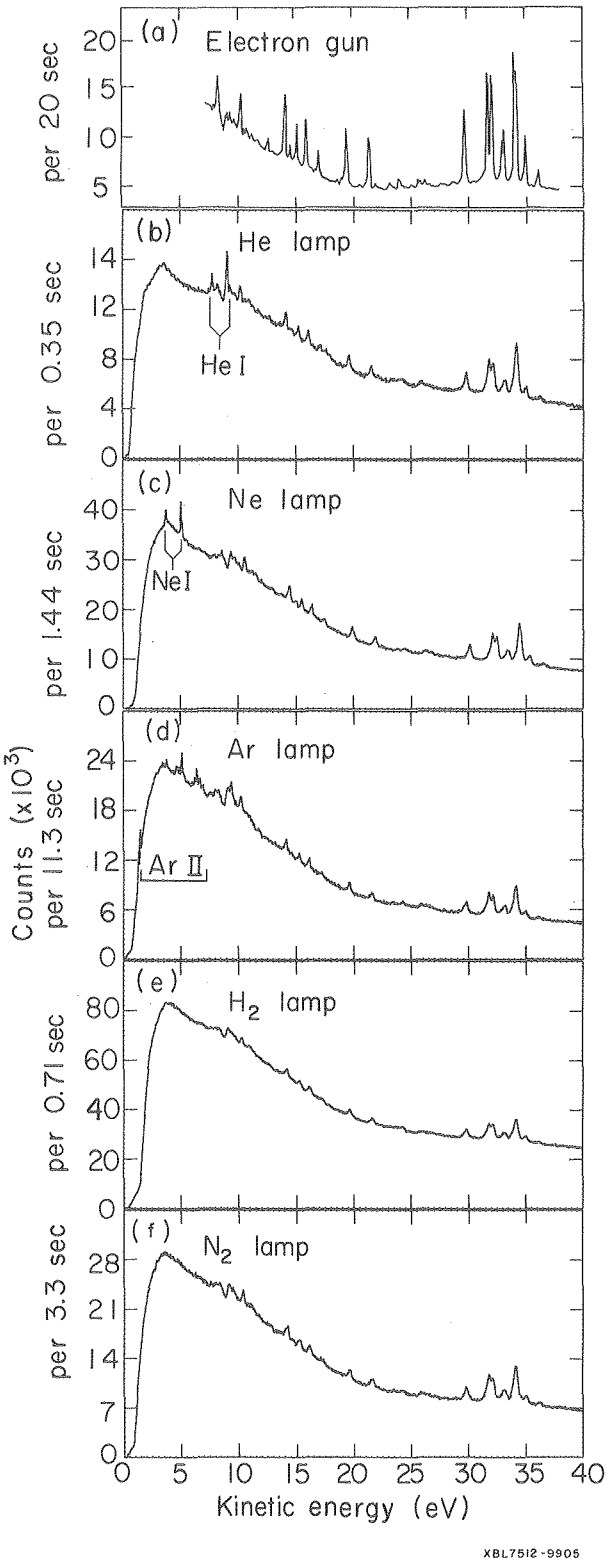
(a) Electron gun
per 20 sec
(b) He lamp
He I
per 0.35 sec
(c) Ne lamp
Ne I
per 1.44 sec
(d) Ar lamp
Ar II
Counts (x10³) per 11.3 sec
(e) H₂ lamp
per 0.71 sec
(f) N₂ lamp
per 3.3 sec
Kinetic energy (eV)
XBL7512-9905

Fig. 2

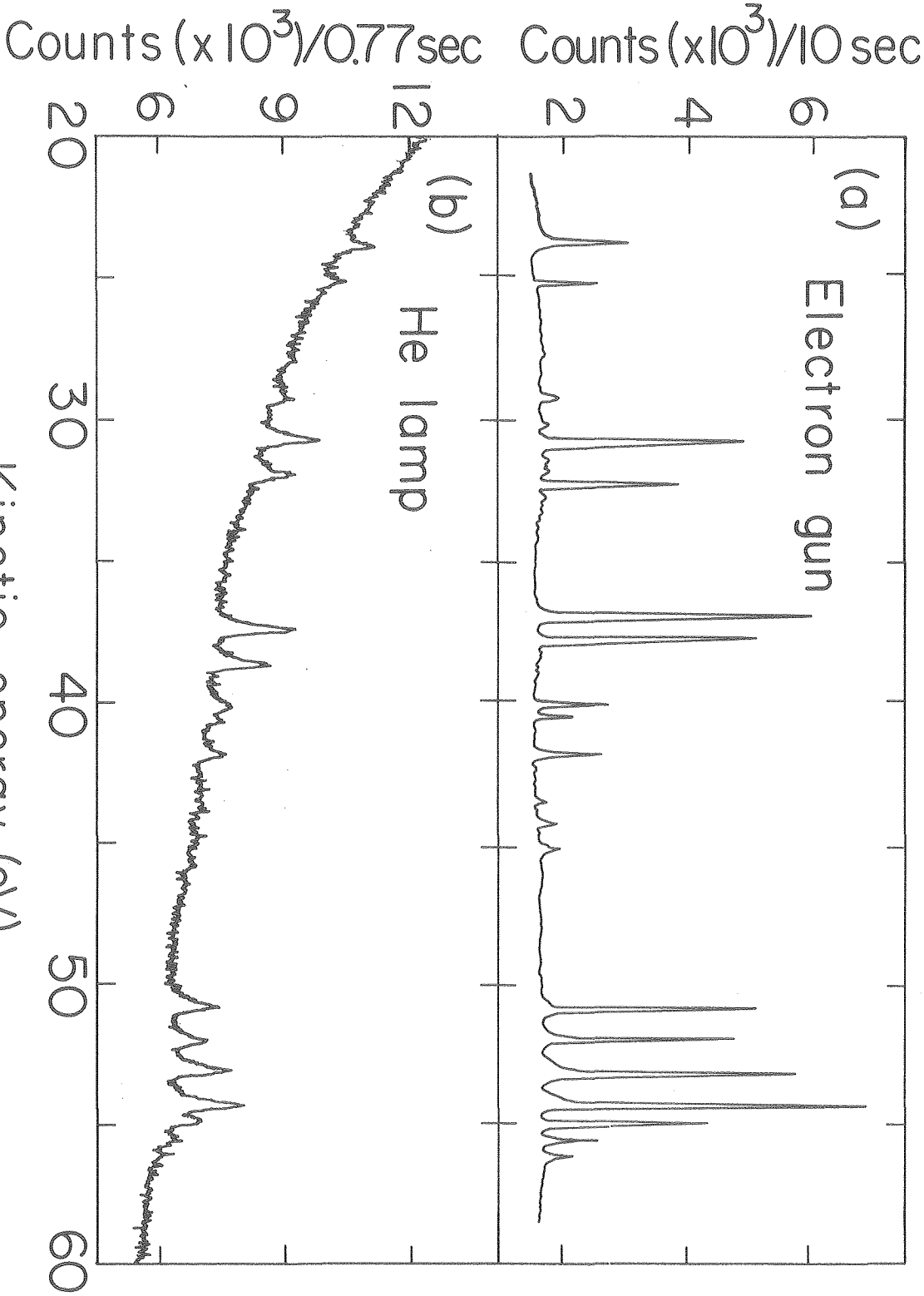

Fig. 3

XBL7512-9906

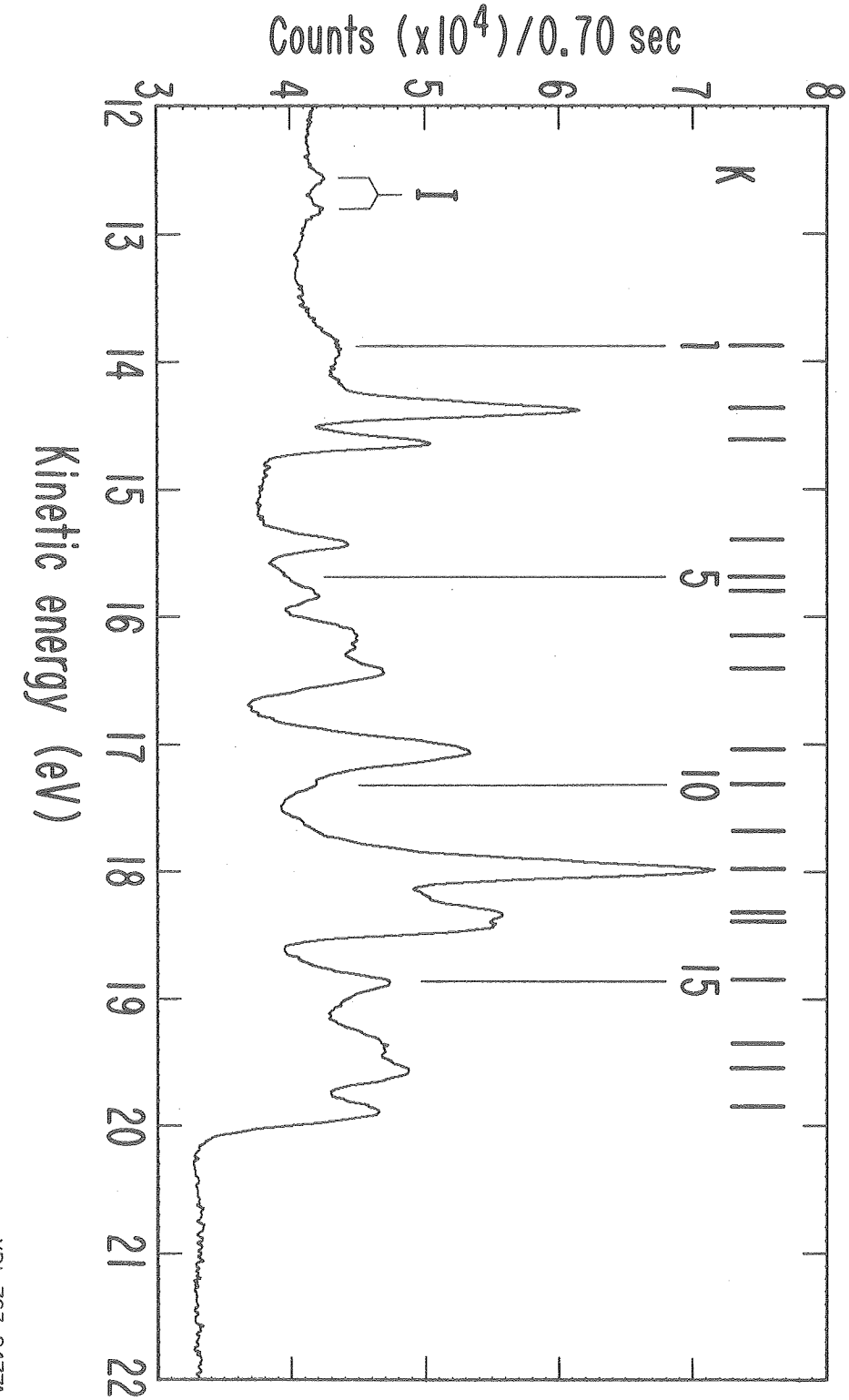

Fig. 4

XBL 763-2477A

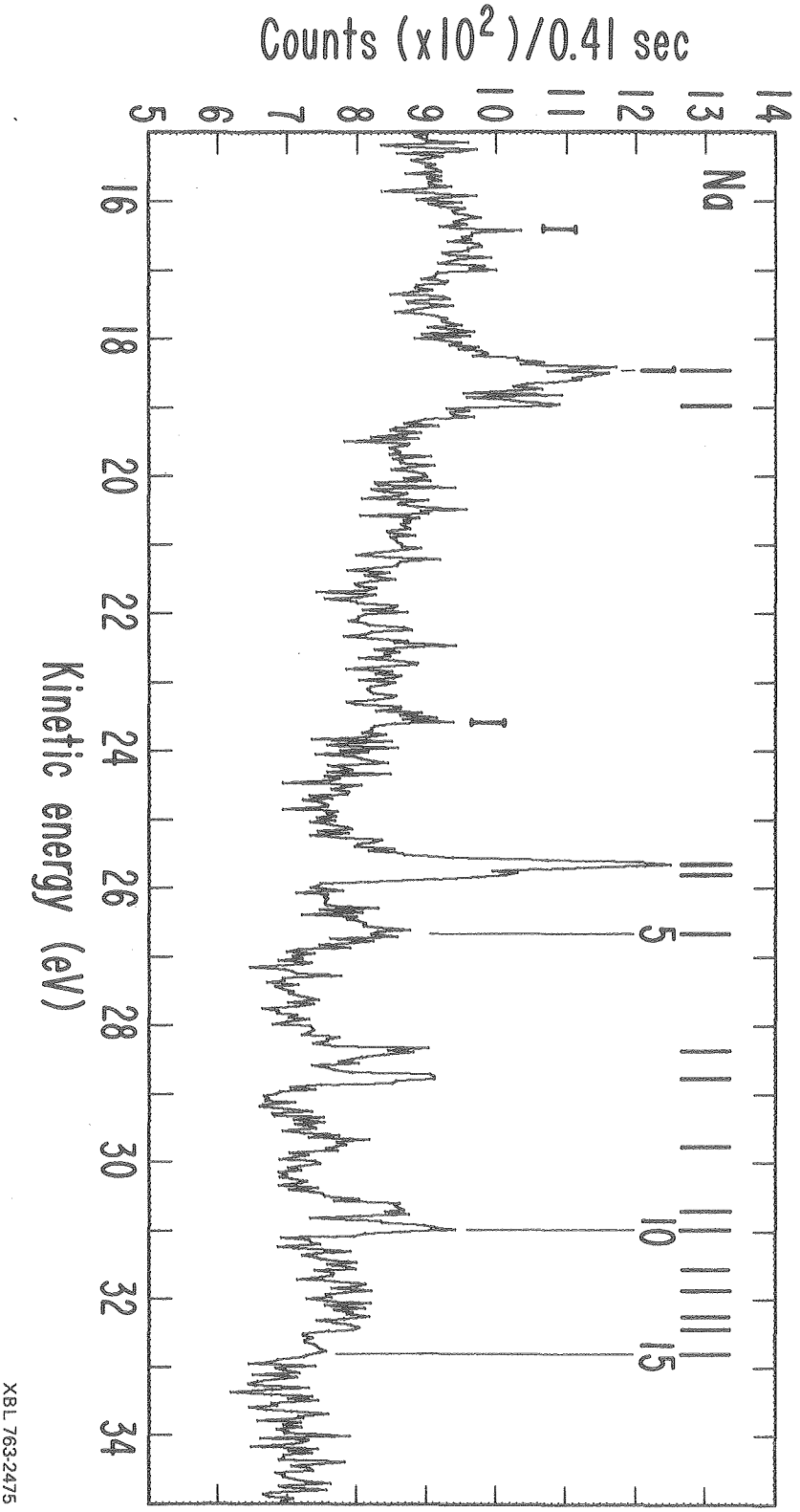

XBL 763-2475

Fig. 5

C. Experiments Performed at the Stanford Synchrotron Radiation Laboratory (SSRL)

1. Time-Resolved Fluorescence Spectroscopy

This section illustrates the utility of synchrotron radiation for performing time-resolved spectroscopy. The advantage of direct pulsed optical excitation over other techniques is demonstrated by measurements of the lifetimes of the three lowest lying excited states of atomic Xe. Because these studies involve resonance fluorescence, the radiation may become "trapped". Therefore, the measurements must be done as a function of pressure. A theory of radiation trapping is extended for the results presented here. It should be noted that for the measurement of the lifetime of the lowest excited state of Xe^+ reported in Chapter IV, this procedure is not necessary, because the fluorescence is non-resonant. As a result, the decay curve is not convoluted by the "prompt" or Rayleigh scattered light observed in the neutral Xe measurements.

The experiments were performed on the 8° beam line at SSRL. A detailed description of this facility was given elsewhere.[1] Briefly, 3.2 milliradians of radiation from the storage ring is subtended by a mirror and focused onto the grating of a 1-meter Seya-Namioka monochromator (UHV Design, GCA/McPherson). The dispersed light passes through an exit slit (2 Å band pass) and enters the gas cell through a LiF window. The LiF window serves both to isolate the ultrahigh vacuum (1×10^{-10} torr) of the monochromator from the gas cell and to filter out higher-order light. The excitation energies are restricted, however, to wavelengths longer than 1050 Å because of the LiF cutoff. The light entering the gas cell is 97% plane-polarized and focused to a cross-section

of approximately 1 mm x 3 mm.

The experimental apparatus and associated electronics are shown diagrammatically in Figure 1. An EMR 541-G photomultiplier (LiF window, CsI cathode), mounted perpendicular to both the propagation vector and the polarization vector, was used to detect the fluorescent radiation. The photomultiplier was placed approximately 1.0cm from the interaction region. The photomultiplier and associated electronics limited the time resolution of the experiments to ∿1.8 nsec. There was no energy-selective device in the fluorescence channel because in atomic systems in the low pressure limit only resonance fluorescence occurs. The acceptance range for fluorescence was 1050-1850 Å due to the LiF-cutoff and the CsI response limit of the photomultiplier.

The data were recorded by a conventional single photon counting technique. The photomultiplier pulses were amplified and discriminated, then used as the start signals for the time-to-amplitude converter equipped with a single channel analyzer (Ortec model 467). The stop pulse was provided by a signal from an induction coil located in the ring.* The data were accumulated in a multi-channel analyzer.

During these experiments, the electron beam current was between 12 mA and 18 mA, from which we expect a photon flux on the order of 10^{10}/sec. With sample pressure in the 10^{-6} torr range, the counting rate ranged from 1500 to 2500/sec., of which about one-third was true fluorescence events and two-thirds came from Rayleigh scattering of the incident light. Typical counting times were 60-90 min.

---

*This results in a reversal of the time axis in Figure 2. It is necessary to avoid reset-time counting losses of the time-to-amplitude converter.

The gases were obtained from Airco Company, and were 99.995% pure. To maintain a fresh sample in the gas cell, the gas was continuously leaked into the sample chamber, which was pumped by a diffusion pump. The base pressure was 1×10^{-6} torr.

Typical decay curves are shown in Figure 2. Data analysis was done by means of a least-square fitting routine in which the background was subtracted. The "prompt" peak with a maximum at time $t = 0$ (ca. channel 780) is due to the large number of Rayleigh scattering events, broadened by instrumental response, which is essentially Gaussian. This form of the response function was confirmed by measurements made off resonance, where Rayleigh scattering was present, but resonance fluorescence was not. The total observed resonance fluorescence decay curve is also broadened by the Gaussian "prompt" curve. Since the "prompt" curve decays very rapidly (FWHM - 1.8 ns), the true lifetime could be found by fitting at times far enough removed from $t = 0$, that the Gaussian had become negligible.

Lifetime measurements had to be carried out in the 10^{-5} - 10^{-6} torr pressure range to minimize the effects of resonance trapping. Even at these low pressures there is a finite probability for resonance scattering to occur before the fluorescence is detected. Such processes result in an apparent lifetime longer than the true one (see Appendix). To obtain the true lifetime, the pressure dependences were measured and extrapolated to zero pressure. Figure 3 illustrates this procedure for the $^3P_1$ and $^1P_1$ states of Xe, as well as for the $5p^5(^2P_{3/2})5d$ $J = 1$ state in Xe for which the lifetime has not been measured before.

Because these are the first direct lifetime measurements on these systems by this method, we discuss briefly the sources of error. There are two non-negligible error sources: uncertainties in pressure measurements (leading to a typical error of $\sim$2% in the extrapolated value of τ at $t = 0$), and statistical error (typically $\sim$1%). Cumulative errors are given in Table I.

A comparison of our results with previous data and theoretical predictions are given in Table I for xenon. The scatter as well as the large limits of error of the previous, less direct methods emphasize the need for direct resonance fluorescence lifetime measurements. An exception is the zero field level crossing measurement by Anderson[2] in Xe which we consider to be the most reliable set of earlier results. Our results for the $^3P_1$ and $^1P_1$ levels in Xe are in good agreement with the values given by Anderson.[2] Comparing our experimental results with theoretical predictions, the nonrelativistic HF calculations of Dow and Knox[11] and of Kim, et al.[6] yield lifetimes that are too long, whereas the intermediate coupling scheme of Gruzdev[12] yields values in very good agreement with experiment.

The lifetime of the $5p^5(^2P_{3/2})5d$ $J = 1$ state at 1192 Å in Xe was determined in the same manner. The result $\tau = 1.40 \pm 0.07$ ns reflects the large oscillator strength of this transition. There are no theoretical predictions available for comparison. Calculations of Gruzdev and Loginov[13] however, yield a value of 1.87 ns for the lifetime of the analogous state in krypton, which confirms the trend observed in xenon.

In summary, this work reports the first lifetimes of atomic states excited by synchrotron radiation. No other method used for time-resolved spectroscopy can characterize the system as well as direct optical excitation. Our results demonstrate that the synchrotron radiation available at SPEAR, has both the necessary timing characteristic and sufficient intensity to study atomic lifetimes at very low pressures. Our measurements yield accurate results for three levels in Xe, of which the $5p^5(^2P_{3/2})5d$ $J = 1$ state in Xe has not been previously reported. They also show the intermediate coupling approach to be the most useful for calculating these lifetimes.

APPENDIX: Radiation Trapping

In order to explain the relative slopes of the lines in Figs. 3 and 4, it is necessary to employ one of the theories on imprisonment of resonance radiation.[14-17] If τ_0 represents the true zero pressure lifetime, and τ the coherence time at some pressure, then it is predicted that

$$\tau = \frac{\tau_0}{1-x} \tag{1}$$

where according to D'yakanov and Perel[17]

$$x = 1 - \frac{1}{\sqrt{\pi}} \int_{-\infty}^{\infty} \exp(-t^2)\exp(-k_0 L e^{-t^2})\,dt \tag{2}$$

and according to Barrat[16]

$$x = 1 - \exp[-(\pi/6)^{1/2} k_0 L] \tag{3}$$

and in both cases[14]

$$k_0 = \frac{2}{\Delta\nu_D}\left(\frac{\ell n 2}{\pi}\right)^{1/2} \frac{\lambda_0^2}{8\pi} \frac{N}{\tau_0} \tag{4}$$

The quantity x represents the fractional absorption of resonance radiation by a layer of vapor of density N and thickness L; $1/k_0$ may be thought of as the minimum mean free path for absorption of resonance radiation of wavelength λ_0 and Doppler width $\Delta\nu_D$. For comparative purposes, the expression developed by Barrat will be used.*

Substituting Eq. (3) into Eq. (1) and expanding the exponential, one obtains†

*According to Nussbaum and Pipkin (see Ref. 18), both theories give equivalent results at sufficiently low values of the optical thickness, $k_0\ell$. For these measurements, $k_0\ell \sim 0.3$.

†Including terms only to first order introduces an error of $\sim(k_0\ell)^2$ or less than 10%. The data is insufficient to warrant inclusion of higher order terms.

$$\tau = \tau_0(1 + (\pi/6)^{1/2} k_0 L + \ldots . \tag{5}$$

or

$$\tau = \tau_0 + KLN \tag{6}$$

where

$$K = (\pi/6)^{1/2} \frac{2}{\Delta\nu_D} \left(\frac{\ell n 2}{\pi}\right)^{1/2} \left(\frac{\lambda_0^2}{8\pi}\right) \frac{g_2}{g_1} \quad .$$

Thus, a plot of τ - vs. - N should yield to first order a straight line of slope KL.

Since in these experiments L was not well defined, and to account for the different isotopes,[18] the only meaningful comparison is a ratio of the slopes of the lines for a given gas.

Equation (6) predicts the slopes of the 5s[3/2]1 line and the 5s[1/2]1 line of Kr to be in a ratio of 1.2 : 1; the experimental result is 1.2 ± 0.2 : 1 for Xe; the predicted value of the slopes of the 5s[3/2]1 to 6s[1/2]1 to 5d[3/2]1 are 1.9 : 1.3 : 1.0, while experimentally the values are 1.9 ± 0.5 : 1.0 ± 0.3 : 1.0.

The experimental results are more than adequately explained by the theory, thus justifying the linear extrapolation used to obtain the zero pressure lifetime.

REFERENCES

1. H. Winick, VUV Radiation Physics, edited by E. E. Koch, et al. (Pergamon Viewpeg, 1974), p. 776; V. Rehn, et al., ibid. p. 780.
2. D. Kent Andersson, Phys. Rev. 137, A21 (1965).
3. P. G. Wilkinson, J. Quant. Spectr. Rad. Transfer 6, 823 (1966).
4. G. I. Chashcina and E. Ya. Shreider, Opt. Spectr. 20, 283 (1966).
5. J. M. Vaughan, Phys. Rev. 166, 13 (1968).
6. Y. K. Kim, M. Inokuti, G. E. Chamberlain, and S. R. Mielezarek, Phys. Rev. Letters 21, 1146 (1968).
7. P. M. Griffin and J. W. Hutcherson, J. Opt. Soc. Am. 59, 1607 (1969).
8. K. T. Lu, Phys. Rev. A4, 579 (1971).
9. W. Wieme and P. Mortier, Physica 65, 198 (1973).
10. A. Delage and J. D. Carette, Phys. Rev. A14, 1345 (1976).
11. J. D. Dow and R. S. Knox, Phys. Rev. 152, 50 (1966).
12. P. F. Gruzdev, Opt. Spectr. 22, 170 (1967).
13. P. F. Gruzdev and A. V. Loginov, Opt. Spectr. 38, 611 (1975).
14. A. C. E. Mitchell and M. W. Zemansky, Resonance Radiation and Excited Atoms, (Cambridge University Press, Cambridge, England, 1964).
15. T. Holstein, Phys. Rev. 72, 1212 (1947).
16. J. P. Barrat, J. Phys. Radium 20, 541, 633, 657 (1959).
17. M. I. D'yakanov and V. I. Perel, Zh. Eksperim, i. Teor. Fiz. 47, 1483 (1964) (Translation: Soviet Phys.-JETP 20, 997 (1965)).
18. Gilbert H. Nussbaum and Frances M. Pipkin, Phys. Rev. Letters 19, 1089 (1967).

Table I. Compilation of lifetimes and oscillator strengths for the two transitions $^3P_1 \rightarrow {}^1S_0$ and $^1P_1 \rightarrow {}^1S_0$ in Xenon.

$^3\tau$(ns)	^3f(1470Å)	$^1\tau$(ns)	^1f(1296Å)	method	authors
3.79 ± 0.12	0.256 ± 0.008	3.17 ± 0.19	0.238 ± 0.015	zero field level crossing	Anderson[2] (1965)
3.5 ± 0.6	0.28 ± 0.05	3.3 ± 0.7	0.23 ± 0.05	linear absorption	Chashchina and Shreider[4] (1965)
3.74 ± 0.25	0.260 ± 0.20	2.80 ± 0.20	0.270 ± 0.020	total absorption	Wilkinson[13] (1966)
		3.89 ± 0.10	0.194 ± 0.005	total absorption	Griffin and Hutcherson[7] (1969)
3.73 ± 0.75	0.260 ± 0.052	4.0 ± 0.8	0.190 ± 0.038	electron energy loss	Geiger[5] (1970)
3.57	0.272	3.99	0.189	low-energy electron impact	Lu[8] (1971)
4.6 ± 0.5	0.213 ± 0.020	4.2 ± 0.9	0.180 ± 0.040	resonance imprisonment	Wieme and Mortier[9] (1973)
5.31	0.183	4.47	0.169	low-energy electron impact	Delage and Carette[10] (1976)
3.46 ± 0.09	0.263 ± 0.007	3.44 ± 0.07	0.229 ± 0.007	resonance fluorescence	present work
5.00	0.194	5.13	0.147	nonrel. Hartree-Fock	Dow and Knox[11] (1966)
3.47	0.28	3.02	0.25	intermediate coupling calc.	Gruzdev[12] (1967)
4.58	0.212	3.99	0.189	nonrel. Hartree-Fock	Kim, et al.[6] (1968)

FIGURE CAPTIONS

Fig. 1. Schematic representation of experimental apparatus.

Fig. 2. Fluorescence decay curve of Xe.

Fig. 3. Lifetime vs. pressure for Xe.

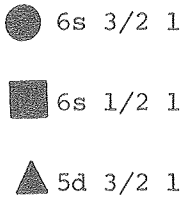

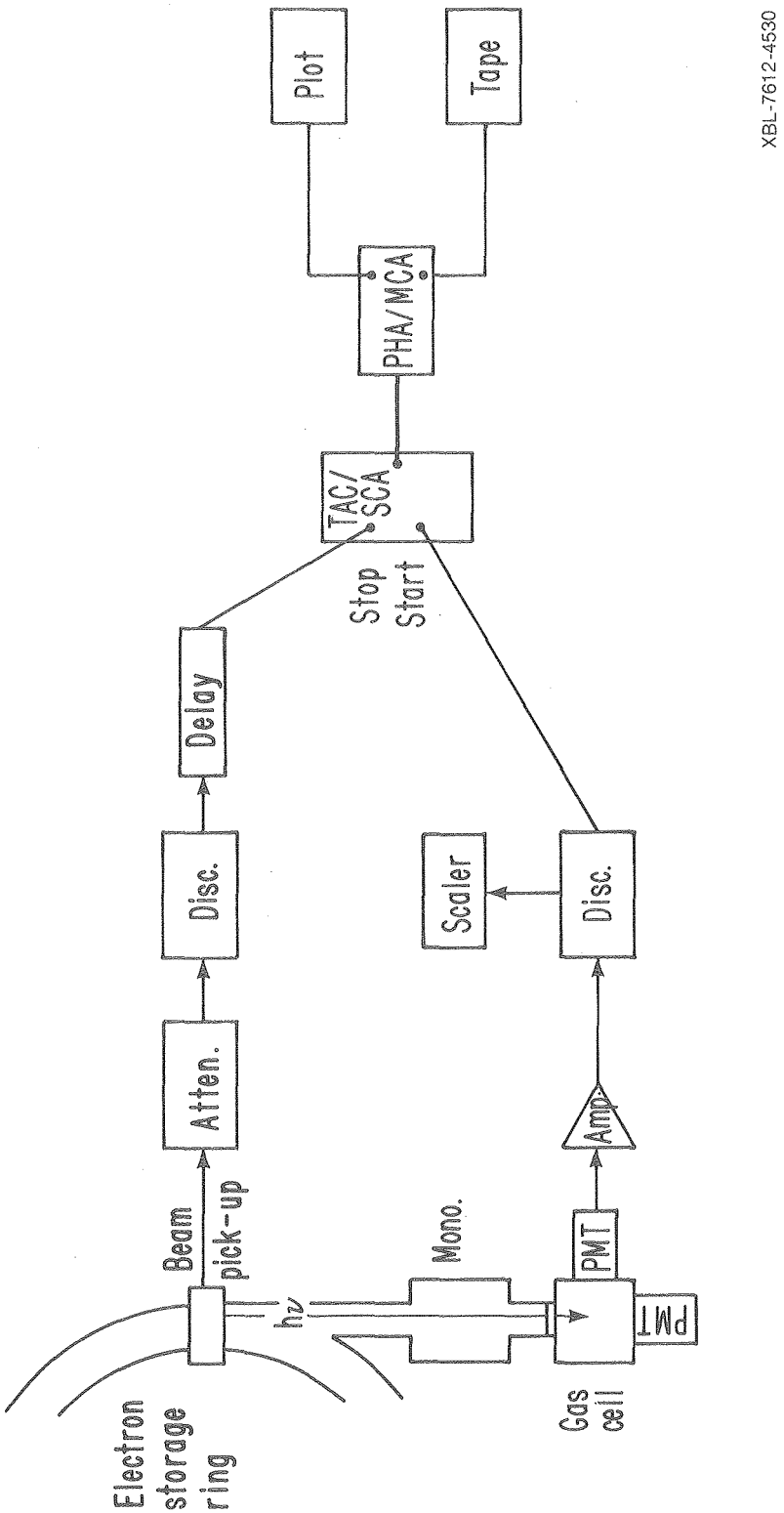

XBL-7612-4530

Fig. 1

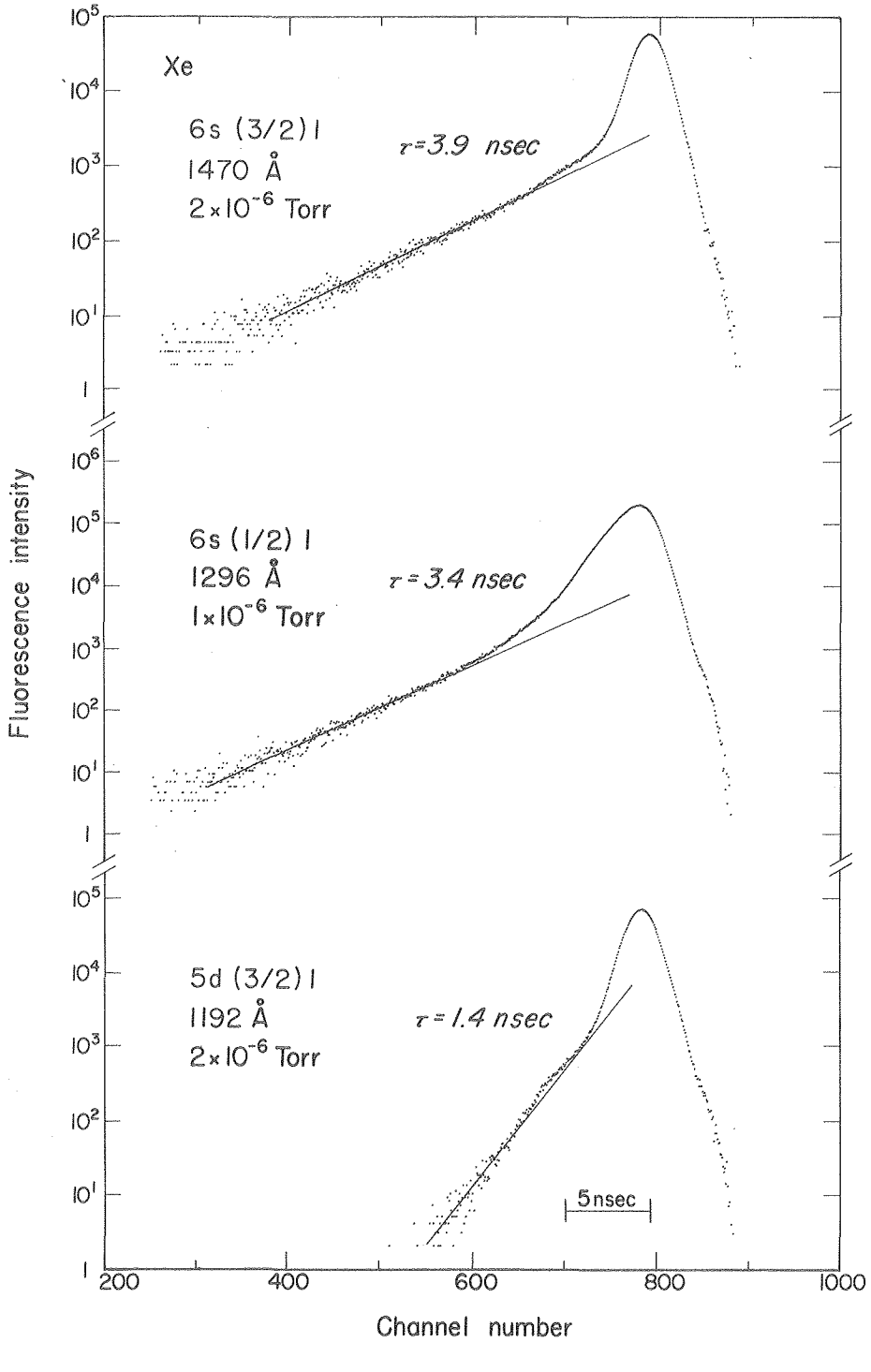
Xe
6s (3/2) 1
1470 Å
2×10⁻⁶ Torr
τ=3.9 nsec
6s (1/2) 1
1296 Å
1×10⁻⁶ Torr
τ = 3.4 nsec
5d (3/2) 1
1192 Å
2×10⁻⁶ Torr
τ = 1.4 nsec
5nsec
Fluorescence intensity
Channel number
XBL-7612-4535

Fig. 2

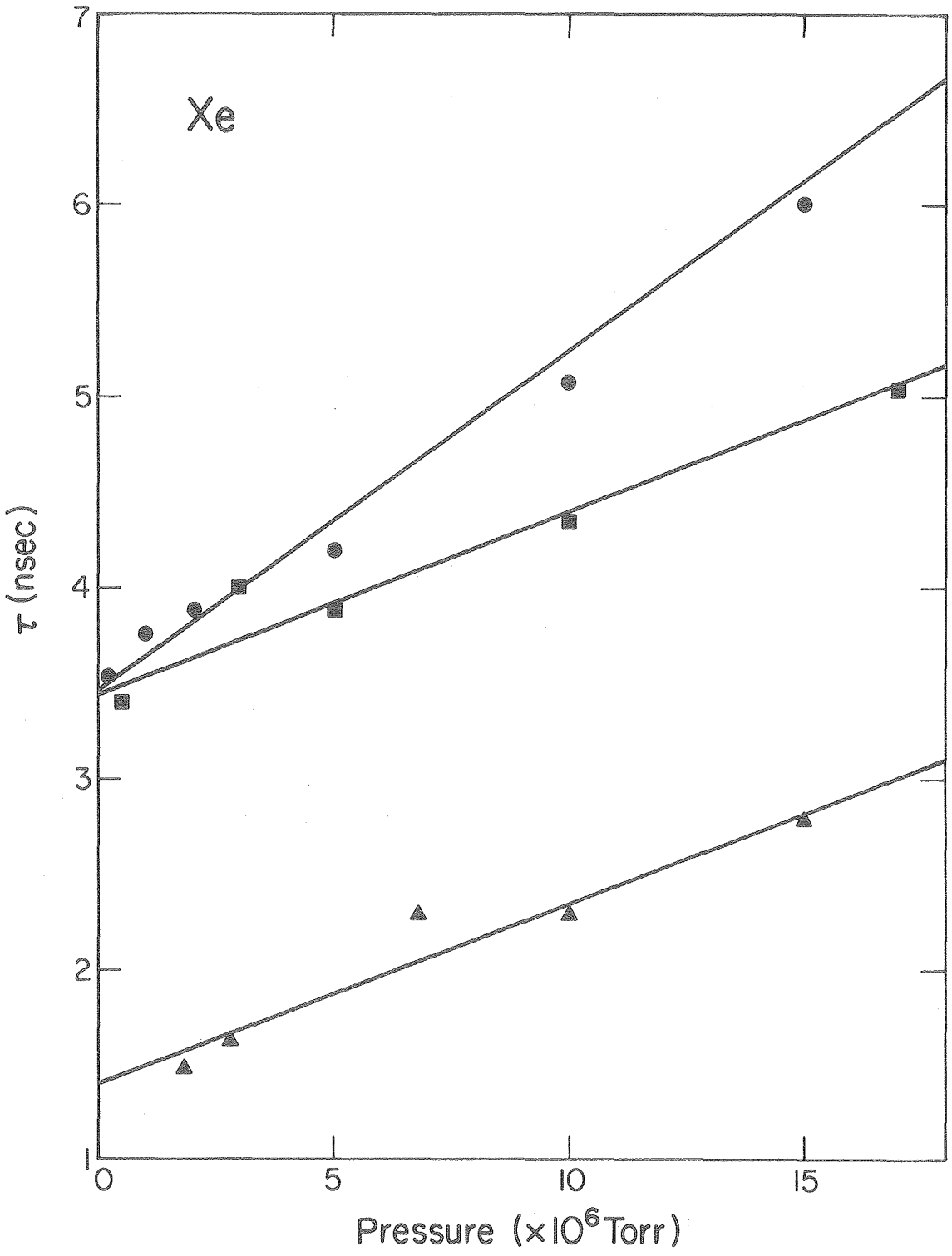

XBL-7612-4532

Fig. 3

2. The Aluminum Window System

In order to extend the excitation energy range beyond the LiF cutoff (1050 Å), a material with good transmission properties in this region is required. Such requirements are best met through use of a 1500 Å Al window. This material is documented as having good spectral characteristics for wavelengths shorter than 700 Å.

Since the window is so thin, precautions must be taken to ensure SPEAR's vacuum integrity. This is accomplished through the introduction of two sub-systems: a window chamber (Part a), and a sample inlet system (Part b). The interlock system will be described in Part c.

a. Window Chamber (see Figure 1)

Since thin metal foil windows are potentially useful for many gas-phase experiments utilizing different sample chambers, the window chamber is designed as a self-contained UHV system. All components are of UHV (10^{-9} - 10^{-10} Torr) compatibility and the system is thoroughly interlocked against large pressure changes on either side of the window.

The window chamber is separated from SPEAR by means of a very fast ($\sim$200 msec), UHV pneumatic gate valve (1). This valve serves to isolate the window system and because of its fast response time, prevents large volumes of gas to enter SPEAR should a window rupture occur. During experiments, the right-angle valves (4) separate the sample chamber and/or the ion pump from the UHV beam line. Ion gauges (3) monitor pressures on either side of the window and are appropriately interlocked (see Part C). Equal volumes on both sides of the window guarantee that no pressure differential occurs during initial pump down by the cryo pump/ion pump arrangement.

b. Sample Inlet System (see Figure 2)

Modifications to the LiF sample inlet system were deemed necessary in order to prevent the possibility of a high pressure surge in the sample chamber which could burst the window. Gas samples from a high pressure tank enter through the interlocked on/off valve (12) and are stored in a one liter ballast (10) at pressures between 500 Torr to 1 atmosphere. If the ballast pressure meets the interlock requirements, the pneumatic valve (8) can be opened and the gas enters the sample chamber through the leak-valve (7). Fast, high pressure bursts (< 1 sec) into the sample chamber are not likely since the leak valve presents a large conduction barrier, so that the pressure interlocks in the sample chamber may respond in sufficient time to close the gate valve.

c. Interlocks

The two pneumatic valves (1) and (8) (see Figures 1 and 2) are the most crucial in preventing and controlling a major pressure burst in the sample chamber. The pneumatic valve (8) of the sample inlet system prevents the high pressure gas in the supply tank and ballast from entering the sample chamber, while the pneumatic gate valve (1) prevents SPEAR vacuum contamination. Hence, the interlock logic is primarily a control of these two valves and their interconnection.

Figure 3 shows the basic logic for the gas inlet interlocks. The pneumatic valve (8) is normally closed and is opened when the solenoid valve (9) opens and the air passes to the pneumatic cylinder. When the solenoid valve is closed or the power turned off, the air pressure is released and the pneumatic valve closes. Hence, interlocking requires

the line voltage to the solenoid valve to be enabled or disabled depending on the criteria chosen. The criteria for enabling the pneumatic valve are:

1. The on/off toggle valve (12) between ballast and high pressure tank must be closed. This interlock is accomplished with the use of a micro-switch attached to the body of the valve.
2. The pressure sensor (transducer) (11) output voltage must be less than the voltage corresponding to the maximum allowed pressure in ballast tank.
3. Drop in line voltage causes disabling.

This circuit also outputs a voltage for enabling the pneumatic gate valve of the window chamber.

A similar logic diagram for the window chamber is shown in Figure 4. In this case, however, the fast closing valve requires air pressure (100 psi) to open and close, although a power failure to the solenoid valve will close the gate valve. Therefore, the air pressure must also be monitored so that a loss of air pressure cuts off line voltage which then closes the gate valve. The other enabling criteria are the following:

1. Sample inlet system must be enabled.
2. Pressure on the SPEAR UHV side of the window must be $<10^{-9}$ Torr This pressure is measured on a Varian UHV nude ionization gauge and the trip point is set using the process control circuit of the Varian Dual Range Ionization Gauge Controller, Model #971-1008.

3. Pressure on the sample chamber side of the window is measured by a combination of a Bayard-Alpert ionization gauge and a Granville-Phillips Thermo-Gauge (Pirani Gauge). The trip point will be set at 0.1-0.01 Torr on the process control logic of the Granville-Phillips Series 260 Ionization Gauge Controller.

4. Drop in line voltage disables gate valve.

In the event that the pneumatic gate valve is disabled, an output will be made such that IV-2 (8° beam line valve) will also close.

d. Set up Procedure

In order to show how the preceding precautions will be used to overcome the major problems of a thin window system, this section deals with the setup of the apparatus for an experiment. This is intended to give the reader a more experimental perspective.

Once the entire system (window chamber, sample chamber, sample inlet system) has been attached to the beam line, pumping down of the window chamber takes place. First, a cryo pump is used to rough down the small volume between valve (1) and the valve to the monochromator (8° beam line). Then with valves (1) and (5) closed and valves (4R) and (4L) open, a cryo pump is used to rough the window chamber. Simultaneously, a separate cryo pump pumps out the entire sample chamber and sample inlet system. Next, valve (1) is opened, keeping the valve to the monochromator closed, and the ion pump (6) brings the system to the UHV range (10^{-9} Torr). Valves (4R and (4L) are then closed and the valve to the monochromator opened. Then the valve (5) to the sample chamber is opened for alignment of the beam. Following this, valve (1) is closed and sample is introduced to the ballast tank (10) with toggle valve (12) open and

pneumatic valve (8) and metering valve (7) closed. Valve (12) is shut; solenoid valve (9) is enabled to open valve (8) and the sample is allowed to flow from the ballast tank to the metering valve. This valve is then opened slowly until the desired pressure is reached in the sample chamber, and it is then closed. If all interlocking conditions are met, valve (1) is enabled and the experiment may begin. For very low pressure measurements, the valve (4R) may be opened, so that the ion pump working in conjunction with the metering valve will give the option of operating a "flow" type system.

FIGURE CAPTIONS

Fig. 1. Schematic of the window isolation chamber.

Fig. 2. Schematic of the sample inlet system.

Fig. 3. Logic diagram for gas inlet interlocks.

Fig. 4. Logic diagram for window system interlocks.

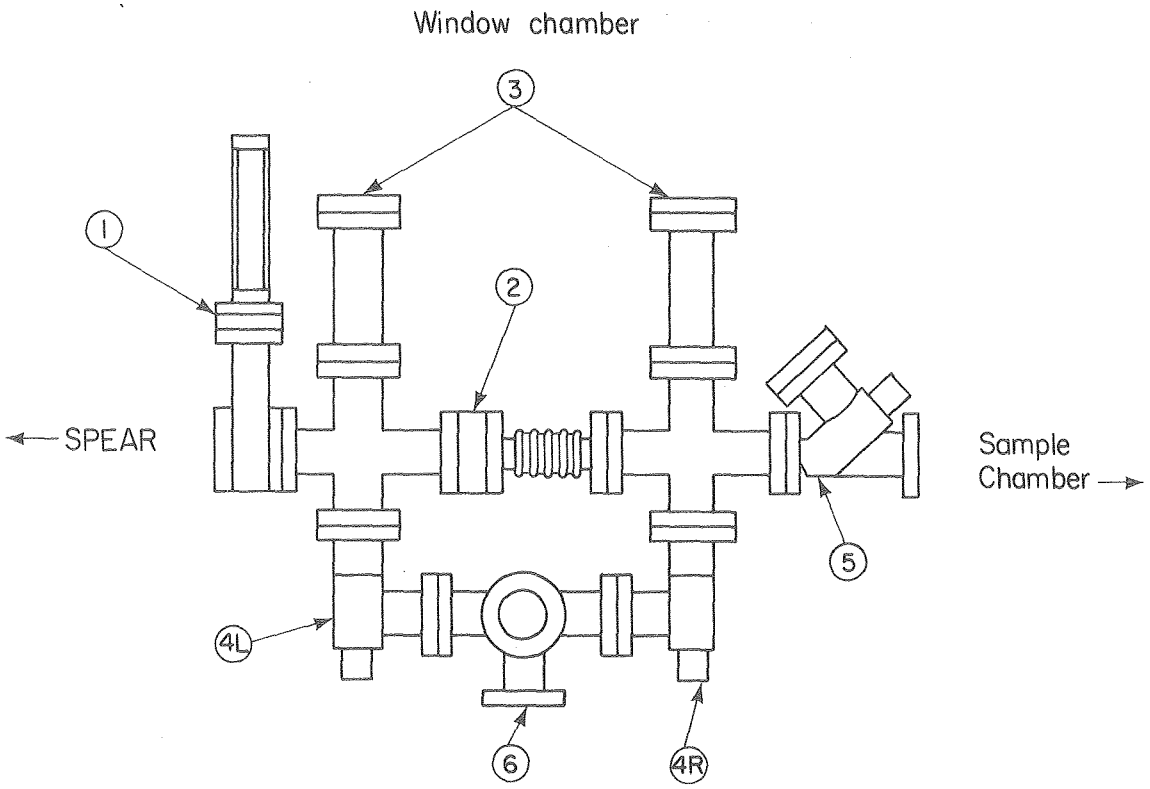

XBL 794-1125

Fig. 1

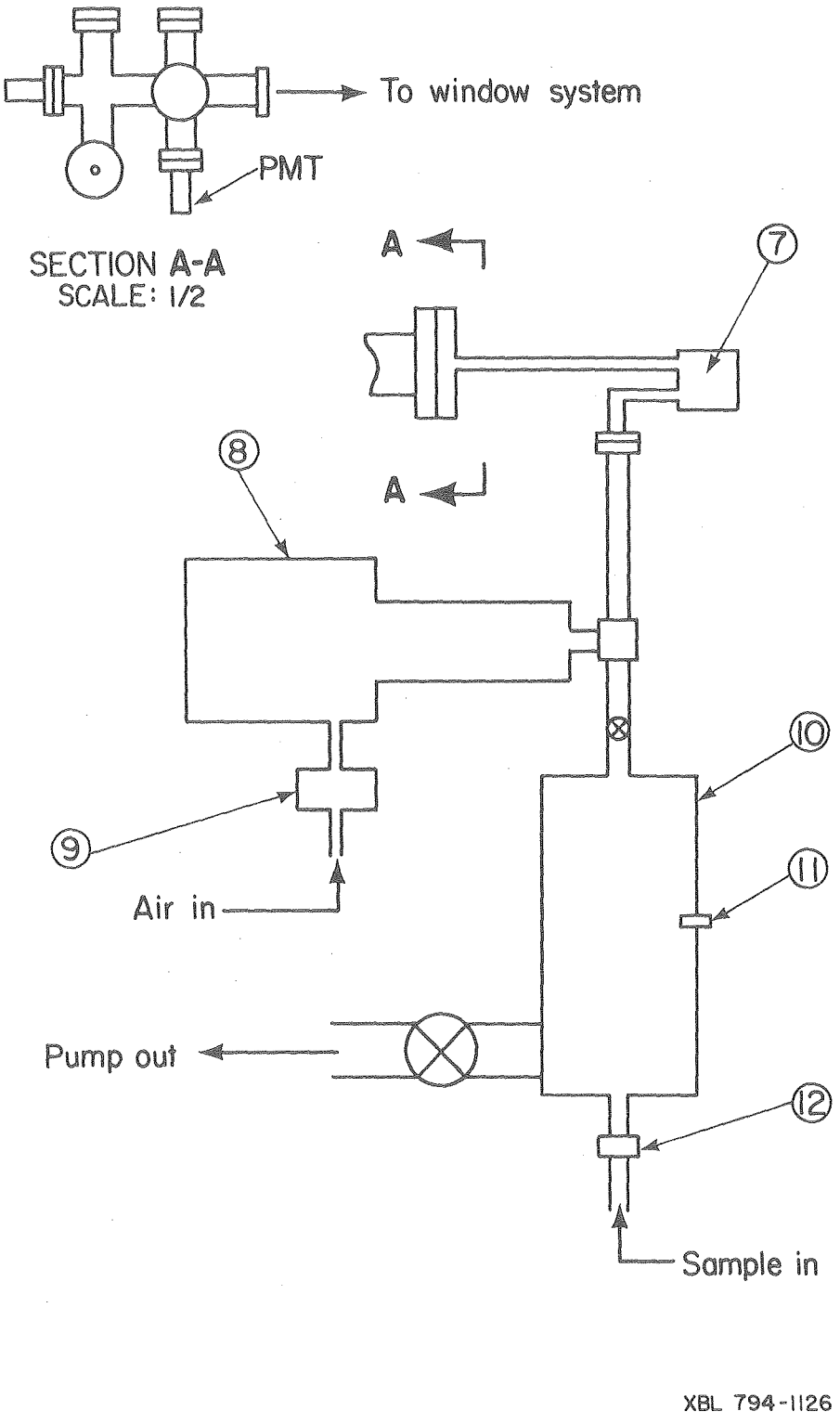
To window system
PMT
SECTION A-A
SCALE: 1/2
A
A
7
8
9
10
11
12
Air in
Pump out
Sample in
XBL 794-1126

Fig. 2

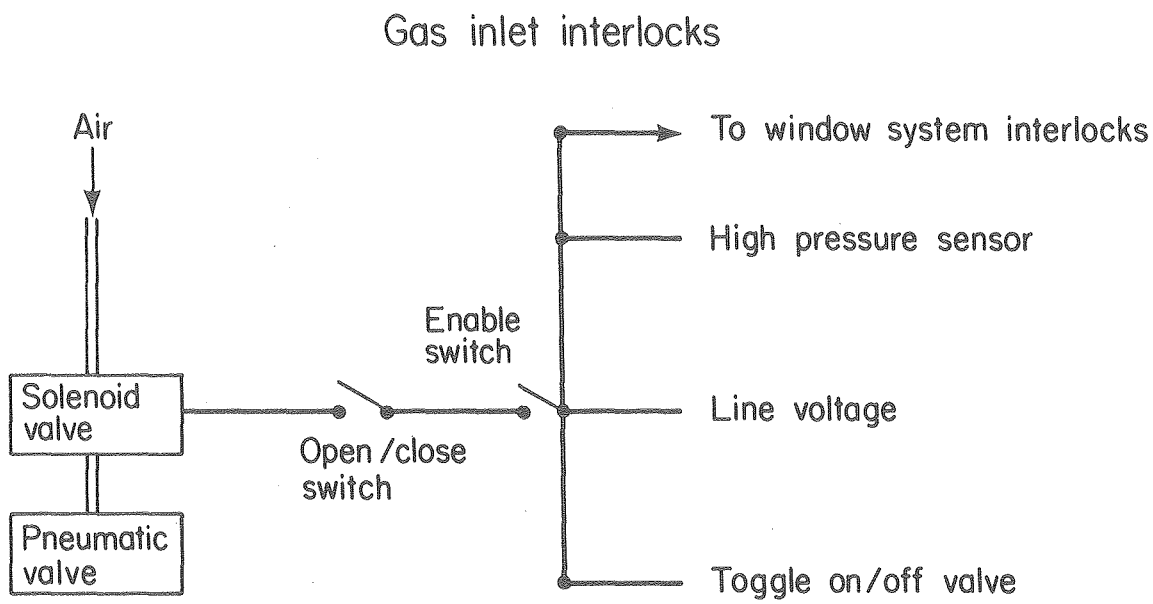
Gas inlet interlocks
Air
Solenoid valve
Pneumatic valve
Open /close switch
Enable switch
To window system interlocks
High pressure sensor
Line voltage
Toggle on/off valve
XBL 794-1127

Fig. 3

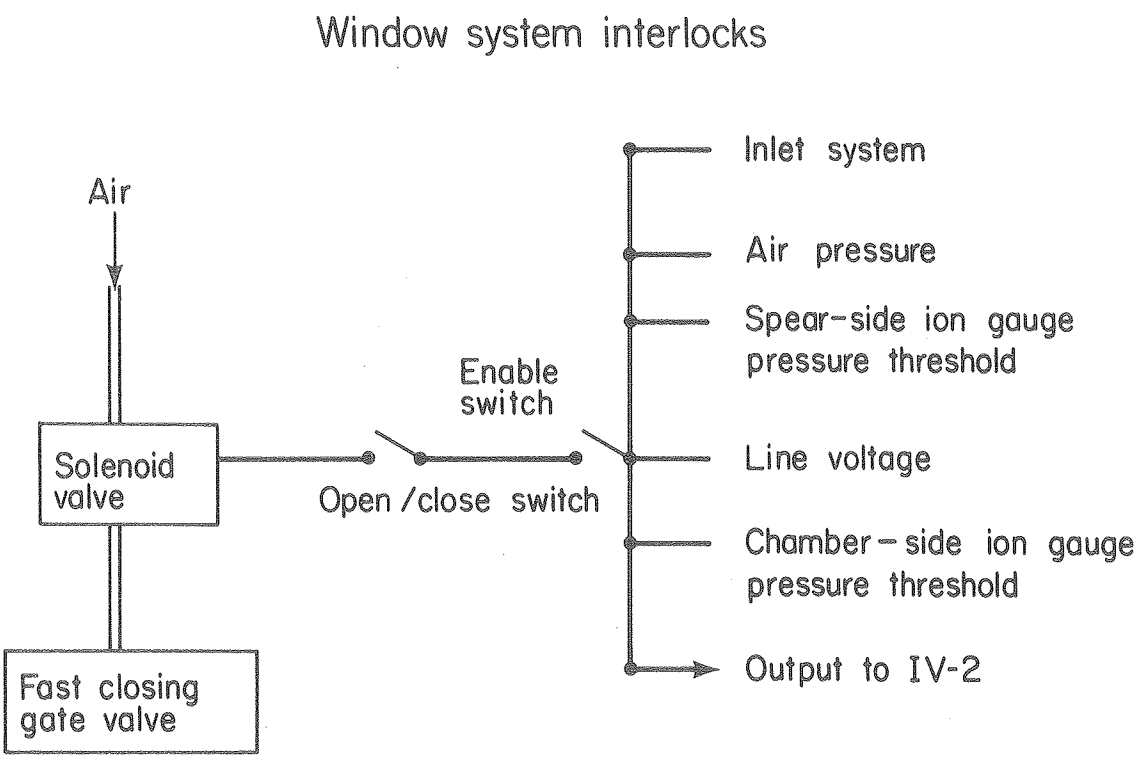
Window system interlocks
Air
Solenoid valve
Fast closing gate valve
Enable switch
Open /close switch
Inlet system
Air pressure
Spear-side ion gauge pressure threshold
Line voltage
Chamber-side ion gauge pressure threshold
Output to IV-2
XBL 794-1128

Fig. 4

3. Time-of-Flight Photoelectron Spectroscopy of Gases

a. Introduction

Photoelectron spectroscopy of gases using present day synchrotron radiation sources is a comparatively low counting rate experiment. This is a result of both the relatively small photon fluxes available in the VUV (typically $<10^{11}$ sec^{-1}cm^{-2}) and the small sample densities ($<10^{14}$ cm^{-3}) normally employed in gas-phase photoelectron measurements. Also, angle resolved experiments require an angular resolution of at least $\pm 5^{\circ}$, implying a collection solid angle of $\leq 10^{-2}$ sterdians. These factors lead to typical counting rates of 10 - 100 sec^{-1}, depending on the cross-section of the species being studied. It is therefore imperative to develop very efficient electron analyzers to avoid prohibitively long counting times. To date, nearly all gas-phase photoelectron experiments using synchrotron radiation have employed electrostatic deflection electron analyzers, either a 127 cylindrical mirror sector[1] or a cylindrical mirror analyzer.[2] Although these analyzers have high resolving capabilities, they are intrinsically inefficient because electrons in only a narrow energy range are collected at any one time.

An alternative and much more efficient method of electron kinetic energy analysis is by the time-of-flight (TOF) technique. A TOF analyzer measures the time required for a photoelectron to travel over a fixed distance of field free space after an ionizing event. Using standard timing/coincidence techniques, TOF analysis permits the entire energy spectrum within a given time window to be analyzed simultaneously. The counting efficiency is therefore increased relative to the more conventional deflection-type analyzers by a factor equal to the number of collecting channels (typically 10^3). Since all the peaks in a given

spectrum are collected simultaneously, it is not necessary to normalize relative peak areas for fluctuations in sample pressure and beam decay. In addition, because TOF is a coincidence technique, random background contributions such as electron multiplier dark noise are equally divided among the time channels of a collection window which includes the entire repetition period of the pulsed source. Hence, the background contribution to any given time channel is significantly reduced and signal-to-background ratios of 1:1 or smaller can be tolerated. Because the actual collection time window is normally smaller than the full repetition period, a further improvement in the total signal-to-background ratio is obtained.

The pulsed nature of synchrotron radiation from large storage rings provides an ideal time base for electron TOF analysis. Recently, Bachrach, et al.,[3] performed solid state photoemission experiments employing a prototype TOF analyzer and the pulsed synchrotron radiation at the Stanford Positron Electron Accelerator Ring (SPEAR). These measurements clearly established the feasibility and usefulness of the TOF technique based on pulsed synchrotron radiation. TOF detection is facilitated by the excellent time structure (0.3 nsec pulse width and a 780 nsec repetition period) of the radiation produced at SPEAR. These timing characteristics are ideal for electron TOF analysis because the very narrow pulse imparts only a small kinetic energy spread to the ejected electrons (40 meV at 10 eV). Furthermore, the relatively long repetition period permits kinetic energies from 1 eV to several hundred eV to be analyzed using practical drift tube lengths ($\sim$30 cm).

The TOF apparatus described here is significantly different from other gas-phase TOF instruments using VUV radiation recently developed by Tsai, et al.,[4] and Guyon, et al.[5] In those spectrometers only near-threshold ($\leq$1 eV) photoelectrons are detected, and they are collected over large solid angles, yielding spectra which are somewhat angle-integrated. These limitations would preclude certain studies of autoionization phenomena and photoelectron anisotropies. Because synchrotron radiation is ideally suited for probing resonant phenomena and angular distributions, our TOF detector was designed to analyze electrons over a wide energy range at medium energy resolution and high angular resolution.

b. Apparatus

The TOF apparatus shown schematically in Figure 1 was designed for experiments on the 8° beam line at SSRL. After final focusing, the beam passes through the window isolation fore chamber. This section of the apparatus is used to isolate the sample chamber, which is operated at a relatively high pressure of $\sim 2 \times 10^{-5}$ torr, from the monochromator and beam line. Isolation is accomplished by ultra-thin ($\sim$1500 Å) In and Al windows which are capable of withstanding differential pressures of up to 1 torr and have acceptable transmission for the photon energies of interest (see Fig. 2).[7] At the peak transmittance wavelength, $\sim$570Å the photon flux is estimated to be 5×10^{9} $sec^{-1}cm^{-2}$ for typical operating conditions of 2Å band pass and 10 mA SPEAR electron ring current. A sodium salicylate scintillator and optical phototube (RCA, 8850) are used to continuously monitor the beam intensity.

The gas sample enters the vacuum chamber through a disc of 10 μ diameter, 1 mm long microchannels (Galileo Corp.) sealed with epoxy to the end of a 1 mm capillary tube and located approximately 5 mm above the interaction region. After assembly, the inlet probe including the capillary array was vacuum coated with gold in order to prevent charging near the ionization region. The microchannel array serves to collimate the gas source, increasing the forward intensity over that of a simple effusive source of the same backing pressure. Based on the work of Johnson, et al.,[8] and Jones, et al.,[9] we estimate the increase in forward intensity, the "peaking factor",[9] to be ∿7 for a 5 torr backing pressure with a half-intensity beam angle of $\Theta_{1/2} = 6.5^{\circ}$. Here $\Theta_{1/2}$ is defined by $I(\Theta_{1/2}/I(0^{\circ}) = 1/2$. This can be compared to the 60° half intensity angle of an effusive beam source, indicating that significant collimation is achieved by expansion through the channel array. Backing pressures typically ranged between 2 torr and 10 torr as measured by a capacitance manometer (MKS Instruments, Inc.). At these backing pressures, the particle density is predicted to be $\sim 10^{13} cm^{-3}$, which is consistent with the observed photoelectron counting rates. The resultant gas jet is directed into a conical "gas catch" directly below the ionization region which is pumped by a 500 liter/sec. turbomolecular pump (Airco-Temescal). A second 500 liter/sec. turbomolecular pump attached to the main chamber provides a background pressure of $\sim 2 \times 10^{-5}$ torr.

Photoelectrons enter the TOF analyzer through a 2.4 mm orifice located 2.3 cm from the center of the interaction region. The orifice collimates the ejected electron signal and also acts as a conduction

barrier between the sample chamber and detector housing for the purpose of differential pumping. A total flight path of 28.5 cm was chosen to give an angular acceptance of $\pm 3^{\circ}$ and is limited by the diameter of the active area of the electron detector (2.84 cm). This angular resolution represents a compromise between limiting the variation in electron flight paths, which degrades the overall energy resolution, and insuring a sufficient collection solid angle (8.6×10^{-3} sr). Typical flight times for this distance are 480 nsec and 96 nsec for 1 eV and 25 eV electrons, respectively.

The drift tube is constructed from aluminum and provides the electrostatic shield for the field free flight path. The entire flight tube as well as the detector assembly is gold plated to eliminate contact potentials. In addition, the inside of the drift tube was coated with a colloidal graphite spray to reduce secondary electron emission caused by photoelectrons striking the walls of the shield. Magnetic shielding was provided by a coaxial μ-metal cylinder mounted around the flight tube. The residual magnetic field inside the drift space was measured to be less than 10 milligauss. The assembled analyzer is shown in Figure 3 and the individual components are exhibited in Figure 4. Figure 5 shows an aerial view of the instrument taken during an experiment at SSRL.

The electron amplifier is a tandem pair of microchannel plates (MCP) whose output is collected on a conical anode (Fig. 6). The MCP amplifier is similar in design to those recently employed for fast timing measurements of nuclear particles[10] and heavy ions[11,12] and the TOF electron detectors of Kennerly[13] and Bachrach, et al.[3] The general operating characteristics of MCP's and their timing capabilities have

been discussed in detail in the literature cited above and hence will not be repeated here. It is sufficient to note that because of the small time dispersion in a MCP's amplifying process, single particle events can be timed with a resolution of <100 psec.

The electrons which have drifted through the field free region are accelerated by 100 V before impinging on the first MCP. The MCP's electron detection efficiency is >96% and is uniform for input kinetic energies of 100 eV to 700 eV.[14] Two MCP's (Varian Series 8900, 40 mm diameter, 8° bias angle) in a Chevron arrangement were employed as the subnanosecond amplifier with up to 10^7 gain. Bias voltages from a divider chain (shown schematically in Figure 6) were applied to the front and rear conducting surfaces of each MCP through .05 mm thick gold-plate brass rings. The contact rings between the two MCP's were isolated by a .05 mm Mylar spacer, giving a total separation of .15 mm between the two MCP's. The emerging electron cascade is collected on a coaxial anode whose surface diameter (2.84 cm) determines the useful active area of the detector. The coaxial anode cone is designed to have the impedance of the anode increase from a minimum value of 16Ω at the collection surface to the output impedance of 50Ω. In this way a larger collection surface area is possible for a given MCP geometry than with a coaxial design in which the entire anode is fixed at 50Ω impedance. The anode shield is coupled to the back surface of the second MCP by a capacitor made from .5 mm double faced printed circuit board. The anode is at a virtual ground with respect to the anode shield, but the whole anode assembly is floated at the full positive high voltage potential. A fast coaxial transformer decouples the output signal to ground reference before

passing through a high vacuum floating-shield coaxial BNC feedthrough (Ceramaseal, Inc.).

At an applied voltage of 2.5 kV, the detector provides a gain of 10^6 and a dark noise count rate of 1 - 10 sec^{-1}. The output pulses are very sharp, with a 10% - 90% rise time of $\leqslant$.5 nsec. and pulse amplitudes of $\sim$75 mV.

Photoelectron spectra are generated by using the photon-electron coincidence counting circuit shown schematically in Figure 6. Pulses from the electron multiplier are amplified and discriminated, then used as a start signal for a time-to-amplitude converter (TAC). The stop pulse is provided by a signal from an induction coil located in the storage ring. This arrangement of stop and start signals avoids reset-time losses in the TAC. The pulse-height spectrum is then analyzed and accumulated in a multichannel analyzer.

c. Performance

The energy resolution for TOF analysis is given by[15]

$$\left(\frac{\Delta E}{E}\right)_{TOF} = \sqrt{\left(\frac{2\Delta t}{t}\right)^2 + \left(\frac{2\Delta \ell}{\ell}\right)^2} \qquad (1)$$

where Δt and $\Delta \ell$ represent the total time resolution of the apparatus and the electron flight path uncertainty, respectively. The time resolution of the TOF detector system is determined by the timing capabilities of the electron multiplier and associated electronics, folded together with the time width of the synchrotron beam pulse. Timing dispersion in the MCP amplifier and electronics is <70 psec. and the width (FWHM) of the synchrotron radiation pulse varies from 150 psec. to 400 psec.

depending on the operating conditions of SPEAR. Furthermore, the pulse shape is in general neither gaussian in time nor constant for different electron beam currents.[16] The overall timing resolution of the apparatus was measured directly by the observation of prompt (Rayleigh) photon scattering from the gas sample. A prompt pulse is shown in Figure 7. The measured FWHM of ∿300 psec. leads to an energy resolution contribution from timing factors of 40 meV at 10 eV and represents the limiting resolution of our TOF apparatus when employed at SSRL.

Differences in the photoelectron flight paths ($\Delta\ell$) result from the finite source volume and finite collection solid angle. The spread in electron flight paths due to the angular acceptance of $\pm 3^{\circ}$ contributes only a small energy uncertainly of .25%. A much larger contribution to $\Delta\ell$ results from the relatively large interaction volume from which the photoelectrons originate. With the present focusing optics on the 8° beam line, the photon beam cross section (FWHM) is 2.1 mm high by 4.2 mm wide at the interaction point. Furthermore, the experiments reported here were conducted at the "magic angle" (54.7° with respect to the photon polarization vector), hence, the horizontal beam profile at the source point is increased to ∿7.3 mm. This would correspond to a ∿5% resolution contribution if the electrons originated from the entire width of the beam. Due to the imperfect alignment of the photon beam and the highly collimated nature of the gas jet, however, the effective size of the interaction region is actually smaller. Hence, the 5% contribution represents an upper limit to the flight path uncertainty. Since this dispersion dominates the first term of Eq. (1) the energy resolution ($\Delta E/E$) is essentially constant over the kinetic energy range of 1 eV to 25 eV.

The total energy resolution is given by

$$\left(\frac{\Delta E}{E}\right)_{TOTAL} = \sqrt{\left(\frac{\Delta E}{E}\right)^2_{TOF} + \left(\frac{\Delta\lambda}{\lambda}\right)^2} \qquad (2)$$

where λ is the wavelength of the exciting radiation and $\Delta\lambda$ the monochromator band pass. The loss of intensity at higher resolution limited the usable band pass to 2.5 Å (∿90 meV at 21.2 eV photon energy) in the work presented here.

The TOF photoelectron spectrum of the 5p shell of atomic Xe at $h\nu$ = 23.1 eV is shown in Figure 7. This spectrum was recorded in only 5 minutes and represents the time-to-energy converted raw data. The marked asymmetry of the peaks towards lower energies is again due to the "magic angle" geometry employed. This results in the analyzer accepting more electrons with longer flight paths and hence apparent lower kinetic energies.

The resolution of 4% found for the $^2P_{3/2}$ peak is smaller than predicted by Eqs. (1) and (2), presumably because of an over-estimation of the interaction source width as discussed above. A resolution of ∿4% at 10 eV is comparable or better than that obtained with previous TOF electron analyzers. In the low energy (⩽2 eV) electron spectrometers of Tsai, et al.,[4] Land, et al.,[17] Baldwin,[18] and Wilden, et al.,[19] energy resolutions ($\Delta E/E$) of 10% at 50 meV, 6% at 150 meV, 13% at 1 eV and 3.3% at 1 eV, respectively, were reported. Because the resolving capabilities of those spectrometers are limited by the time resolution of the detector (5-12 nsec), only the first term of Eq. (1), i.e., $\frac{2\Delta t}{t}$, contributes significantly to the energy resolution. Hence, ΔE is

proportional to $E^{3/2}$ and their energy resolution will deteriorate rapidly with increasing kinetic energy. For detection of photoelectrons with energies greater than 1 eV, only the TOF apparatus of Kennerly[13] has better resolution than the present spectrometer (.67% at 12 eV). The time dispersions in both spectrometers are essentially identical (300 psec.), however a longer flight path (50 cm) and much smaller flight path uncertainty ($\Delta\ell$ = .1 cm) significantly improves the overall energy resolution obtainable by Kennerly.

To improve the resolution, a retarding grid assembly, shown in Figure 4, was added to the TOF analyzer. The higher resolving power is accomplished simply through reduction of the field free kinetic energy of the electrons. This assembly was utilized for the first time in the work discussed in Chapter V. As a result, the Ba^+ $[(5p^6 6s)-(5p^6 5d)]$ (600 meV) splitting is well resolved, and the Ba^+ $(5p^6\ 6p)\ ^2P_{3/2} - {}^2P_{1/2}$ fine structure (200 meV) is even discernible. Future improvements in resolution will be made by refocusing of the beam to a cross-section of 2.2 mm x 1.4 mm, thus reducing the path length dispersion, $\frac{2\Delta\ell}{\ell}$, from $\sim$5% to 1.5%.

REFERENCES

1. See for example, L. Torop, J. Morton, and J. B. West, J. Phys. B 9, 2035 (1976).

2. See for example, P. C. Kemeny, J.A.R. Samson, and A. F. Starace, J. Phys. B 10, L201 (1977).

3. R. Z. Bachrach, F. C. Brown, and S.B.M. Hagstrom, J. Vac. Sci. Tech. 12, 309 (1975).

4. B. Tasi, T. Baer, and M. L. Horowitz, Rev. Sci. Instrum., 45, 494 (1974).

5. P. M. Guyon, T. Baer, L.F.A. Ferreira, I. Nenner, A. Tabché-Fouhailés, R. Botter, and T. R. Govers, J. Phys. B 11, L141 (1978).

6. H. Winick, in VUV Radiation Physics, eds., E. E. Koch, et al. (Pergamon-Vieweg, London/Braunschweig, 1974), p. 780; V. Rehn, et al., in VUV Radiation Physics, eds., E. E. Koch, et al. (Pergamon-Vieweg, London/Braunschweig, 1974), p. 780.

7. Luxell Corporation, Santa Barbara, CA

8. J. C. Johnson, A. T. Stair, Jr., and J. L. Pritchard, J. Appl. Phys. 37, 1551 (1966).

9. R. H. Jones, D. R. Olander, and V. R. Kruger, J. Appl. Phys. 40, 4641 (1969).

10. M. I. Green, P. F. Kenealy, and G. B. Beard, Nucl. Instrum. and Methods 126, 175 (1975).

11. G. Gabor, W. Schimmerling, D. Greiner, F. Bieser, and P. Lindstrom, Nucl. Instrum. and Methods 130, 65 (1975).

12. J. Girard and M. Bolore, Nucl. Instrum. and Methods 140, 279 (1977).

13. R. E. Kennerly, Rev. Sci. Instrum. 48, 1682 (1977).

14. G. Gabor, to be published.

15. W. C. Wiley and I. H. McLaren, Rev. Sci. Instrum. 26, 1150 (1955).

16. A. P. Sabersky, in Abstracts of the Third Annual SSRP Users Group Meeting, Stanford, CA, 1976, p. 46.

17. J. E. Land and W. Raith, Phys. Rev. A9, 1592 (1974).

18. G. C. Baldwin, Phys. Rev. A9, 1225 (1974).

19. D. G. Wilden, P. J. Hicks, and J. Comer, J. PHys. B 9, 1959 (1976).

FIGURE CAPTIONS

Fig. 1. Lay-out of the TOF photoelectron spectrometer. See text for detailed description.

Fig. 2. Relative transmitted intensity versus photon wavelength for the 8° beam line at SSRL employing In and Al windows.

Fig. 3. The assembled TOF analyzer.

Fig. 4. The disassembled TOF analyzer, showing the μ-metal shield, detector/retarding grid assembly, and aluminum drift tube.

Fig. 5. Aerial view of the TOF apparatus on-line at SSRL. From left to right:

1) Al window
2) TOF analyzer assembly
3) Gas inlet mounted on manipulator
4) Turbomolecular pump
5) Photomultiplier used for monitoring photon flux

Fig. 6. Schematic of the TOF analyzer and associated electronics. A = 1MΩ, B = 422kΩ, C = 1MΩ, D = 619kΩ, E = 750kΩ; the voltage divider and power supply were potted in thermally conducting epoxy and were heat sunk to the detector support stalk. MONO = 8° line monochromator. CS = ceramic spacer. MS = mylar spacer. MCP = 40 mm diameter microchannel plate. DC = decoupling capacitor. CA = coaxial anode. DT = decoupling transformer. CFD = constant fraction discriminator. Attn = 0-100 db. attenuator. DD = differential discriminator. TAC = time-to-amplitude converter. PHA/MCA = combination pulse height analyzer and multichannel analyzer.

Fig. 7. Prompt signal resulting from Rayleigh photon scattering from the gas sample. The shape of the prompt signal and FWHM of 300 psec. are characteristic of the synchrotron radiation pulse.

Fig. 8. TOF photoelectron spectrum of the 5p shell of atomic Xe.

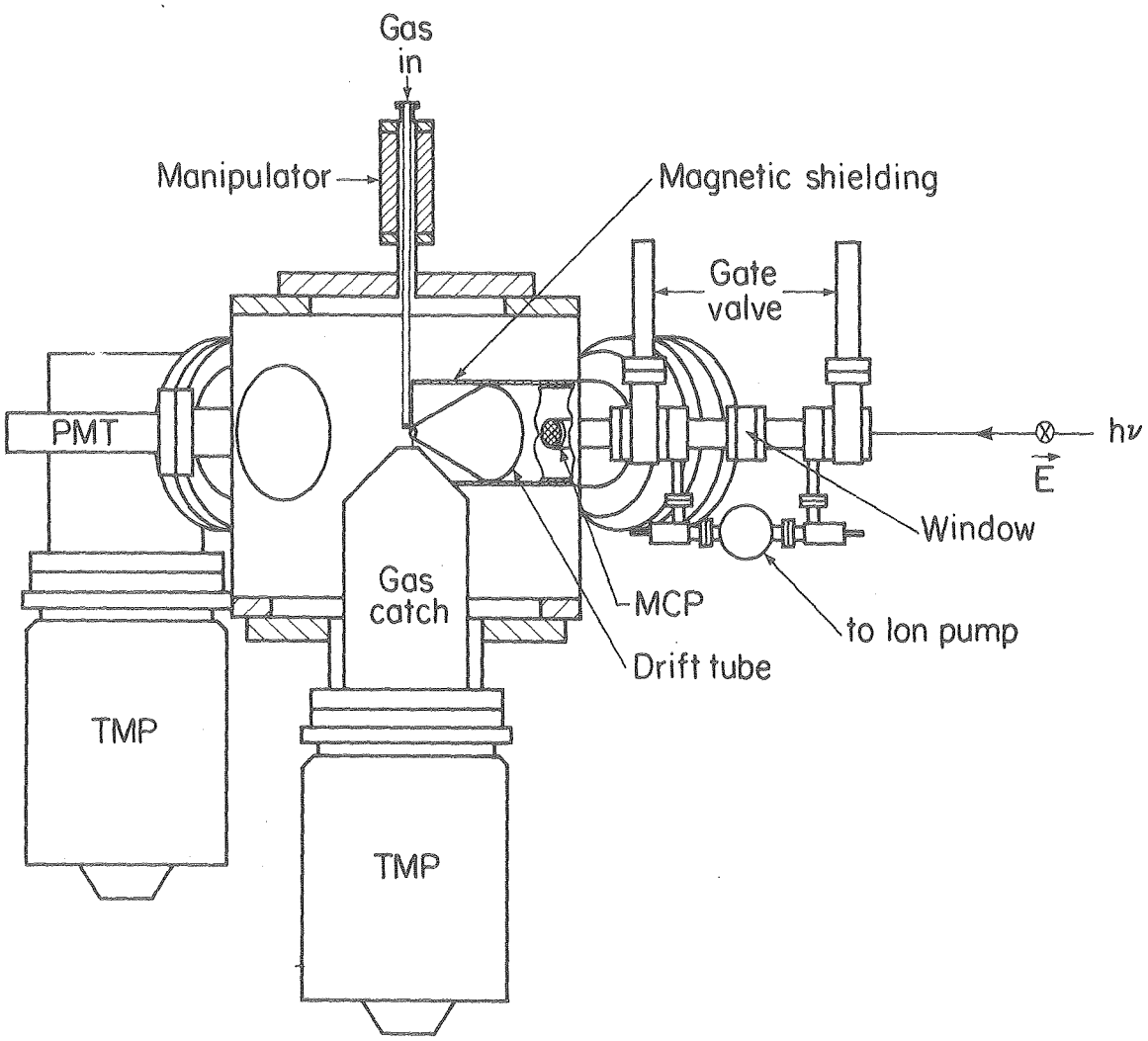

XBL 792-8566

Fig. 1

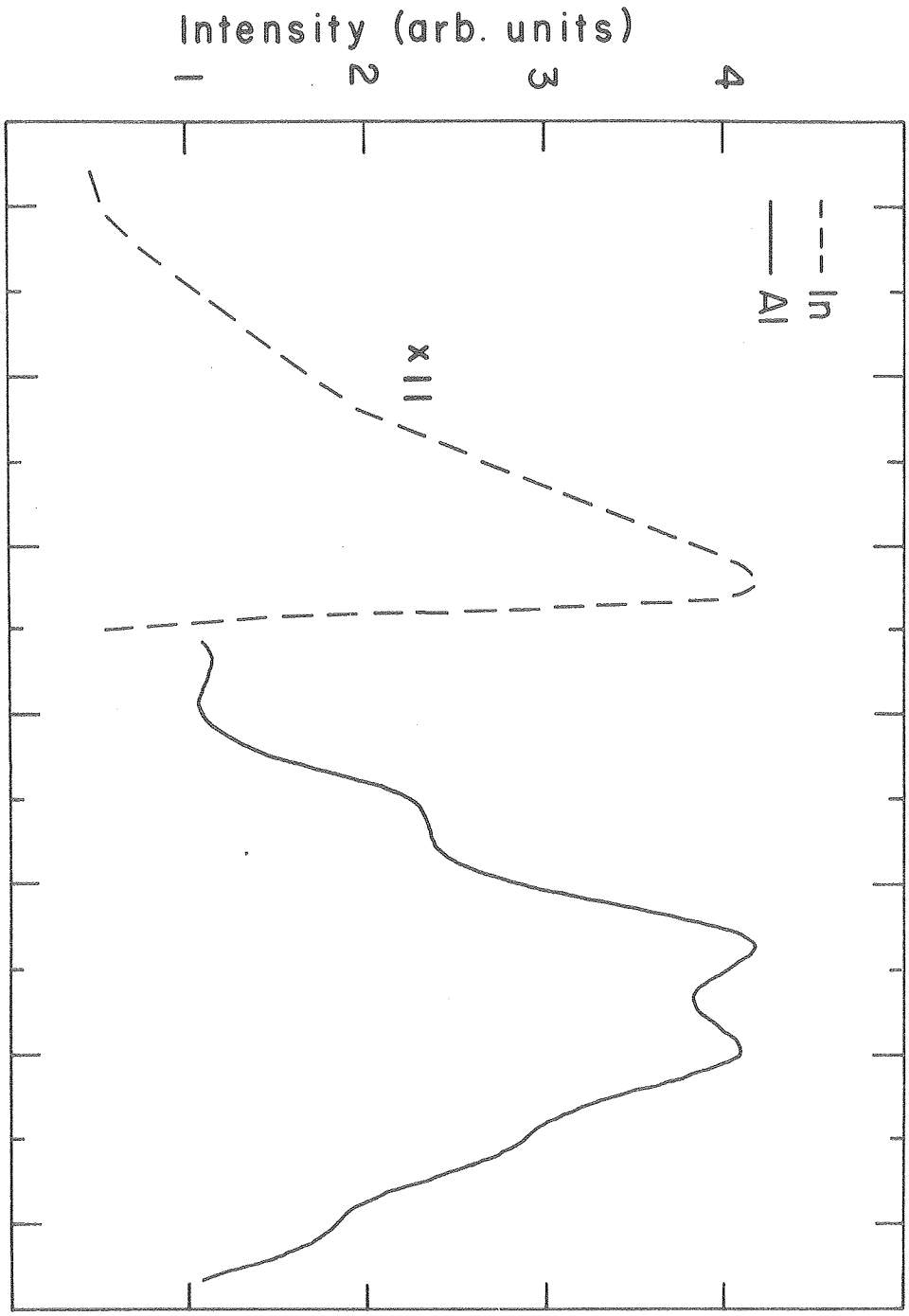

XBL 7810-11701A

Fig. 2

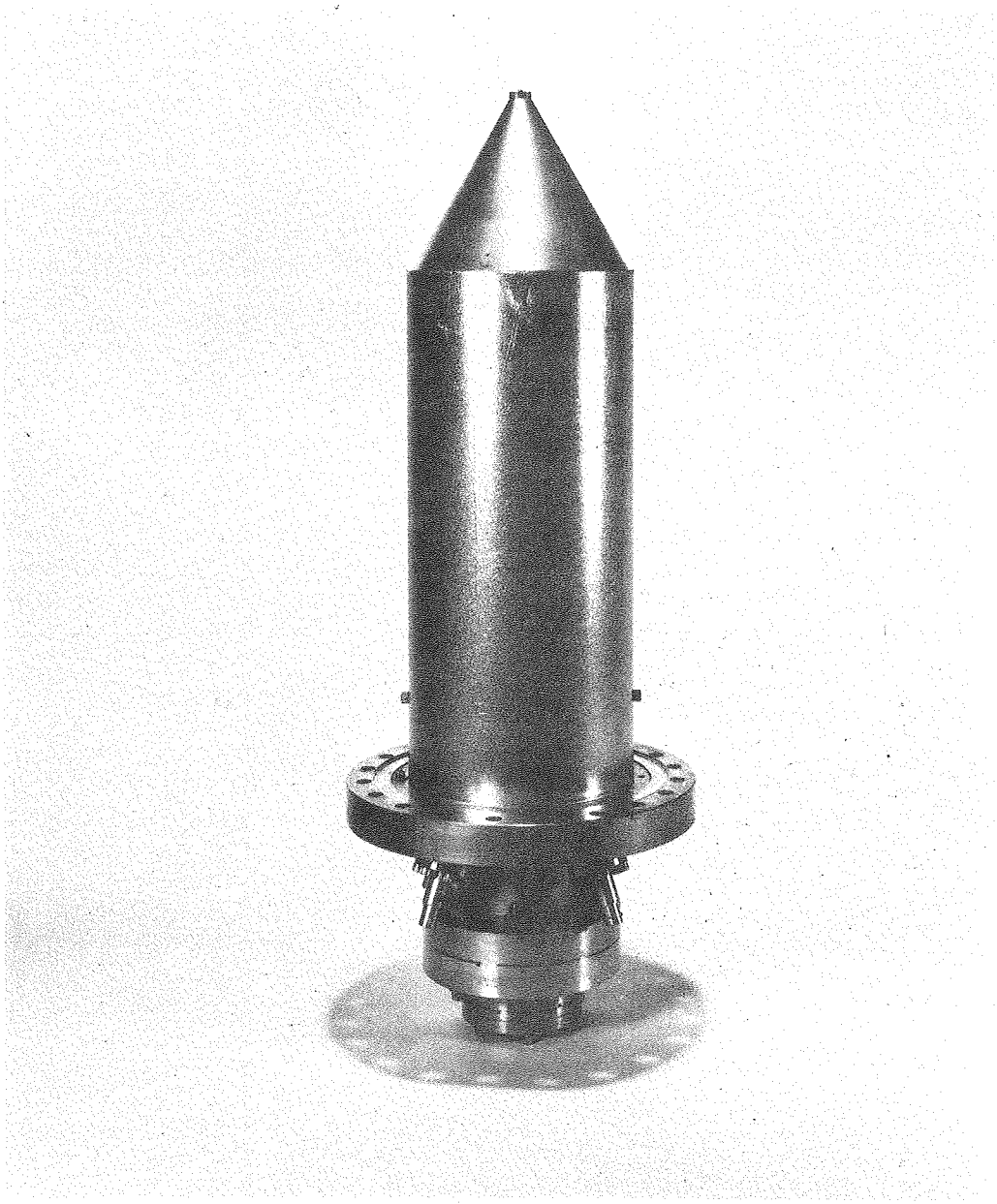

CBB793 3978

Fig. 3

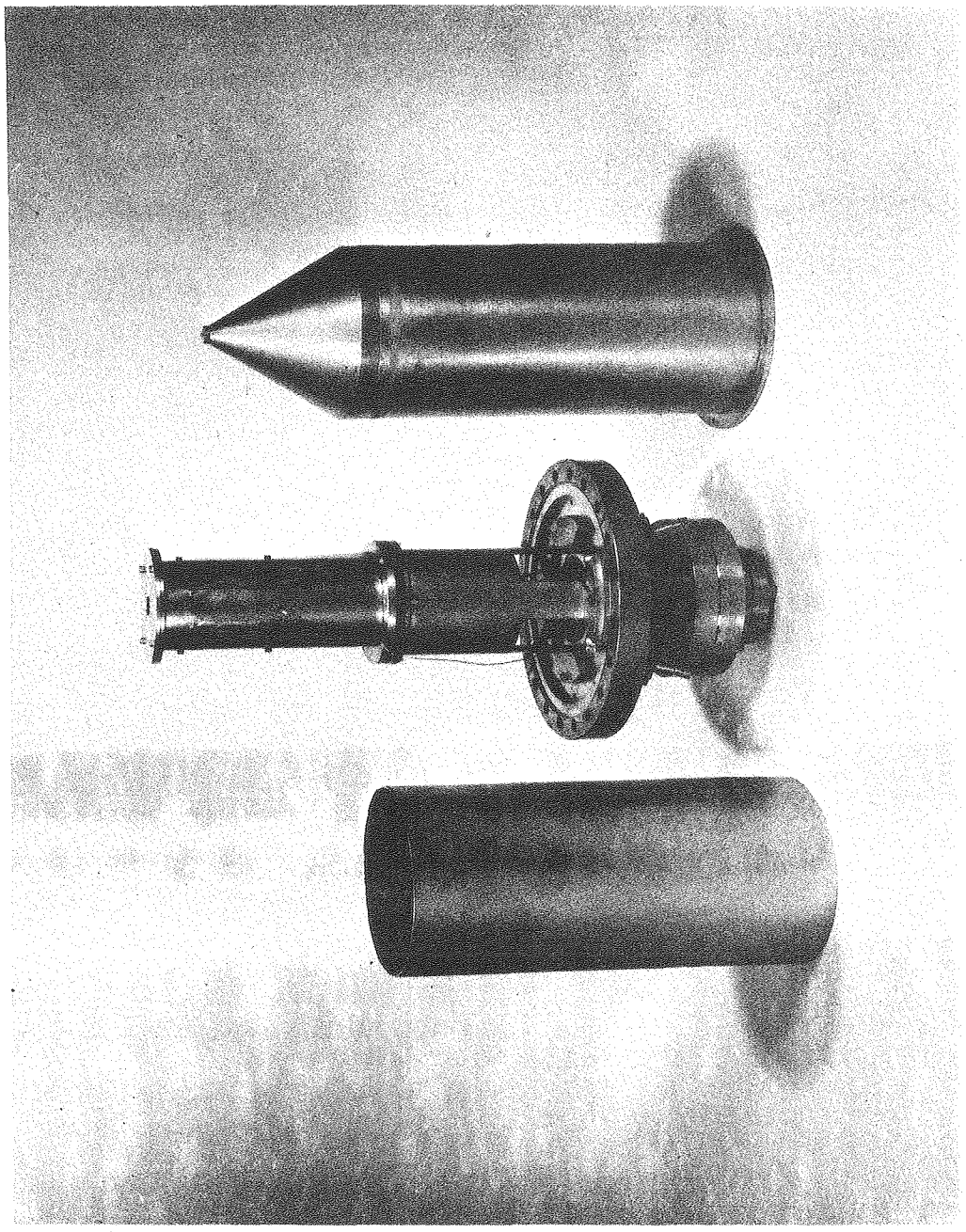

CBB793 3980

Fig. 4

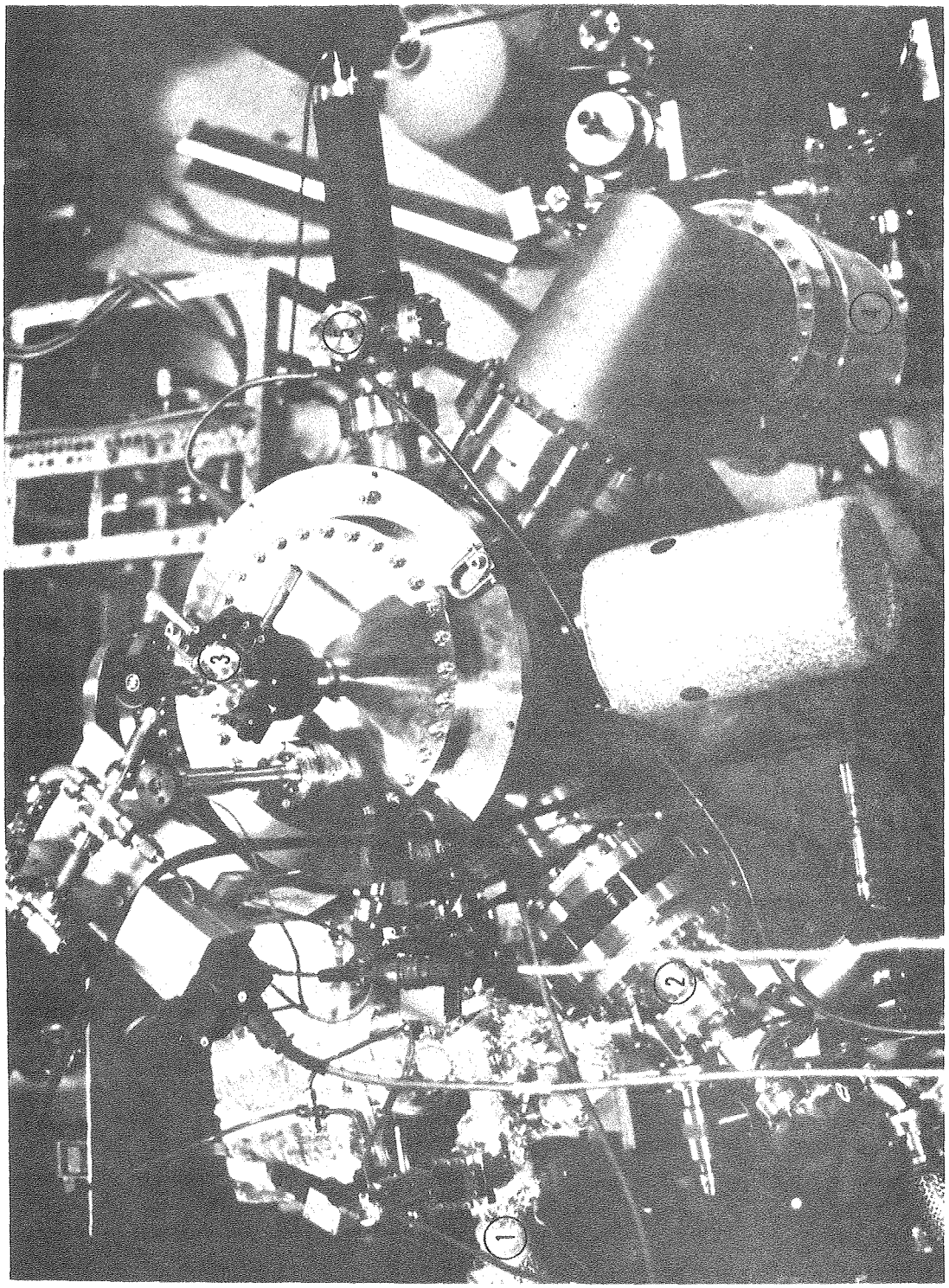

CBB794 5650

Fig. 5

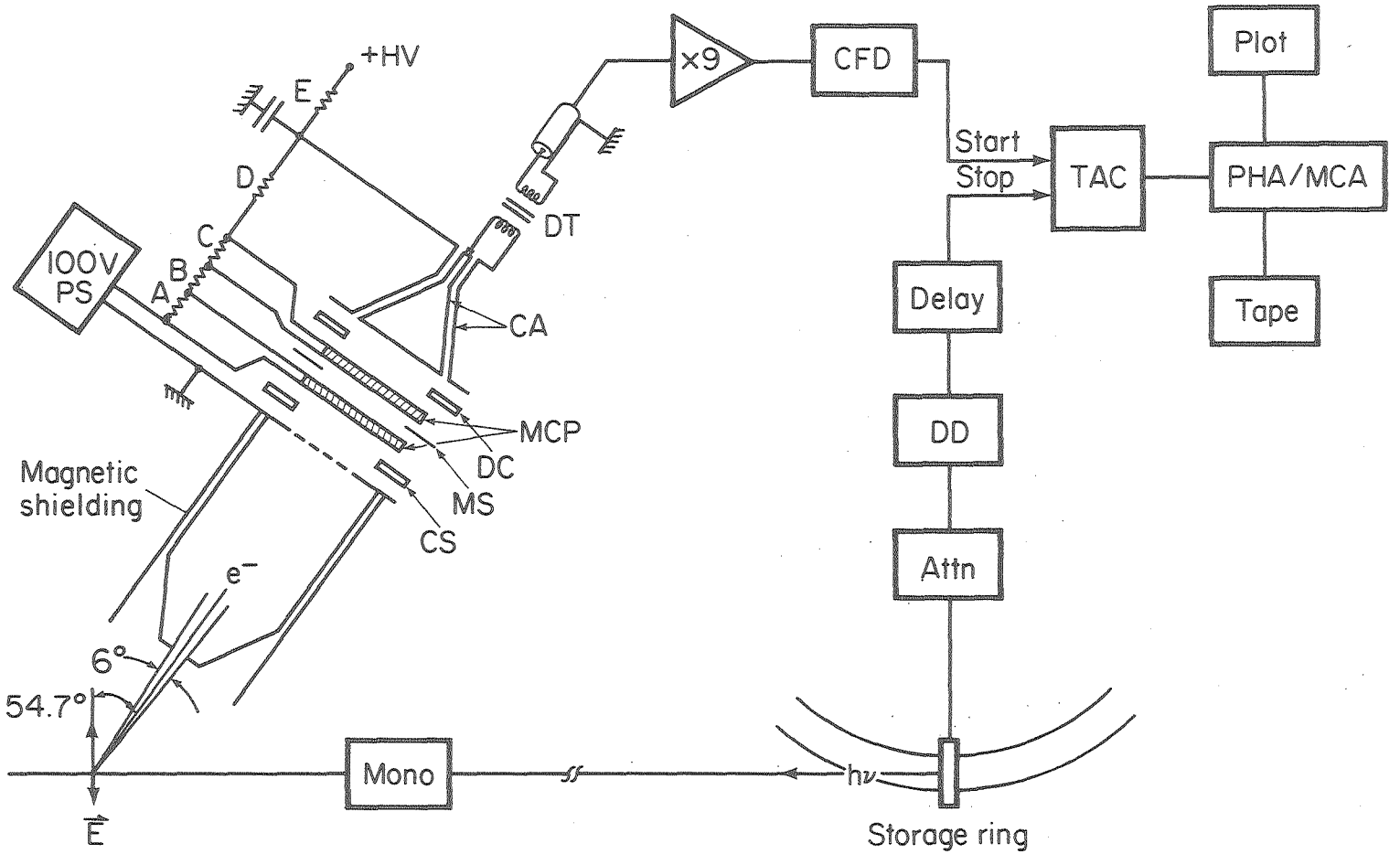

XBL 792-619

Fig. 6

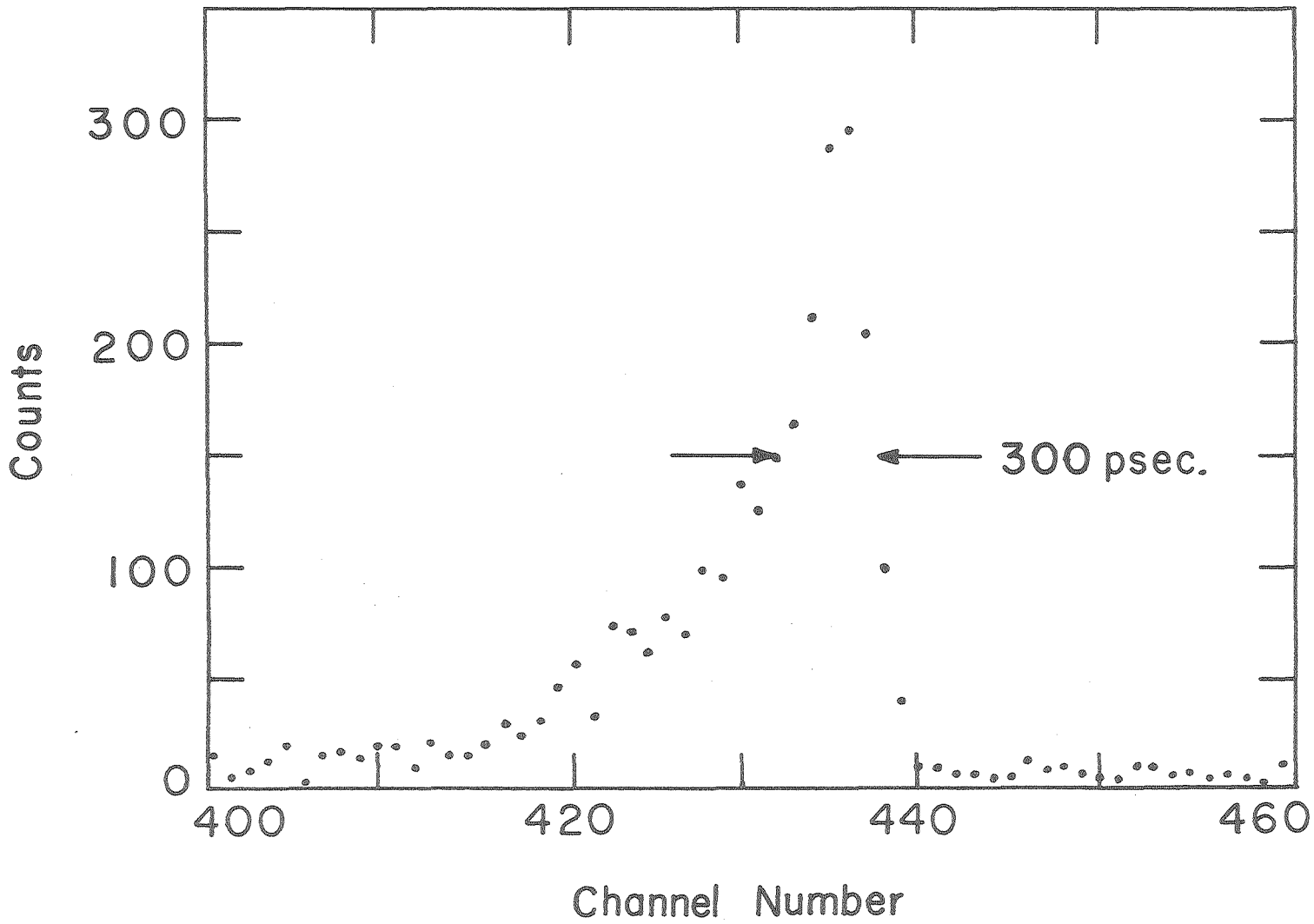

XBL 792-8565

Fig. 7

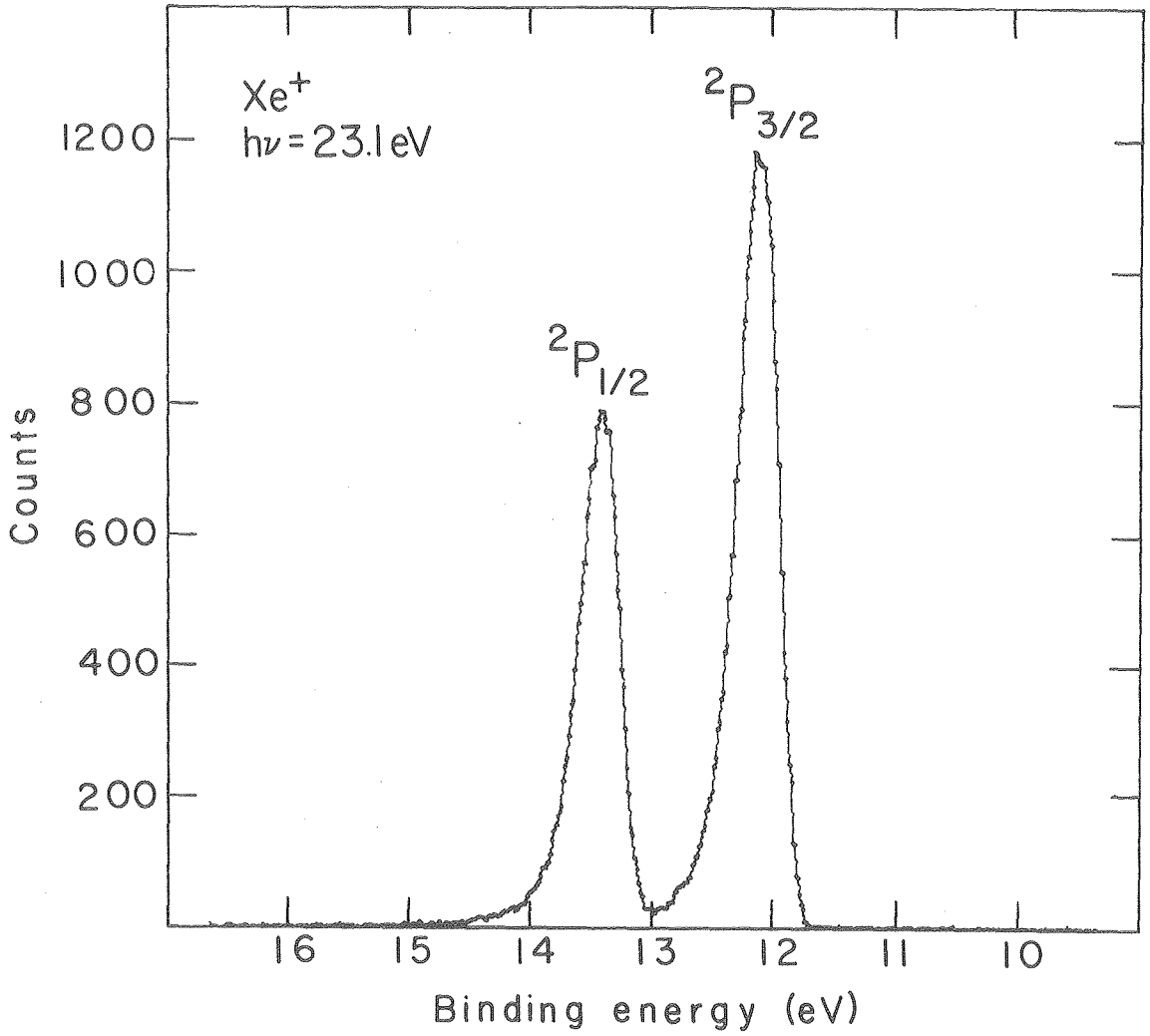

XBL 789-10742A

Fig. 8

4. The High Temperature Effusive Beam Source

As mentioned above, a primary objective of this work was to study, at SSRL, the photoelectron spectra of Ba and other high temperature species at SSRL, in particular Ba. For reasons previously discussed (Section II A), the oven source of Süzer[1] was found unsatisfactory for this purpose. The philosophy behind the design of the new source may be stated as follows.

1. Correct the deficiences inherent in the previous design, i.e. inductive effects, thermal electrons, and collimation.
2. Make the design simple and easy to assemble, so in the event of component failure, repair or replacement could be made using equipment existing at SSRL.
3. Provide for simultaneous inlet of a calibration gas.

The latter criterion was met in the design, but the facility was not used due to the loss of service of the TMP's (section II A).

The remaining two items were adequately satisfied by the source shown schematically in Figure 1. This plan takes advantage of some aspects of earlier designs.[3]

Collimation and containment of the vapor was achieved by the micro-capillary array (MCAP)[3]/cold finger arrangement. The liquid-nitrogen cooled cold finger was fed by a "chicken feeder" and the complete assembly was mounted on a gimble (flexible bellows) to allow alignment of the cold finger with respect to the oven. The presence of the boron nitride piece provided for the possibility of floating the oven electrically (to retard the thermal electrons) and also served to prevent thermal losses. Since the analyzer retarding grid system was available, a small

negative voltage (1-2 volts) prevented the thermal electrons from reaching the detector and therefore the oven was externally grounded during the experiment. All the other parts were machined of stainless steel or tantalum, easily assembled, and easily cleaned.

Sample heating was accomplished by use of a Semflex heating cable[4] coiled around the sample chamber (see Figure 1). The cable consists of two Ni-Cr alloy wires separated by an insulating layer of highly compacted magnesium oxide and surrounded by a sheath of Inconel 600. The cable utilized in this work was .093 inches in diameter and the wires were .015 inches in diameter. The coil was tightly wound near the top of the sample chamber to insure that this area was the hottest part of the system (to prevent obstruction in the MCAP). In this arrangement D. C. current is passed through one wire to the tip of the coil, where the two wires were TIG welded together, and then out through the other wire. Hence, the inductive effect of one wire cancelled out that of another. A ceramic bead was placed on the tip to prevent electrical shorting. Heat shielding consisted of a cylinder of .004 inch Ta foil, which was "dimpled" to prevent thermal losses. An additional cylinder placed around the top also served to keep the MCAP hot.

The wire in the coil is capable of withstanding temperatures of up to 1150° C. In practice, the coil was found to melt at approximately 1000° C. The coils had approximately 13 turns. For the results presented in Chapter V, the oven was operated at roughly 850° C, as measured by an optical pyrometer. This corresponded to an input power of 78 watts (2.6A x 30V).

The sample was loaded in a S.S. crucible and inserted into the sample chamber. A S.S. cap with a 1/8 inch orifice contained the MCAP and was secured to the chamber by a 1/16 inch S.S. rod. The boron nitride insulator was then attached to the bottom of the chamber with S.S. screws (0-80). After the coil and heat shielding were mounted, the entire source was attached to the end of the gas inlet tube. This assembly (Figure 2) was then mounted on an XYZ manipulator mounted on a 10-inch flange on the bottom of the vacuum chamber. Electrical connection to the coil was made via a UHV electrical feedthrough and wire insulated with ceramic beads.

Laboratory measurements using Ba as a sample indicate that a sample density of approximately 10^{-3} torr may be achieved at 1000° C. At this temperature, Ba has a vapor pressure of nearly 10 torr. For the work reported in Chapter V, the oven was operated at ∿850° C, giving a vapor pressure of 1 torr Ba, which implies a sample density of ∿10^{-4} torr.

An end-on view of the source is shown in Figure 3. In Figure 4 is seen an expanded view of the assembled sample chamber, heating coil, and heat shielding. Figure 5 shows the individual components of the sample chamber. The source, cold finger, and TOF analyzer are featured in Figure 6 and Figure 7 shows the entire system mounted on the vacuum chamber.

REFERENCES

1. Sefik Süzer, PhD. Thesis, University of California (1976) LBL-4922.

2. J. P. Connerade, Nucl. Instr. and Methods, 152, 271 (1978).

3. Type 304 stainless steel, Brunswick Corp., Bridgeport, Conn.

4. SEMCO, Inc., Hollywood, California.

FIGURE CAPTIONS

Fig. 1. Schematic of the High Temperature Effusive Beam Source.

Fig. 2. Assembled source mounted on the end of the gas inlet tube. At the bottom of the tube is the flange used to mount the assembly on the XYZ manipulator, as well as the on-off valve used for admitting calibration gases.

Fig. 3. End-on view of the effusive source. Starting from the outside are pictured the two Ta heat shields, the heater cable with ceramic insulating bead, the stainless steel cap with 1/8 inch orifice, and the s.s. microcapillary array.

Fig. 4. From left to right: Ta heat shields, heater coil with electrical connectors; the assembled sample chamber.

Fig. 5. Expanded view of the sample chamber. From left to right: boron nitride insulator (bottom of chamber) and 0-80 screws used to attach insulator; s.s. sample chamber (top) and crucible (bottom); s.s. microcapillary array; 1/16 inch S.S. rod used to secure cap to chamber; s.s. cap (top of chamber).

Fig. 6. The liquid nitrogen cold finger (top), TOF analyzer (middle), and high temperature source bottom. The analyzer is situated at 54.7° with respect to the $\vec{E}$ vector (perpendicular to the page).

Fig. 7. Overall view of the TOF chamber modified for high temperature work. At the top of the chamber is the "chicken feeder"/LN cold finger arrangement mounted on a gimble for alignment. The TOF analyzer is in the middle and perpendicular to the plane of the page. The TMP shown on the elbow to the right was not used during the experiment due to Ba vapor contamination.

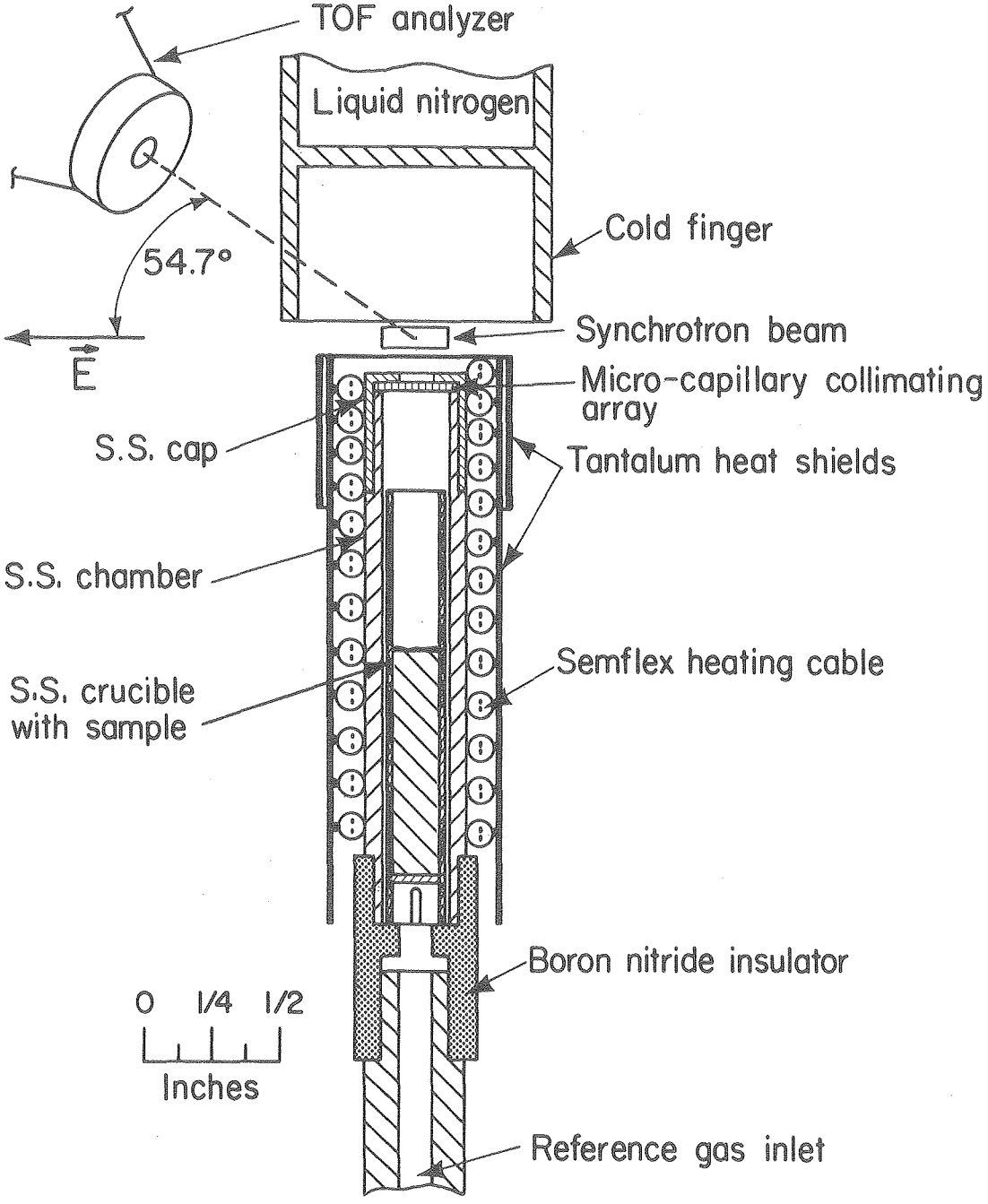
TOF analyzer
Liquid nitrogen
Q
54.7°
Cold finger
E
Synchrotron beam
Micro-capillary collimating array
S.S. cap
Tantalum heat shields
S.S. chamber
Semflex heating cable
S.S. crucible with sample
Boron nitride insulator
0 1/4 1/2
Inches
Reference gas inlet
XBL 794-1129

Fig. 1

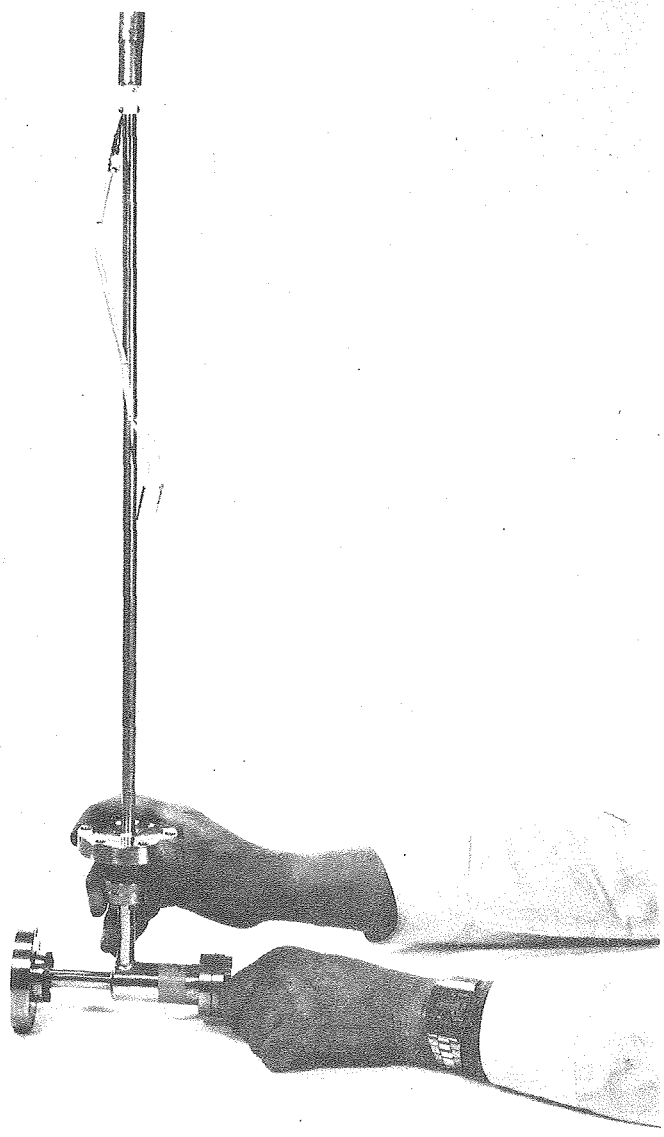

CBB793 3990

Fig. 2

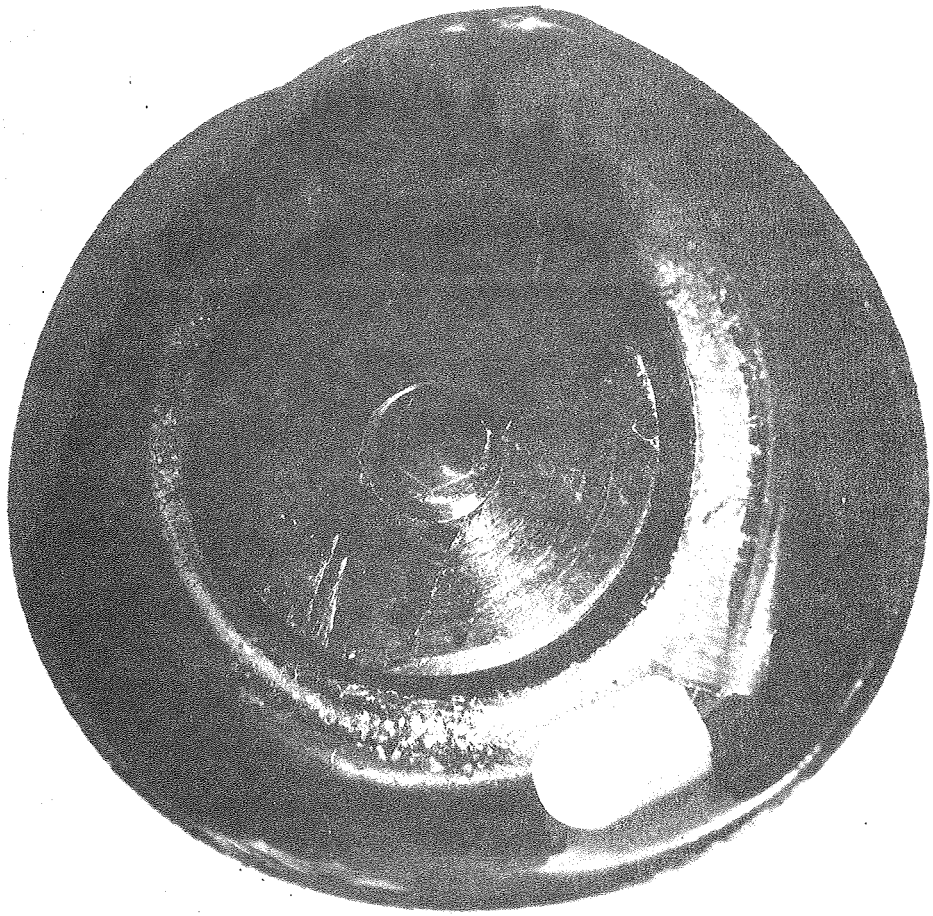

CBB793 3988

Fig. 3

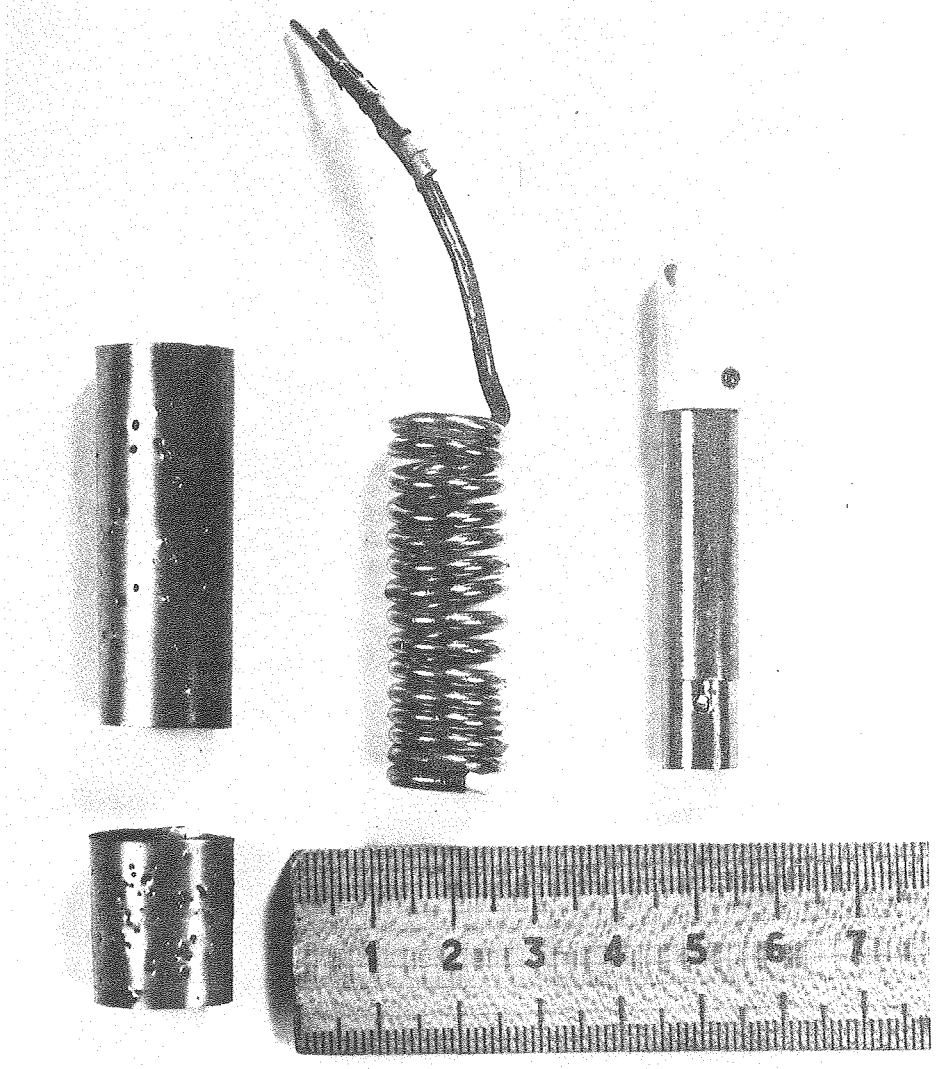

CBB793 3986

Fig. 4

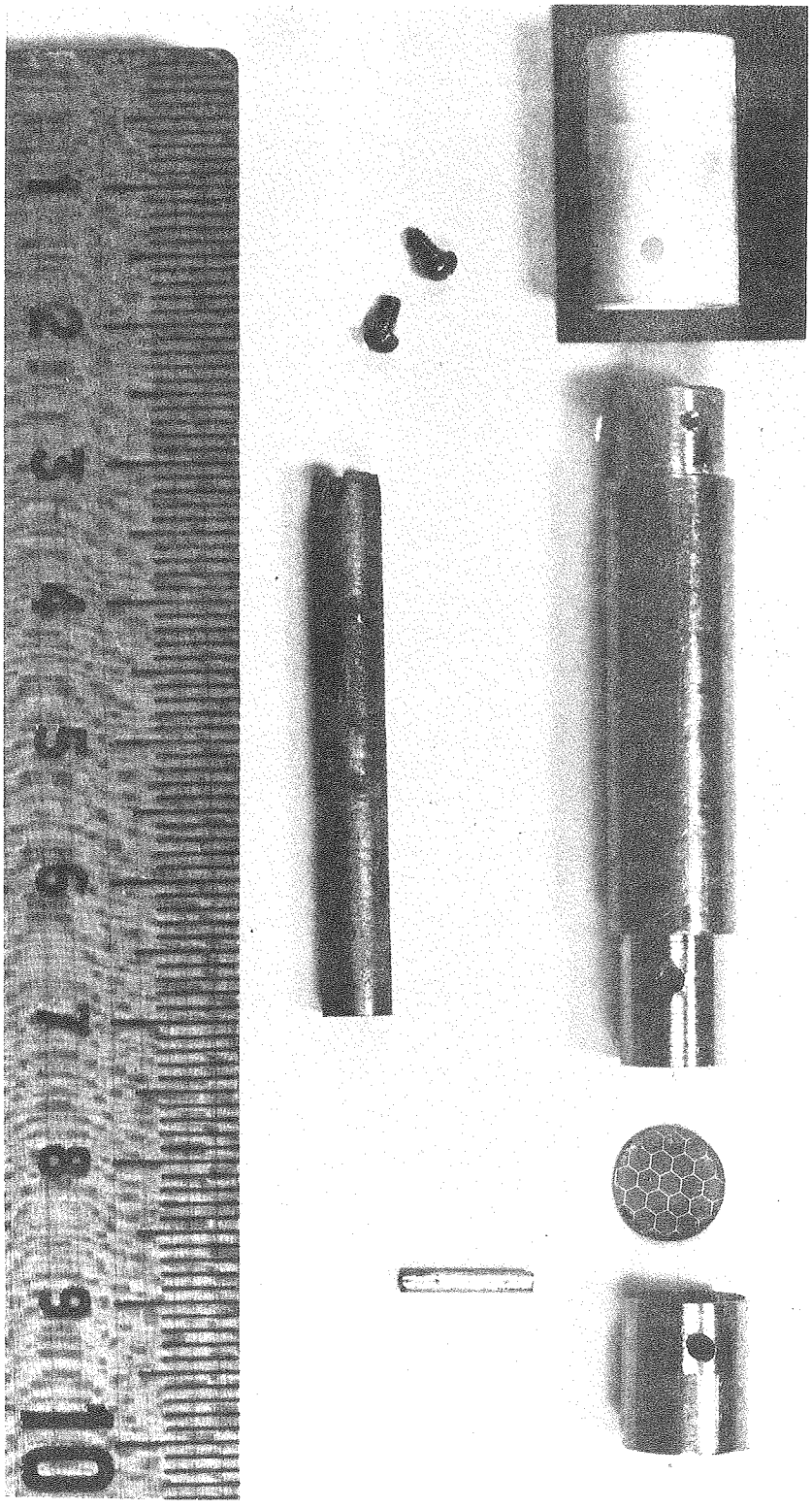

CBB793 3992

Fig. 5

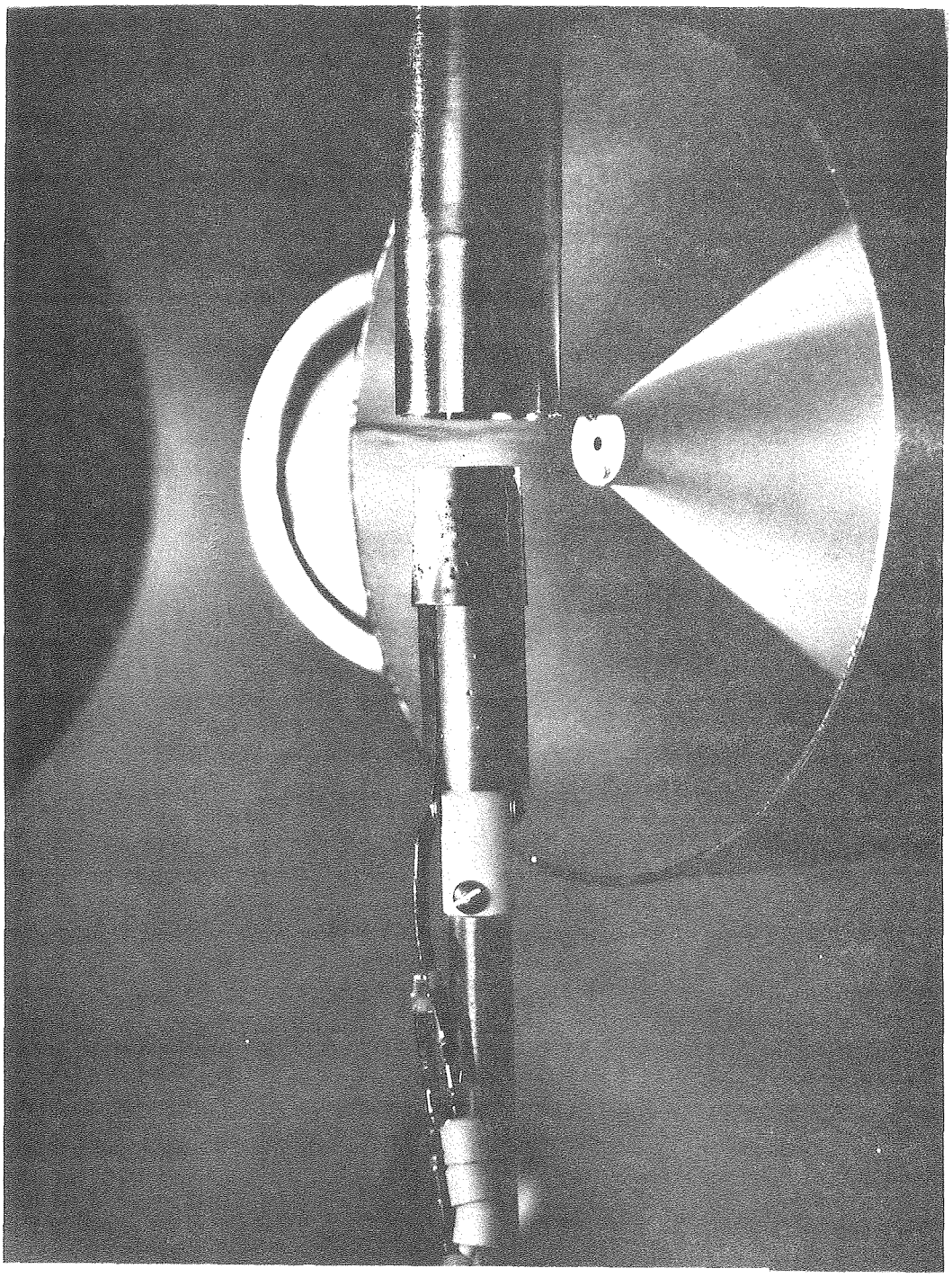

CBB795 6223

Fig. 6

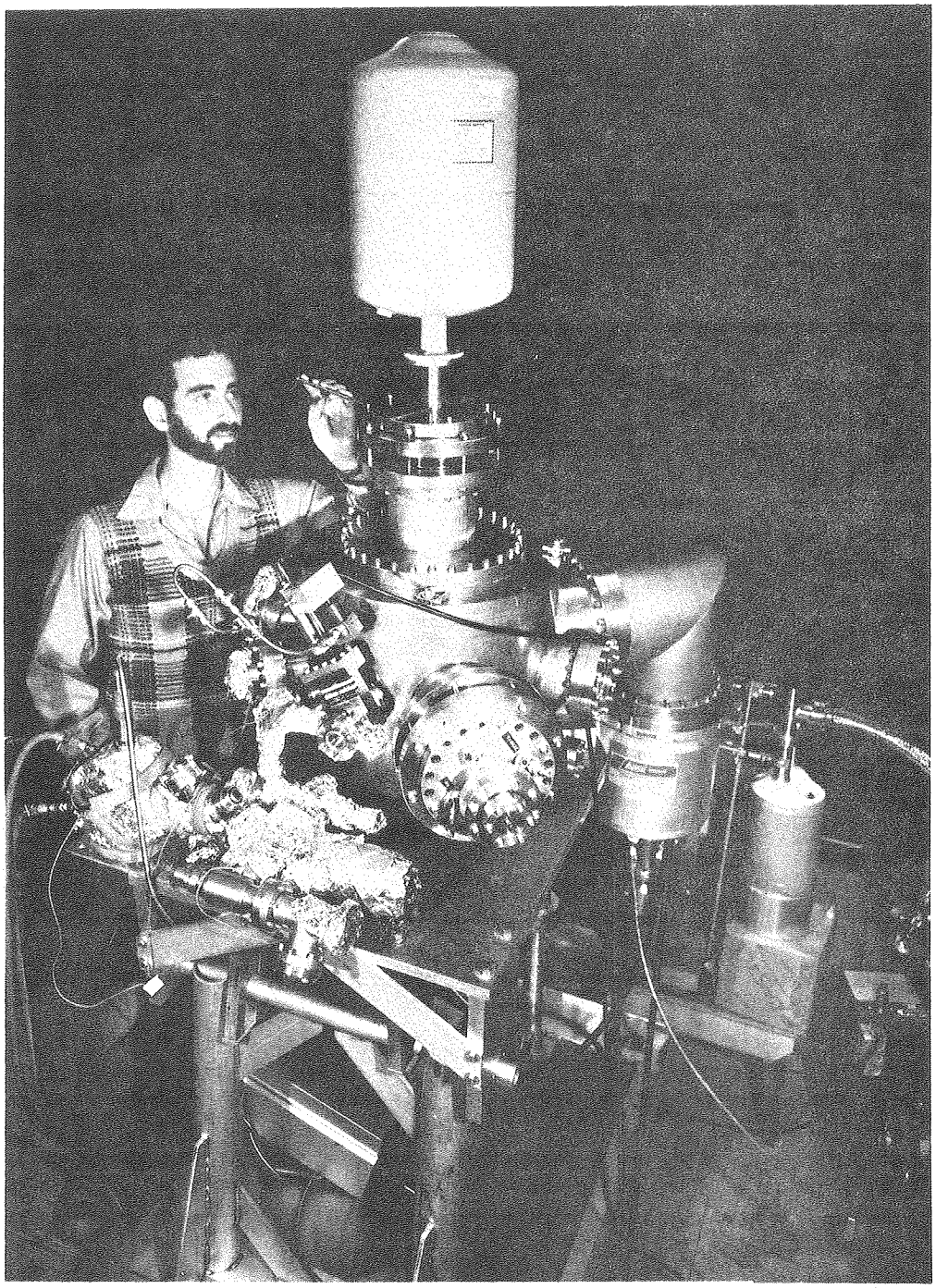

CBB795 6227

Fig. 7

5. People

Since experiments at SSRL are run continuously, it is impossible for one or even two people to carry them out alone. The following two figures show the people who made important contributions to many of the results presented here.

FIGURE CAPTIONS

Fig. 1. From left to right: Mike White, Erwin Poliakoff, and Shuit-Tong Lee during one of the first fluorescence experiments at SSRL.

Fig. 2. From left to right: the author, Steve Southworth, Mike White, and Geoff Thornton during the monochromatized fluorescence experiment at SSRL.

CBB794 5654

Fig. 1

CBB794 5648

Fig. 2

III. CONFIGURATION INTERACTION EFFECTS IN THE ATOMIC PHOTOELECTRON SPECTRA OF Ba, Sm, Eu, and Yb*

ABSTRACT

High temperature photoelectron spectra of Ba, Sm, Eu, and Yb were studied using both HeI and NeI resonance lines. In addition to strong lines corresponding to transitions from the primary configurations, correlation satellites were observed in every spectrum. By comparing the spectra excited at different photon energies, the satellite lines found in all NeI spectra and the HeI spectrum of Yb were attributed to admixtures of the configurations $5d^2$, $6p^2$, etc., into the ground state. Autoionization is believed to occur at the energies of the HeIα, HeIβ and NeI satellite lines for Ba, at the HeIα energy for Sm, and at the HeIα and HeIβ energies for Eu. Autoionization was detected by noting the dramatic increase in satellite intensities and, in some instances, the large deviation of the observed intensity ratios within multiplets from the statistical values. Photoelectron spectroscopy has been demonstrated to have great potential in providing detailed information about electron correlation in both initial and final states.

---

*Paper published with co-authors S.-T. Lee, S. Süzer, E. Matthias, and D. A. Shirley, J. Chem. Phys. 66, 2496 (1976).

A. Introduction

The origin of satellite lines due to electron correlation in photoelectron spectra has recently been discussed[1,2] using the model of configuration interaction (CI). Photoionization causes a transition from an initial state of an N-electron system to a final state composed of an (N-1)-electron ion and the free electron. Within the context of a particular basis set, the intensities of the correlation satellites can derive contributions from configuration interaction in the initial (ISCI) and/or final state. For pedagogical purposes, final-state CI can further be classified as final ionic CI (FISCI),[1,2] continuum state CI (CSCI),[2] and autoionization.[3] Among these four mechanisms leading to satellites, autoionization is readily distinguishable because of its resonant nature. The distinction among the other three is not so straightforward; indeed this distinction is unique only within the context of a particular basic set. In the case of the Ne 1s satellites, elaborate CI calculations were necessary in order to establish the major contributions from ISCI and FISCI, and to bring the calculated intensities into agreement with experiment.[4] However, in certain atomic cases, ISCI can be regarded as the sole dominant contributor to the satellites[5] simply on the grounds of symmetry and near-degeneracy of states. Therefore, ISCI was found predominantly responsible for the satellites in the photoelectron spectra of Pb,[6] Bi,[7] and Group-IIA and -IIB elements.[5,8,9] Particularly in these latter cases, satellite structure can provide unique information about the nature and extent of electron correlation effects in the ground states of atoms.[5]

Continuing our work with metal vapors, we have made a similar study on some rare-earth metals. Because of the similar valence-electron configurations of the rare-earths and the alkaline earth metals, we expect to find ISCI satellites in the photoelectron spectra of the former as well. Furthermore, it is interesting to see what effects the incompletely-filled 4f-shell will have on the satellites.

Recent studies, both experimental[10-12] and theoretical,[13,14] have suggested that resonant autoionization might be responsible for the remarkably high intensities of satellites and the large ratio of double to single ionization in the photoelectron spectra of Ba excited by HeIα(21.22eV) line. The resonant absorption at HeIα energy is further demonstrated by comparison to the NeI spectrum of Ba[5], and by the UV absorption spectrum of Ba in the 800-500 Å region.[15,16] The Rydberg-like state reached by the HeIα line must involve one of the $5p^6$ electrons, on energy grounds, possibly a state like $[5p^5\ 6s^2(\text{nd or ns})]_{J=1}$. Proceeding from Ba to the lanthanides, because of the rather effective screening of the additional nuclear charge by the accompanying additional 4f-electrons, we expected the threshold of 5p ionization to increase only gradually with the filling of the 4f shell. Therefore, it was anticipated that the HeIα line would be close to the 5p threshold, and that resonant absorption might occur at HeI resonance energies for some lighter lanthanides. In light of the above discussion, it might thus be possible to extend the observation and study of autoionization with laboratory source from barium into the lanthanides.

In this paper, we report the observation of satellites in the UV photoelectron spectra of Ba, Sm, Eu, and Yb. By analysis of the spectra provided by the various He and Ne resonance lines, satellites due to ISCI and autoionization have been differentiated.

Experimental information is given in Section II, and results and assignments are given in Section III. In Section IV these results are discussed in terms of autoionization and other mechanisms. Conclusions are drawn in Section V.

B. Experimental

The experimental procedure is identical to that reported earlier.[5,6] Briefly, the spectra were taken with a modified Perkin-Elmer PS-18 photoelectron spectrometer. The samples were loaded in air in a stainless steel container which rested inside the ionization chamber that was heated by a tantalum oven. Because of continuous deposit and oxidation of the metals on critical surfaces, the resolution of the electron analyzer could vary considerably during a run, which lasted between one and ten hours with a single sample load. The resolution also changed with the electron energy, and ranged between 60 and 150 meV for 9 eV electrons as monitored by the Xe $^2P_{3/2}$ line. Energy calibration was done by measuring Xe and N_2 photoelectron lines together with the sample, and also by using the documented first ionization potentials of the metals. All samples were obtained in purities of 99% or higher from commercial sources.

Intensities of lines were taken as the peak areas divided by their kinetic energies (thereby correcting for the theoretical transmission function of the analyzer). No correction was made for the

dependence of transmission upon charging effects and inelastic scattering; nor has the effect of photoelectron angular distribution been taken into account. Therefore the reported intensities bear large uncertainties and are only included for qualitative discussion. However, the relative intensities of lines that lie nearby in energy in the same spectrum are expected to be quite reliable. In the case of Ba, HeII and NeII lines were necessary to ionize the 5p electrons. These more energetic lines were produced using a hollow cathode lamp.[17]

The temperatures at which the spectra were recorded are: Ba/HeI (620°C), Ba/NeI (700°C), Sm/HeI (640°C), Sm/NeI (730°C), Eu/HeI (740°C), Eu/NeI (740°C), Yb/HeI (650°C), and Yb/NeI (600°C). The thermocouple which monitored the temperature was in contact with the colder part of the oven;[6] hence the actual sample temperatures may be up to 30°C higher than those given.

C. Results and Assignments

The spectra of Ba, Sm, Eu, and Yb are displayed respectively in Figs. 1-4, with the prominent lines labelled. The peaks marked S are assigned to photoemission induced by HeI or NeI satellite lines and those denoted I are inelastic loss peaks of the intense lines involving the $6s \rightarrow 6p$, $\Delta S = 0$ and $\Delta L = 1$ transitions. The results and derived parameters are collected in Tables 1-4, and Table 5 gives the energies and relative intensities of the HeI and NeI lines produced in our lamp. Except as noted, the photoelectron lines were identified by comparison with the ionization potentials from optical work.[18] The spectra of the four elements are discussed separately below.

1. $\underline{Ba(6s^2;{}^1S)}$

In agreement with previous workers,[11,12] the HeIα spectrum of Ba (Fig. 1a) shows a large number of excited ionic states with remarkably high intensities. With better statistics, we have been able to positively detect and identify several new lines in the energy range 13-15 eV (Table 1). All lines below 14.2 eV are associated with the Ba^+ states of $5p^6n\ell$ configurations, with ℓ representing s, p, d, f, and g orbitals and the number n going as high as 10 for s and p orbitals. The lines numbered 4-10 may be assigned similarly to the higher Rydberg states ($5p^6n\ell$) of Ba^+ leading to the threshold of Ba^{++} at 15.215 eV,[18] as proposed previously,[11] but alternative assignments may be possible, as discussed later (Section IVD). The nature of the three intense lines lying above the threshold of Ba^{++} has been unequivocally established by Hotop and Mahr[12] as arising from two-step double ionization, forming Ba^{++}. The peak at 3.34 eV and the doublet at 4.0 eV are the 6s and 5d states of Ba^+ reached by the HeIβ line.

The NeI spectrum above 3 eV has been reported earlier,[5] but is included here for comparison and to show the ionization due to other, weaker NeI lines. Except for the 6s Ba^+ ground state, only 5d, 6p, 7s, 6d, and 4f states are positively detected and are of much lower intensity relative to the 6s line in HeIα spectrum. The lines in the 1-3 eV range (Fig. 1b) cannot be assigned to any states of Ba^+ resulting from excitation by the NeI doublet. These lines have been reproduced in two independent runs and the possibility of their arising from impurities having 2-3 eV binding energies is very small. We attribute these peaks to 5d and 6s Ba^+ states excited by the weak NeI satellite lines between

19.69 and 21.11 eV (Table 5). These peaks are broadened and coalesced by the instrumental resolution.

Ionization of Ba by HeII (40.8 eV) and NeII (26.9 eV) has also been studied in an attempt to determine the $(5p)^{-1}$ threshold. In both spectra, a peak corresponding to a binding energy of 22.7 eV was detected. This peak is assigned to the ionic state $(5p^5 6s^2; {}^2P_{3/2})$ by comparison to a $(5p)^{-1}$ hole state relativistic Hartree-Fock calculation using the Desclaux program,[19] which gave $(5p_{3/2})^{-1}$ hole states at 22.15 and 24.28 eV respectively. The assignment is further corroborated with the results obtained from the Auger spectrum of Ba,[20] which gave the $(5p_{3/2})$ and $(5p_{1/2})$ binding energies at 22.7 and 24.8 eV. The $(5p^5 6s^2; {}^2P_{1/2})$ state was, however, not detected in the HeII spectrum because it is overlapped by the $Ba^+ 6s$/HeI line or in NeII spectrum presumably due to poor electron collection efficiency.

2. $\underline{Sm(4f^6 6s^2; {}^7F_0)}$

Both HeI and NeI spectra of Sm (Fig. 2) shows four bands centered at 5.8, 8.9, 9.6 and 11.9 eV. The band at 5.8 eV is associated with the removal of a 6s electron giving the ${}^8F$ and ${}^6F$ manifolds of the $[4f^6({}^7F)6s]$ configuration. However this band shows quite different structure in the two spectra. In the NeI spectrum it consists of two sharp peaks at 5.64 and 5.80 eV, while in HeI it is made of a sharp peak at 5.64 eV and a band with 0.34 eV FWHM at 5.80 eV. The bands at 8.9, 9.6, and 11.9 eV are similar in both spectra and have, respectively, FWHM values of 0.6, 0.4, and 1.2 eV. They are associated, in the same order, with the ${}^6H$, ${}^6F$, and ${}^6P$ terms of the Sm^+ $(4f^6 6s^2)$ configuration (see below). The HeI spectrum shows additional electron

intensity between 6.5 and 8.0 eV, and possibly also on the low energy shoulder of the ^6H manifold, although the NeI spectrum also shows an indication of weaker signals around 7 eV. The five peaks in the range 6.5 - 8.0 eV in the HeI spectrum correspond to Sm^+ states from the $4f^6(^7F)5d$ configuration, and their widths suggest more than one state within each peak. The intensity around 8.4 eV may be assigned to states from the $4f^6(^7F)6p$ configuration. The broad band centered at 10.5 eV, present only in the NeI spectrum, intensified with increasing temperature and seemed to grow relative to the other peaks with elapsed running time. It is difficult to assign the band to inelastic losses in view of its high energy, and we tentatively attribute it to impurities.

The ground state of $Sm(4f^66s^2)$ is $^7F_0$, but at ca. 1000 ^0K, the $^7F_{J=1,2,3,4,5,6}$ components are also populated. Using the energy splittings of the J components,[18b] we estimated their population ratio in the order of increasing J values to be 1.0 : 2.0 : 1.5 : 0.84 : 0.36 : 0.11 : 0.04. Since all J components of ^7F are populated, removal of a 6s electron from $[4f^6(^7F)6s^2]$ should give ^8F and ^6F terms with all the possible J values, although the lower J's are favored due to larger population of low J's in the initial state. Despite the many possible final states, it can be readily shown that both the ^8F and ^6F manifolds have energy spreads of only ca. 0.10 eV and are separated by at least 0.14 eV. This result is in good agreement with the first doublet in the NeI spectrum. Removal of a 4f-electron from the $4f^6(^7F)6s^2$ state results in ^6H, ^6F, and ^6P states and their intensity, ratios can be related to the squares of the fractional parentage coefficients,[21]

which are respectively 0.52, 0.33, and 0.14.[22] The energies of these terms for the free atoms has not yet been determined. Brewer[23] estimated the $^6H_{5/2}$ state of Sm^+ to be at (8.61 ± 0.25) eV. This value compares well with the threshold 8.6 eV of the band at 8.9 eV, and thus supports our assignment of this band to ^6H. The positions of the ^6F and ^6P states relative to ^6H can be estimated from the known intervals in the $Sm^{+3}(4f^5)$ ion. The justification for such estimation is that the 6s electrons have little screening effect on the 4f electrons. For Sm^{+3}, the weighted centers of the ^6H, ^6F, and ^6P terms are respectively 0.36, 1.11, and 3.11 eV above the $^6H_{5/2}$ state.[24] In Fig. 2a, these estimated positions are indicated by bars with lengths proportional to the squares of respective fractional parentage coefficients of the ion states. There is very good agreement between the observed and predicted energies and fair agreement in relative intensities. The J components of ^6H, ^6F, and ^6P terms for Sm^{+3} spread over respectively 0.6, 0.4 and 0.3 eV. While the widths of ^6H and ^6F terms are in perfect agreement with those observed for the bands at 8.9 and 9.6 eV, the width of ^6P is much smaller than that (1.2 eV) of the band at 11.9 eV. If spin-orbit coupling is strong enough in the $4f^5 6s^2$ configuration, then other states besides the three sextets can be accessible as a result of the mixing in the final ionic states. These additional states would fall close to the ^6p states[22] and contribute to the observed band width. In light of the above considerations, our assignment of $Sm^+(4f^5 6s^2)$ states should be reliable, and the photoelectron spectra represent the first determination of the positions of the ^6H, ^6F, and ^6P states in Sm^+.

3. Eu($4f^7 6s^2$: ^8S)

The peaks between 5.6 and 9.1 eV, except for the inelastic loss peaks at 8.34 and 8.56 eV, in both the HeIα and NeI spectra, shown in Fig. 3, are associated with the Eu^+ states of the configurations $[4f^7(^8S)6s]$, $[4f^7(^8S)5d]$, and $[4f^7(^8S)6p]$. These seven peaks correspond, as indicated in the spectrum, respectively to the states ^9S, ^7S, $^9D_{6,5,4,3,2}$, $^7D_{1,2,3,4,5}$, $^9P_{4,3}$, $^9P_5$, and $^7P_{2,3,4}$ by comparison to optical data.[18c] The electron distribution around 10.2 eV is assigned to the $^7F_{0,1,2,3,4,5,6}$ states of $Eu^+[4f^5(^7F)6s^2]$, whose positions have not been determined before. This assignment is substantiated by the close agreement between our energy for the $^7F_0$ state and that calculated by Brewer[23], i.e., (9.99 ± 0.05) and (9.76 ± 0.25) eV respectively. Furthermore, this band at 10.2 eV shows six distinct peaks with an additional one barely resolved at 9.99 eV (Fig. 3a), which is the number expected for the J values of ^7F term. In addition, the splittings among the different J components are qualitatively as expected for Eu^+ by analogy with the ^7F_J manifold of Sm.[18b] The HeIα spectrum shows two additional peaks at 11.79 and 12.42 eV, and additional intensity around 13.4 eV. The former two peaks correspond to the $^{7,9}S$ and $^{7,9}D$ states of the configurations $[4f^7(^8S)7s]$ and $[4f^7(^8S)6d]$ respectively. The weak band at 13.4 eV shows some indication of resolvable peaks. Since no optical data are available for the many states that should fall in this high-energy region, the nature of this band is not entirely certain. Even though the NeI spectrum shows no indication of peaks above 11 eV, a more definitive conclusion is precluded by the poor collection efficiency of electrons at lower kinetic energy.

There are distinct differences in the relative peak intensities found in the HeIα and NeI spectra. The intensity ratio $^{7}S/^{9}S$ is quite different; namely, it is ~2/1 in the HeI spectrum and ~1/1 in the NeI case. The ratio in NeI is quite close to the statistical ratio 7/9, while that in HeI is unexpectedly larger. Secondly, the total relative intensity of the two $^{7,9}D$ peaks is much larger in HeI and that of the $^{7,9}P$ peaks is much smaller compared to those of the NeI counterparts.

In the HeI spectrum, the $^{7,9}S$ and ^{9}D states excited by HeIβ line, and the $^{7,9}S$ states by HeIγ are positively identified. It is important to note that the $^{7}S/^{9}S$ ratio continues to deviate from the statistical ratio at the HeIβ energy (it is 1.8/1) but returns to the expected value of 7/9 at the HeIγ energy. Furthermore, the ^{9}D intensity[25] is still larger in HeIβ relative to HeIα, while that in HeIγ is much smaller (cf Table III). The ^{7}D excited by the HeIβ line is however overlapped by the intense $^{7,9}S$ at 5.8 eV.

4. Yb($4f^{14}6s^{2};{}^{1}S$)

In contrast to the cases of Ba, Sm, and Eu, the HeI and NeI spectra of Yb , shown in Fig. 4, are very similar. Both spectra show three intense peaks at 6.25, 8.91, and 10.17 eV corresponding to the Yb^{+} final states ($4f^{14}6s;{}^{2}S$), ($4f^{13}6s^{2};{}^{2}F_{7/2}$), and ($4f^{13}6s;{}^{2}F_{5/2}$) respectively. Three weak peaks at 9.27, 9.61, and 10.02 eV, which are better resolved in the NeI spectrum, are associated with the Yb^{+} states ($4f^{14}5d;{}^{2}D_{5/2}$), ($4f^{14}6p;{}^{2}P_{1/2}$), and ($4f^{14}6p;{}^{2}P_{3/2}$). In addition, there are peaks at 9.82 eV, 10.42 eV, and a number of peaks above 11.6 eV; however, the nature of these weak peaks cannot be definitely determined.

D. Discussion

1. General Consideration of Correlation Effects

In a recent paper, we[5] reported the correlation satellites in the atomic photoelectron spectra of Group-IIA and Group-IIB elements. Considering their similar valence electronic structure (s^2), we expected the lanthanides to show similar correlation effects. Accordingly, the following discussion will follow closely, except as noted, the approach adopted earlier.[5]

Because the photo ion formed by removal of a 6s-electron might be approximated by a one-electron system, the contribution of FISCI to satellite structure should be small by analogy to H and He^+, for which CI is unnecessary. The importance of the CSCI contribution is more difficult to estimate, but it will be neglected on grounds that it is generally expected to be most significant near threshold and/or for ions with closely-spaced states of the same symmetry. Therefore for the 6s ionization in Ba and the lanthanides, we shall assume that only ISCI and possibly autoionization can lead to satellites of substantial intensity.

By analogy to the Group-II elements,[5] the ground states of the lanthanides can be approximated by ISCI as

$$\psi = a|6s^2;{}^1S\rangle + b|5d^2;{}^1S\rangle + c|6p^2;{}^1S\rangle + \ldots , \qquad (1)$$

where the [Xe] core and the 4f-electrons have been suppressed, and $a \gg b \sim c$. Consequently, the photoelectron spectra of the lanthanides will show, in addition to intense peaks due to the 6s ionic states, weak lines corresponding to states such as 5d, 6p etc. The intensities of the satellites depend upon the ISCI admixture coefficients as well

as the differential photoionization cross sections. The latter normally vary smoothly with photon energy, barring the existence of Cooper minimum and resonance,[26] and over a small span of energy, say 5 - 10 eV, an order of magnitude change in cross sections is normally not expected. Consequently, if the satellites are interpreted entirely in terms of ISCI, the shapes of the spectra excited by HeI and NeI radiation should reveal little difference. This was indeed observed in Ca and Sr,[5] for which the satellite intensities hardly changed relative to the main line in both HeI and NeI spectra.

Among the cases studied here, the spectra of Yb fall within the above expectation while those of Ba, Sm, and Eu showed differences too large to be explained in terms of ISCI alone. The unexpected features all appeared at the photon energies of HeI radiation (for Ba, at more energetic NeI lines as well) and can be summarized as follows. (1) The relative intensities of the satellites are far too large to be expected from ISCI considerations. This behavior is dramatized in the HeI spectrum of Ba (Fig. 1a) which showed a number of satellites with intensities comparable to the 6s main line. This trend is further continued at several photon energies close to the HeIα (21.22 eV) line. (2) The intensity ratios of the exchange multiplets of $Sm^+(4f^6 6s;\ ^{6,8}F)$ and $Eu^+(4f^7 6s;\ ^{7,9}S)$ deviate considerably from their respective statistical multiplicity ratios. This indicates that additional mechanisms must be present at HeI energies to account for the "anomalies". In contrast, all the NeI spectra are consistent with our simple picture of ISCI, and will be interpreted as such.

2. ISCI and Satellite Structure

Let us first discuss the NeI spectra. There are two points worth noting in going from Ba, Sm, Eu to Yb. First is the variation of satellite intensities across the series. To first approximation the satellite intensities may be estimated by the squares of the CI admixture coefficients, and the magnitude of the coefficients reflects the extent of ISCI. This approximation neglects the differences in photoionization cross sections, and its limitations have been discussed elsewhere.[5,27] Experimentally, the 5d intensities appear to decrease with increasing nuclear charge, while the variation of the 6p intensities is considerably less, except for Sm. This intensity trend may be understood qualitatively by a simple consideration of CI effects. The energy of the 5d ionic state increases from Ba to Yb much faster (cf Tables I - IV) than that of the 6p state. This suggests that the energy of the $5d^2(^1S)$ configuration should also increase faster than that of the $6p^2(^1S)$. This trend in energy should be reflected roughly in the CI admixture coefficients, and thus is consistent with the variation of satellite intensities. By contrast, the decrease in satellite intensities for Sm seems to conflict with the simple energy argument. We note, however, that Sm differs from the other three atoms in having one empty 4f-orbital.

Secondly, in the cases of Sm, Eu, and Yb, depending upon the mode of ionization, the resulting ionic states may be formed with two open shells. The question then arises whether the open shell originally present will remain unchanged, or to the same effect, which of the possible final ionic states derived from the same electronic configuration can be reached upon ionization. Let us first consider the

ionization of the outermost electron from Eu. Among the many possible states of the configurations $4f^7 6s$, $4f^7 5d$, and $4f^7 6p$, only $[4f^7(^8S)6s;^{7,9}S]$, $[4f^7(^8S)5d;^{7,9}D]$, and $[4f^7(^8S)6p;^{7,9}P]$ have been positvely detected. This suggests that the above states 'used up', within experimental error, the intensity derived from the admixed configurations $4f^7 6s^2$, $4f^7 5d^2$, and $4f^7 6p^2$ in the initial state. Furthermore, considering that the $[4f^7(^8S)5d^2(^1S);^8S]$ and $[4f^7(^8S)6p^2(^1S);^8S]$ states are most likely the major components in the ISCI expansion we can then conclude that hardly any recoupling within the $4f^7$ manifold occurred upon ionization. This is not surprising since the transition to the states $[4f^7(^8S)6s;^{7,9}S]$, $[4f^7(^8S)5d;^{7,9}D]$, and $@4f^7(^8S)6p;^{7,9}P]$ can be regarded as a 'one-electron' transition respectively from the ISCI components, and hence their cross sections should be much larger than those for all other states of $4f^7 6s$, $4f^7 5d$, and $4f^7 6p$. The corresponding situation in Sm is not as clear-cut, because the satellite intensities are too low to allow for a meaningful discussion. Nevertheless, it is clear that the 4f shell remained unchanged in the $4f^6 6s$ manifold.

Next we consider the situation in which a 4f electron is ionized. Besides the $(4f)^{-1}$ primary lines, satellite states caused by ISCI may also be observed. Assuming no recoupling in the open shell, the satellites most likely to be found should be formed from the configurations $Sm^+[4f^5 5d^2(^1S)]$, $Sm^+[4f^5 6p^2(^1S)]$, $Eu^+[4f^6 5d^2(^1S)]$, $Eu^+[4f^6 6p^2(^1S)]$, $Yb^+[4f^{13} 5d^2(^1S)]$, and $Yb^+(4f^{13} 6p^2(^1S)]$, where the coupling within the $4f^n$ shell and the total state designation are identical and are dictated by the initial state and the selection rules. To our knowledge, the energies of these excited ionic states have not been determined, thus making their detection in the spectra difficult. They may, however,

account for some of the unassigned lines in the Sm, Eu, and Yb spectra. We note that this subject arose in the study of Hg by Berkowitz et al.[9] The wavefunction for the ground state of Hg can be approximated as[5,9]

$$\psi(^1S) = a|5d^{10}6s^2;^1S\rangle + b|5d^{10}6p^2;^1S\rangle + \ldots . \qquad (2)$$

Removal of 5d-electron from the second configuration results in the configuration $5d^96p^2$, which consists of two open shells. In light of the above discussion, it seems that $6p^2$ would remain coupled to ^1S and only the Hg^+ states $[5d^96p^2(^1S);^2D_{5/2}]$ and $[5p^96p^2(^1S);^2D_{3/2}]$ would contribute significantly to the electron distribution around 27.5 - 30 eV observed in the HeII spectrum (contribution from $5d^96s7s$ manifold is also possible).[9] This interpretation is consistent with the fact that the electron distribution in question appears to consist mainly of two lines at 27.8 and 29.7 eV, whose separation is close to the spin-orbit splitting 1.86 eV between $[5d^96s^2;^2D_{3/2,\ 5/2}]$. Finally, we point out that relativistic effects may cause further mixing of configurations, and especially for Sm^+ and Eu^+, this mixing may be quite important.

3. Autoionization and Satellite Structure

We now turn to the unexpected features found in the HeI spectra of Ba, Sm, and Eu. The dramatic HeI photoelectron spectrum of Ba has recently attracted a great deal of interest.[10-14] Autoionization, together with other mechanisms,[11-14] has been proposed to explain the unusual spectrum. We shall offer evidence that autoionization is the main cause of the peculiar spectrum, and furthermore, that the same mechanism is responsible for the unexpected behavior of the HeI spectra of Sm and Eu.

Heuristically, autoionization may be visualized as a two-step process. The first step involves a resonant transition to a Rydberg-type discrete state, which then decays into different continuum states, giving off free electrons with kinetic energies that label the final ionic-state energies. Autoionization arises because of the interaction between the discrete state and various continuum states. This interaction and the resulting mixing of states has been treated by Fano[3] using the CI model. In this picture, the rather large oscillator strength of the resonant transition is shared among the various coupling channels, and the probability of decaying via the individual channels is in first approximation proportional to the amount of respective mixing. Therefore, if autoionization occurs, the photoelectron spectrum will be strongly affected because each photoelectron line will derive its intensity from both direct and indirect (autoionization) ionization. The exact appearance of the resulting spectrum could be predicted only by a detailed theoretical analysis. Such an analysis is not presented here. Consequently, our discussion has to be qualitative in nature.

In general, unequivocal evidence of autoionization is frequently found in absorption spectra by observing a large absorption intensity, a broad linewidth, and an asymmetric line shape. The absorption spectrum of Ba in the energy region relevant to the photoemission work has recently been reported.[15,16] In the 19 - 25 eV region this spectrum showed a large number of strong, broad absorption lines, and indeed the lines are so densely spaced as to simulate a molecular band-type absorption. This is understandable considering that the binding energies

of the $5p_{3/2}$ and $5p_{1/2}$ electrons lie at 22.7 and 24.8 eV, and thus the Rydberg states converging to these two thresholds are expected to fill the energy interval in question quite closely. Considering the rather effective screening of the 4f-electrons, the $(5p)^{-1}$ thresholds for Sm and Eu are expected to lie not far above those of Ba. Therefore in the energy region near the HeI lines, a large number of closely-spaced Rydberg states is anticipated for Sm and Eu as well. This expectation is indeed substantiated by the absorption spectra of Sm and Eu recently recorded by Connerade et al.[28] In accordance with the foregoing energy considerations, it is quite natural that autoionization in Sm and Eu should occur at HeI energies. At the energy of NeI lines, the absorption spectra of Ba,[15,16] Sm,[28] and Eu[28] showed no absorption lines, whereas for Yb, the 5p threshold moves up high enough in energy that the absorption spectrum[28] showed no appreciable absorption around both the HeI and NeI energies. This supports our interpretation of the NeI spectra of all atoms and the HeI spectrum of Yb in terms of ISCI alone. In addition to the evidence from absorption spectra and from energy considerations, further identification of autoionization is provided by comparing the photoelectron spectra excited with photons of different energies. In general, spectra in which autoionization occurs show drastic deviations from expectations based on initial-state configuration interaction alone. By combining the above considerations, we believe that autoionization has been detected in the HeI photoelectron spectra of Ba, Sm, and Eu, as discussed below.

4. Autoionization in Ba

The remarkable contrast between the HeI and NeI spectra of Ba, together with the evidence from absorption[15,16] and previous photoemission work,[10-13] firmly establishes that autoionization processes are occurring in the HeIα spectrum. The HeIα line overlaps a 5p absorption line such that a Rydberg state is resonantly excited. This state is mixed, through CI, with a number of continuum states such as $[(Ba^{+}5p^{6}n\ell)(\varepsilon\ell')]^{o}_{J=1}$, $[(Ba^{+}5p^{5}n\ell n'\ell')(\varepsilon\ell'')]^{o}_{J=1}$, and $[(Ba^{++}5p^{6})(\varepsilon\ell')(\varepsilon\ell'')]^{o}_{J=1}$. Resonant excitation and autoionization of this state thus gives rise to the various peculiar features observed in the HeI spectrum. This process is described schematically in Fig. 5. The admixed $(Ba^{+}5p^{6}n\ell)(\varepsilon\ell')$ states autoionize directly to yield the $Ba^{+}(5p^{6}n\ell)$ lines, which are detected as peaks through the kinetic energies of the continuum electrons. $(Ba^{++}5p^{6})(\varepsilon\ell)(\varepsilon\ell')$ decays to the Ba^{++} $(5p^{6})$ state by giving off two continuum electrons, yielding a continuous electron distribution at energies above the Ba^{++} threshold (15.215 eV). The $(Ba^{+}5p^{5}n\ell n'\ell')(\varepsilon\ell'')$ manifold first autoionizes to form the highly-excited $(Ba^{+}5p^{5}n\ell n'\ell')$ states, yielding the three peaks at very low kinetic energies; i.e., at ca. 0.1 eV, detected by Hotop and Mahr.[12] These resulting Ba^{+} states can undergo further Auger transitions to the Ba^{++} $(5p^{6})$ state, with the corresponding Auger electrons detected at ca. 5.9 eV (peaks 1,2, and 3 in Fig. 1a). The energetics of this two-step autoionization-Auger process were discussed by Hansen,[14] who also suggested that the same process is responsible for double ionization

being more probable than single ionization.[10]

The HeIα spectrum of Ba consists of contributions from direct ionization as well. The respective contributions due to direct and indirect (autoionization) ionization cannot be distinguished quantitatively. We note this could be accomplished by using a tunable light source such as synchrotron radiation. Some qualitative deductions may however be reached by comparing the HeI and NeI spectra. The intensities of all lines more energetic than the Ba^{+} 6p peaks must come almost exclusively from autoionization, as must more than 95% of the 5d and 6p peak intensities. The predominant part of the intensity of even the 6s states also comes from autoionization, as suggested by its relatively small intensity at the HeIβ energy. The 6s intensity is only 0.6% (Table 1) at the HeIβ energy relative to that at the HeIα energy, as opposed to the ~5% flux of HeIβ radiation usually found in the photon source (Table 5).

The photoelectron lines (labelled S in Fig. 1a) excited by HeIβ radiation again shows two unusual features that indicate the occurrence of autoionization. First, the 5d/6s intensity ratio is ~ 3/1 which is not expected from the ISCI model. Next, the $5d_{5/2}/5d_{3/2}$ ratio is ~ 1/1.1, as opposed to the multiplicity ratio 5/3. It is worthwhile noting that the multiplicty ratios are observed rather well in the HeI spectrum (cf Table 1). As suggested by Brehm and Höfler,[11] the peaks 4 - 10 in Fig. 1a may be assigned to the higher Rydberg states converging to the Ba^{++} threshold. If this is the case, the sudden increase in the intensities of these lines seems unexpected judging from the trend of other satellite intensities. In view of our finding

that autoionization occurs at the HeIβ line energy, it is likely that part of the electron intensity between peaks 4 - 10 arises in the same way as do peaks 1 - 3, i.e., via a two-step autoionization-Auger process. Unfortunately, the corresponding autoionizing electrons were not detected due to poor analyzer transmission at low energies; otherwise the above assignment could be tested.

Autoionization also appears to occur at the various NeI line energies listed as peaks S_1, S_2, S_3 in Table 5 and Fig. 1b. This is suggested by the high photoelectron line intensities relative to the relative radiation line intensities in the usual photon flux from NeI sources, as well as the large intensity ratio of the 5d to 6s states (cf Tables 1 and 5). Furthermore, these NeI lines lie right at the seemingly continuous absorption region of the Ba absorption spectrum.[15,16] The autoionizing states involved at the NeI line energies do not seem to undergo a two-step ionization, as there is no indication for the existence of the corresponding electron lines in the spectrum (Fig. 1b)

5. Autoionization of Sm and Eu

The differences between the HeI and NeI spectra of Sm and Eu have been pointed out in Section IIIB and IIIC respectively. Following the reasoning presented above, these differences can now be understood in terms of autoionization processes. Therefore, autoionization is suggested by the spectra to occur at the HeIα line energy for Sm, and at HeIα and HeIβ energies for Eu. For all three cases, the intensity ratios measured from spectra of the multiplets of the ground ionic states deviate considerably from the expected statistical ratio (cf section IIIB and IIIC): a phenomenon also observed for the 5d doublets of Ba^+

excited by the HeIβ line. Intuitively, this large deviation is quite unexpected, considering the similarity of the states involved, but somehow it appears to reflect the subtlety of the interaction in the final states.

E. Conclusions

Satellite lines have been observed in both HeI and NeI photoelectron spectra of Ba, Sm, Eu, and Yb. The lines have been interpreted in terms of initial-state configuration interaction and autoionization in the final state. By using the different rare gas resonance lines, it was possible to selectively excite certain autoionizing levels, and subsequently identify the satellite structure due to autoionization. Photoelectron spectra showing autoionization were found to contain a great deal of information about the nature and extent of the interaction between the discrete level and the individual continuum channels. The sensitivity of photoelectron spectra toward this coupling is far superior to that of natural line widths, absorption line profiles, etc. revealed in absorption spectra, because the photoelectron channel adds a new dimension of information. Therefore it is anticipated that photoelectron spectroscopy, carried out with a continuously tunable photon source such as synchrotron radiation, will become a powerful method of studying electron correlation in both initial and final states.

ACKNOWLEDGEMENTS

We are indebted to Miss Geri Richmond for experimental assistance, to Dr. J. P. Connerade for sending us the absorption spectra of metal vapors prior to publication, and to Mr. R. S. Williams for help with the relativistic Hartree-Fock calculation.

REFERENCES AND FOOTNOTES

1. R. L. Martin and D. A. Shirley, J. Chem. Phys. 64, 3685 (1976).

2. S. T. Manson, J. Elect. Spect. 9, 21 (1976).

3. U. Fano, Phys. Rev. 124, 1866 (1961).

4. R. L. Martin and D. A. Shirley, Phys. Rev. 13, 1475 (1976).

5. S. Süzer, S.-T. Lee, and D. A. Shirley, Phys. Rev. 13, 1842 (1976).

6. S. Süzer, M. S. Banna, and D. A. Shirley, J. Chem. Phys. 63, 3473 (1975).

7. S. Süzer, S.-T. Lee, and D. A. Shirley, J. Chem. Phys. 65, 412 (1976).

8. S. Süzer and D. A. Shirley, J. Chem. Phys. 61, 2481 (1974).

9. J. Berkowitz, J. L. Dehmer, Y. K. Kim, and J. P. Desclaux, J. Chem. Phys. 61, 2556 (1974).

10. B. Brehm and A. Bucher, Int. J. Mass Spectrom. Ion Phys. 15, 463 (1974).

11. B. Brehm and K. Höfler, Int. J. Mass Spectrom. Ion Phys. 17, 371 (1975).

12. H. Hotop and D. Mahr, J. Phys. B8, L301 (1975).

13. U. Fano, Comments On At. and Mol. Phys. 4, 119 (1973).

14. J. E. Hansen, J. Phys. B8, L403 (1975).

15. J. P. Connerade, M.W.D. Mansfield, K. Thimm, and D. Tracy, VUV Radiation Physics, ed. by E. E. Koch, R. Haensel, and C. Kunz (Pergamon, Vieweg, 1974), p. 243.

16. D. L. Ederer, T. B. Lucatorto, and E. B. Salomon, VUV Radiation Physics, ed. by E. E. Koch, R. Haensel, and C. Kunz (Pergamon, Vieweg, 1974), p. 245.

17. R. G. Newburgh, L. Heroux, and H. E. Hinteregger, App. Optics 1, 733 (1962).

18. (a) Ba —C. E. Moore, Natl. Bur. Stand. (U.S.A.) Circ. 467, Vol. 3 (1962); (b) Sm — J. Blaise, C. Morillon, M-G Schweighofer, and J. Verges, Spect. Acta 24B, 405 (1962); W. Albertson, Astrophys. J. 84, 26 (1936). (c) Eu — A. C. Parr, J. Chem. Phys. 54, 3161 (1971); H. N. Russell, W. Albertson, and D. N. Davis, Phys. Rev. 60, 641 (1941). (d) Yb — V. Kaufman and J. Sugar, J. Opt. Soc. Amer. 63, 1168 (1973); W. F. Meggers, J. Res. NBS, 71A, 396 (1967); A. C. Parr and F. A. Elder, J. Chem. Phys. 49, 2665 (1968).

19. J. P. Desclaux, Comp. Phys. Comm. 9, 31 (1975).

20. D. A. Shirley, R. L. Martin, B. E. Mills, S. Süzer, S.-T. Lee, E. Matthias, and R. A. Rosenberg, Proc. 2nd Int. Conf. on Inner Shell Ionization Phenomena, Freiberg, Germany, March 29 - April 2, 1976; S.-T. Lee, R. A. Rosenberg, E. Matthias, and D. A.Shirley, to be published.

21. P. A. Cox and F. A. Orchard, Chem. Phys. Lett. 7, 273 (1970); P. A. Cox, S. Evans, and F. A. Orchard, ibid, 13, 386 (1972).

22. C. W. Nielson and G. F. Koster, Spectroscopic Coefficients for the p^n, d^n, and f^n Configurations, The M.I.T. Press (1963).

23. Leo Brewer, J. Opt. Soc. Amer. 61, 1666 (1971).

24. W. T. Carnall, P. R. Fields, and K. Rajnak, J. Chem. Phys. 49, 4424 (1968).

25. The ionization of He by HeII (40.8 eV) line falls close to the ^9D signal, but its contribution to the intensity is estimated to be less than a few per cent.

26. J. W. Cooper, Phys. Rev. Lett. 13, 762 (1964); U. Fano and J. W. Cooper, Rev. Mod. Phys. 40, 441 (1968).

27. J. E. Hansen, private communication and to be published.

28. J. P. Connerade, private communication.

TABLE I. Observed states of Ba^+ and relative peak intensities in HeI and NeI spectra.

Ba^+ state[a]		Binding[b] energy (eV)	Optical[c] value (eV)	Intensity[d] HeI	Intensity[e] NeI
6s	$^2S_{1/2}$	5.211	5.211	100; 0.6	100; 1.6; 5.4; 0.8
5d	$^2D_{3/2}$	5.81	5.816	72; 0.9	22; 2.2;
	$^2D_{5/2}$	5.91	5.915	160; 0.8	5.0; ——
6p	$^2P_{1/2}$	7.72	7.723	36	1.5
	$^2P_{3/2}$	7.93	7.933	63	3.2
7s	$^2S_{1/2}$	10.46	10.463	38	0.7
6d	$^2D_{5/2,3/2}$	10.92	10.908; 10.934	108	0.7
4f	$^2F_{7/2,5/2}$	11.20	11.195; 11.222	19	0.5
7p	$^2P_{1/2}$	11.33	11.335	15	
	$^2P_{3/2}$	11.40	11.412	33	
5f	$^2F_{5/2,3/2}$	12.34	12.327; 12.357	28	

TABLE I. (con't)

Ba^+ state[a]		Binding[b] energy (eV)	Optical[c] value (eV)	Intensity[d] HeI	Intensity[e] NeI
8s	$^2S_{1/2}$	12.40	12.405	47	
7d	$^2D_{5/2,3/2}$	12.63	12.626; 12.637	37	
8p	$^2P_{3/2,1/2}$	12.84	12.816; 12.853	20	
5g	$^2G_{9/2,7/2}$	13.02	13.026	11	
6f	$^2F_{7/2,5/2}$	13.22	12.220; 12.233	10	
9s	$^2S_{1/2}$	13.35	13.355	5	
8d	$^2D_{5/2,3/2}$	13 48	13.478; 13.484	7	
9p	$^2P_{3/2,1/2}$	13.61	(13.583; 13.603)	12	
6g	$^2G_{9/2,7/2}$	13.69	13.695	13	
7f	$^2F_{7/2,5/2}$	13.79	13.792; 13.798	3	

TABLE I. (con't)

Ba^+ state[a]		Binding[b] energy (eV)	Optical[c] value (eV)	Intensity[d] HeI	Intensity[e] NeI
10s	$^2S_{1/2}$	13.89	13.892	2	
9d	$^2D_{5/2,3/2}$	13.96	13.967; 13.971	2	
10p	$^2P_{3/2,1/2}$	14.04	(14.031; 14.045)	4	
7g	$^2G_{9/2,7/2}$	14.10	14.099	5	
(11s)	10	14.22	(14.226)	65	
(11p)	9	14.32	(14.317,14.325)	40	
(12s)	8	14.45	(14.447)	28	
	7	14.56		13	
	6	14.66		2	
	5	14.77		3	

TABLE I. (con't)

Ba^+ state[a]	Binding[b] energy (eV)	Optical[c] value (ev)	Intensity[d] HeI	Intensity[e] NeI
4	15.12		44	
3	15.28	15.283	291	
2	15.37	15.366	221	
1	15.42	15.420	81	

a. The [Xe] core has been suppressed in this notation. Peaks 1 - 3 are Auger transitions. For other numbered states, the assignment is not final; see text.

b. The error limit is less than 10 meV.

c. Optical binding energies were obtained from ref. 18a. The values in parenthesis are binding energies estimated from the Rydberg formula, and those for states 1 - 3 are from ref. 12.

d. Intensities are corrected for $\Delta E/E$ dependence and referenced to the Ba^+6s/HeI_α line. Where there are two entries, the first is from the HeI_α and the second from the HeI_β spectrum.

e. Intensities are corrected for $\Delta E/E$ dependence and referenced to Ba^+6s/NeI line. Where there is more than one entry, the first value is from NeI main line, and the others are from NeI S_3, S_2, and S_1 satellite lines.

TABLE II. Observed states of Sm^+ and relative peak intensities in HeI and NeI spectra.

Sm^+ state[a]	Binding[b] energy (eV)	Optical value (eV)	Intensity[e] HeI	Intensity[e] NeI
$4f^6 6s$ ^8F	5.64(2)	5.63[c]	27	100
^6F	5.80(2)	5.82[c]	100	100
$4f^6 5d$	6.61(2)	6.52-8.19[c]	7	4
	6.94(2)		18	4
	7.39(2)		8	——
	7.70(2)		8	——
	7.90(2)		13	——
$4f^6 6p$	8.4 (1)	>8.27[c]	20	<10
$4f^5 6s^2$ ^6H	8.8 (1)	9.0 [d]	76	140
^6F	9.6 (1)	9.7 [d]	35	77
^6P	11.9 (1)	11.7 [d]	39	64

a. The [Xe] core has been suppressed. The particular states of the $(4f^6 5d)$ and $(4f^6 6p)$ configurations cannot be identified, nor are the J values for all the states.

b. The error is listed in parenthesis. The binding energies for broad bands are the vertical values.

c. From ref. 18b. The values for ^6F and ^8F correspond to the transitions $Sm(^7F_o) \rightarrow Sm^+(^8F_{1/2})$ and $Sm^+(^6F_{1/2})$ respectively.

d. The values were estimated from refs. 23 and 24 (cf. text), and are the weighted centers of the individual terms. Ref. 23 gave $^6H_{5/2}$ at (8.61 ± 0.25) eV.

e. The intensities are corrected for the $\Delta E/E$ dependence of this type of spectrometer.

TABLE III. Observed states of Eu^+ and relative peak intensities in HeI and NeI spectra.

Eu^+ state[a]		Binding energy[b] (eV)	Optical value[c] (eV)	Intensity HeI[d]	Intensity NeI[d]
$4f^7 6s$	$^9S_4$	5.67	5.670	52; 4.5; 1.9	95
	$^7S_3$	5.88	5.877	100; 8.1; 1.5	100
$4f^7 5d$	$^9D_{2,3,4,5,6}$	6.96	6.900 - 7.049	26; 9.8; 0.7	12
	$^7D_{1,2,3,4,5}$	7.77	7.760 - 7.817	32	10
$4f^7 6p$	$^9P_{3,4}$	8.67(5)	8.617; 8.670	3	7
	$^9P_5$	8.92	8.914	0.6	2
	$^9P_{4,3,2}$	9.04	8.997; 9.029; 9.048	2	4
$4f^6 6s^2$	$^7F_0$	9.99(3)	———		
	$^7F_1$	10.07	———		
	$^7F_2$	10.15	———		
	$^7F_3$	10.25	———	114	226
	$^7F_4$	10.37	———		
	$^7F_5$	10.46	———		
	$^7F_6$	10.55	———		

TABLE III. (con't)

Eu^+ state[a]	Binding[b] energy (eV)	Optical[c] value (eV)	Intensity[d] HeI	Intensity[d] NeI
$4f^7 7s$ $^9S_4$; $^7S_3$	11.79(3)	11.761; 11.825	2	——
$4f^7 6d$ ^9D ; ^7D	12.42	12.399 - 12.438	1	——

a. The [Xe] core has been suppressed.

b. The error limit is 20 meV except as listed in parenthesis. The binding energies for broad bands are the vertical ones.

c. From ref. 18C.

d. The intensities are corrected for the $\Delta E/E$ dependence and referenced to the $^7S_3$ line. Where there are three entries in the HeI column, they are from HeIα, HeIβ, and HeIγ spectra respectively.

TABLE IV. Observed states of Yb^+ and relative peak intensities in HeI and NeI spectra

Yb^+ state[a]	Binding[b] energy (eV)	Optical[c] value (eV)	Intensity[d] HeI	Intensity[d] NeI
$4f^{14}6s \quad {}^2S_{1/2}$	6.25	6.254	100	100
$4f^{14}5d \quad {}^2D_{5/2}$	9.2	9.271	6	10
$4f^{13}6s^2 \quad {}^2F_{1/2}$	8.91	8.910	180	281
$\quad\quad\quad\quad {}^2F_{5/2}$	10.17	10.168	95	135
$4f^{14}6p \quad {}^2P_{1/2}$	9.61	9.609	3	3
$\quad\quad\quad\quad {}^2P_{3/2}$	10.02	10.022	5	5
———	9.82		2	6
———	11.77		7	2
———	12.37		8	9
———	13.53		11	12
———	14.68		4	———

a. The [Xe] core has been suppressed. Some states have not been identified.

b. The error limit is 20 meV.

c. The binding energies are from ref. 18d.

d. The intensities are corrected for $\Delta E/E$ dependence and referenced to the Yb^+6s line.

TABLE V. The energies and relative line intensities of the HeI and NeI resonance radiation spectra

Source	Excited state	Designation	Wavelength (Å)[a]	Energy (eV)	Relative intensity[b]
Helium capillary discharge	2^1P_1	HeIα	584.334	21.2175	100
	3^1P_1	HeIβ	537.030	23.0864	4.5(1.0)
	4^1P_1	HeIγ	522.213	23.7415	0.6(0.2)
Neon capillary discharge	$3s[3/2]^\circ_1$	NeI	743.718	16.6704	27(5)
	$3s'[1/2]^\circ_1$	doublet	735.895	16.8476	100
	$4s[3/2]^\circ_1$	S_3	629.74	19.688	0.5(0.2)
	$4s'[1/2]^\circ_1$		626.82	19.779	
	$3d[1/2]^\circ_1$	S_2	619.10	20.026	0.2(0.1)
	$3d[3/2]^\circ_1$		618.67	20.040	
	$3d'[3/2]^\circ_1$		615.63	20.139	

TABLE V. (con't)

Source	Excited state	Designation	Wavelength (Å)[a]	Energy (eV)	Relative intensity[b]
	$5s[3/2]_1^\circ$		602.73	20.570	
	$5s'[1/2]_1^\circ$		600.01	20.663	
	$4d[1/2]_1^\circ$	S_1	598.88	20.702	0.1(0.1)
	$4d[3/2]_1^\circ$		598.68	20.709	
	$4d'[3/2]_1^\circ$		595.92	20.805	
	$6s[3/2]_1^\circ$		591.82	20.949	
	$6s'[3/2]_1^\circ$		589.18	21.043	
	$5d[1/2]_1^\circ$	S_0	590.02	21.013	0.03(0.03)
	$5d[3/2]_1^\circ$		589.91	21.017	
	$5d'[3/2]_1^\circ$		587.23	21.113	

a. Reference 18a.

b. The relative intensity was determined by the Xe ^2P doublet. The values in parenthesis are the probable errors, predominantly due to intensity fluctuations in the source.

FIGURE CAPTIONS

Fig. 1 Photoelectron spectra of Ba^+. (a) Excited by HeI lines. The peaks marked S are due to ionization by the HeIβ line. (b) Excited by NeI lines. The peaks marked S_1, S_2, and S_3 are due to ionization by the more energetic NeI satellite lines, and those starred are believed to be Auger peaks arising from excitation by the plasma electrons from the lamp and/or NeII radiation. In both spectra, the peaks marked I arise from elastically scattered electrons.

Fig. 2 Photoelectron spectra of Sm^+. (a) Excited by HeI line. The vertical bars are the estimated positions and intensities of the ^6H, ^6F, and ^6P terms of the ($4f^5 6s^2$) configuration (see text). (b) Excited by NeI line. The nature of the band at 10.5 eV is not known.

Fig. 3. Photoelectron spectra of Eu^+. (a) Excited by HeI lines. The lines marked S_β and S_γ are due to ionization by HeIβ and HeIϒ lines. (b) Excited by NeI line. In both spectra, the lines marked I are elastically scattered electrons.

Fig. 4. Photoelectron spectra of Yb^+. (a) Excited by HeI lines. The lines marked S are due to ionization by HeIβ line. (b) Excited by NeI line. In both spectra, the lines marked I are elastically scattered electrons.

FIGURE CAPTIONS

Fig. 5. Energy diagram illustrating the autoionization process of Ba at HeIα energy. The 5p thresholds are from this work and the energy of ($5p^6 6s5d$) is from ref. 12. All other energy levels are from ref. 18a.

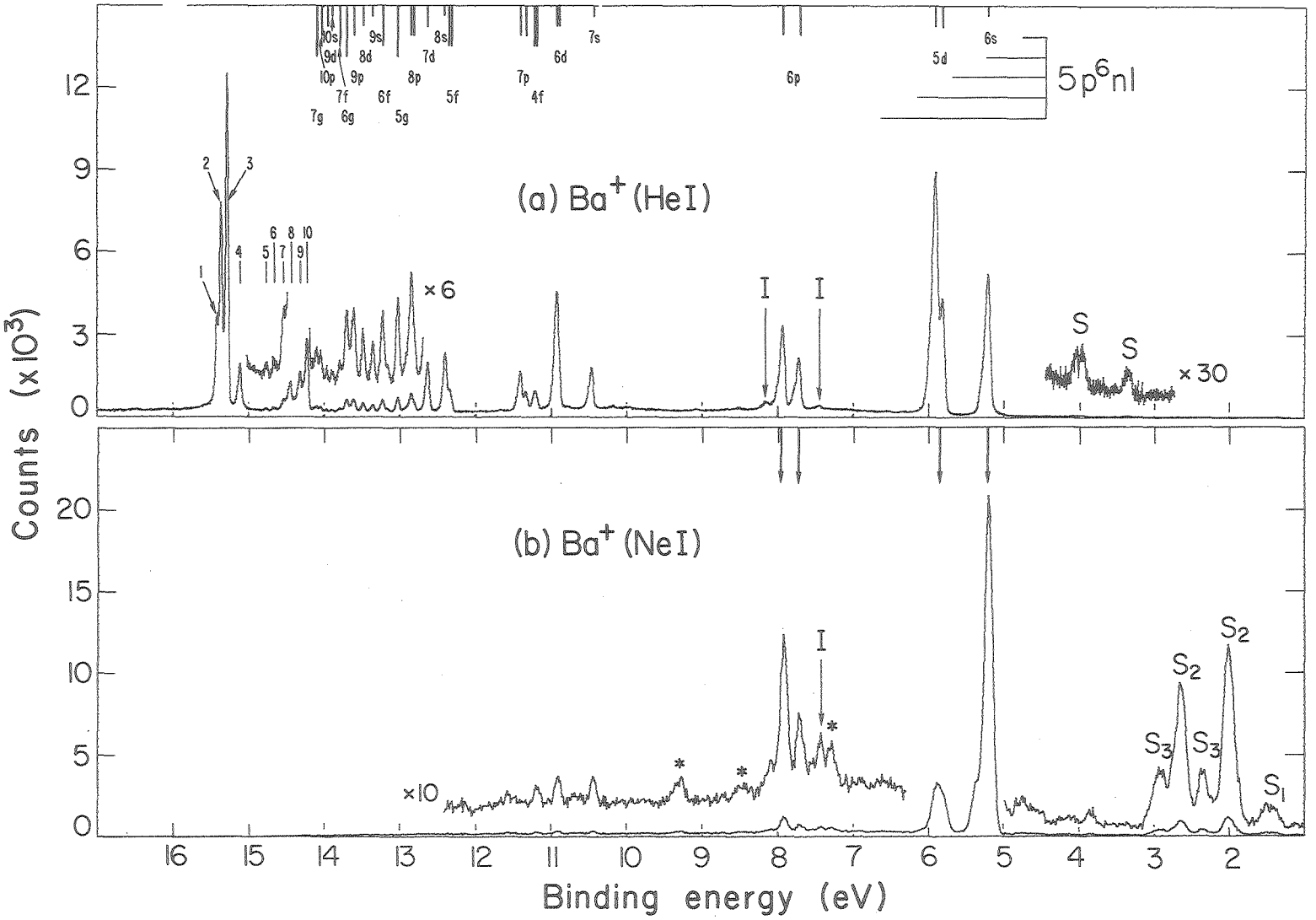

XBL 763-2444A

Fig. 1

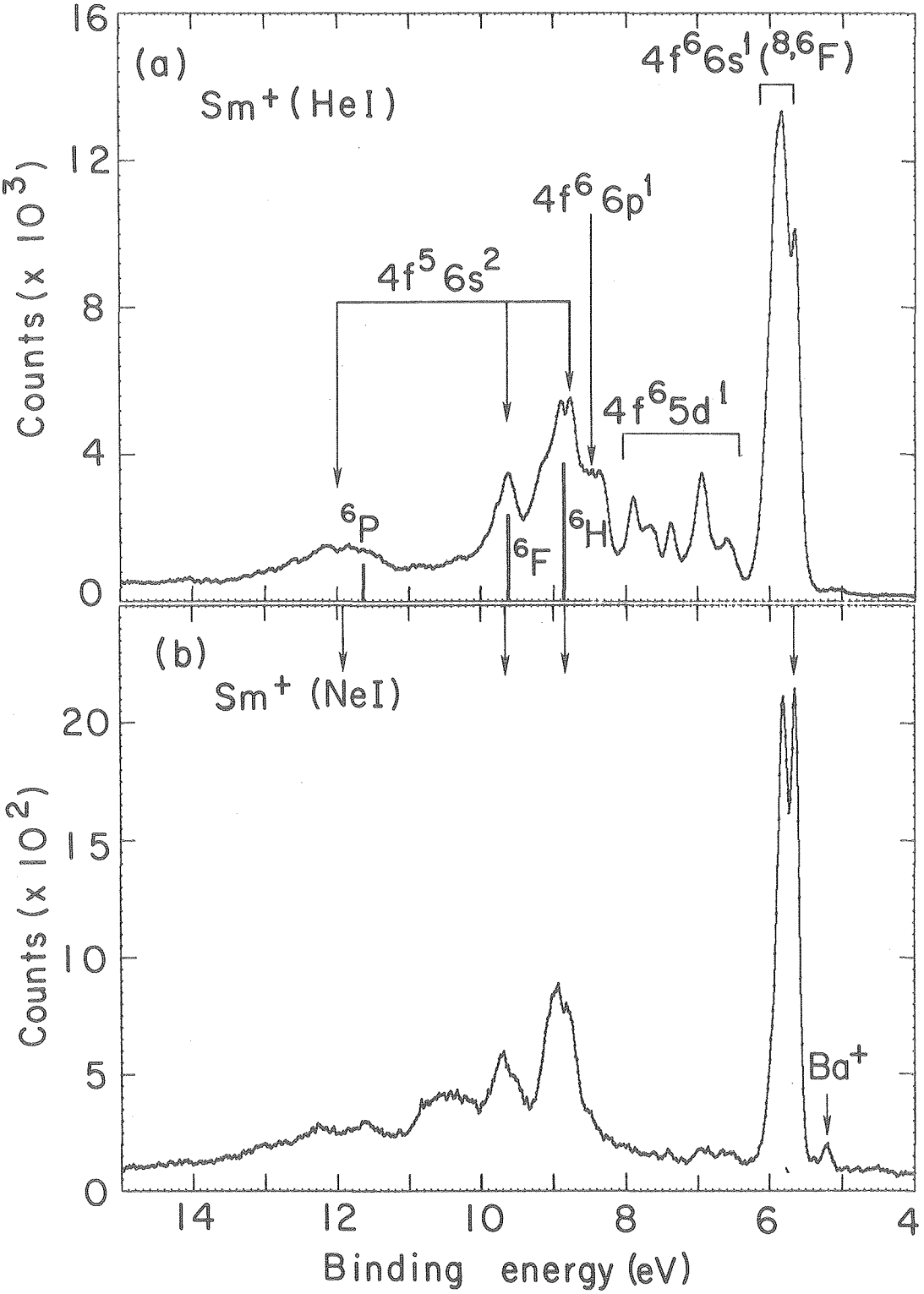

XBL 767-3238 A

Fig. 2

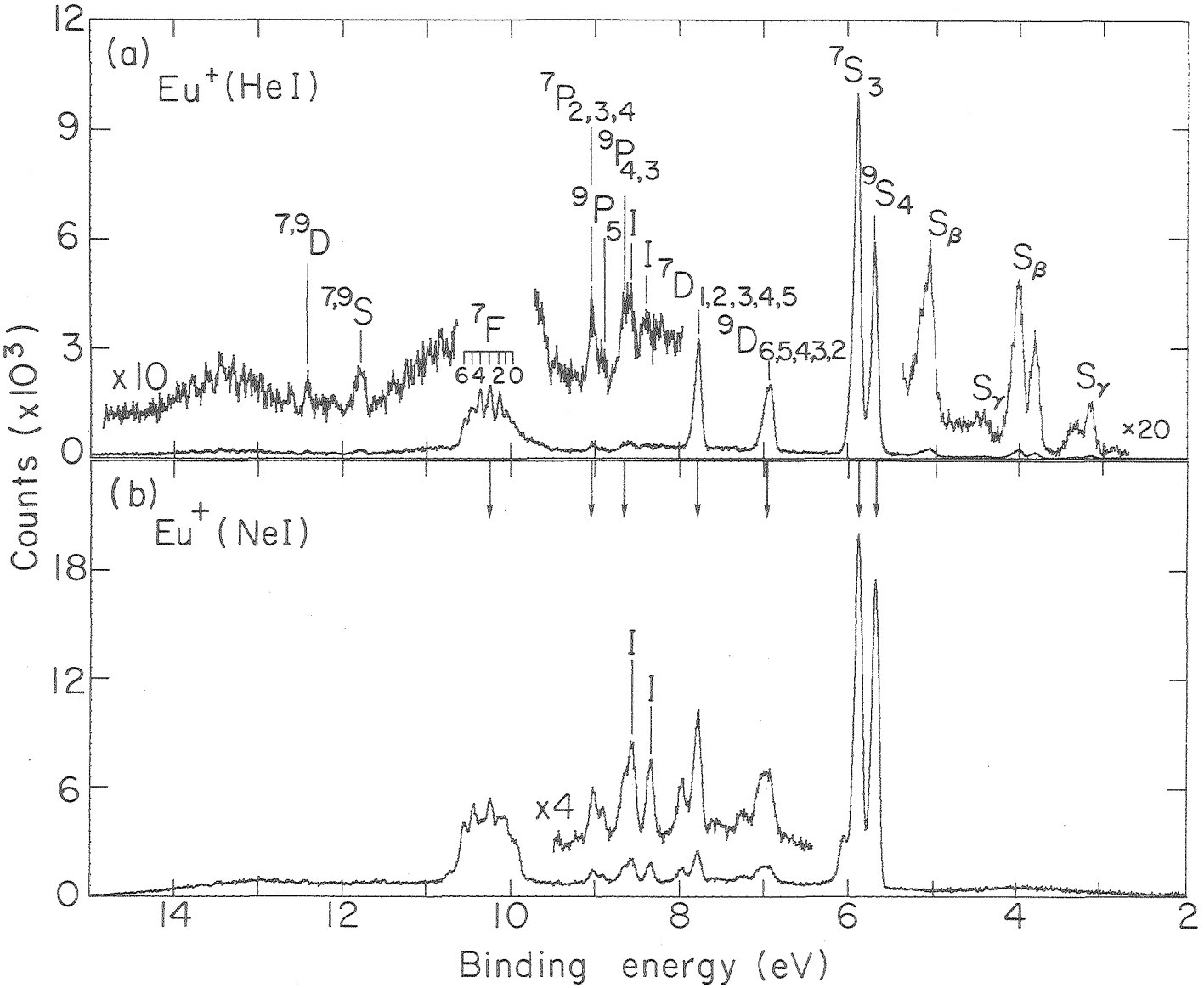

XBL 7512-9596 A

Fig. 3

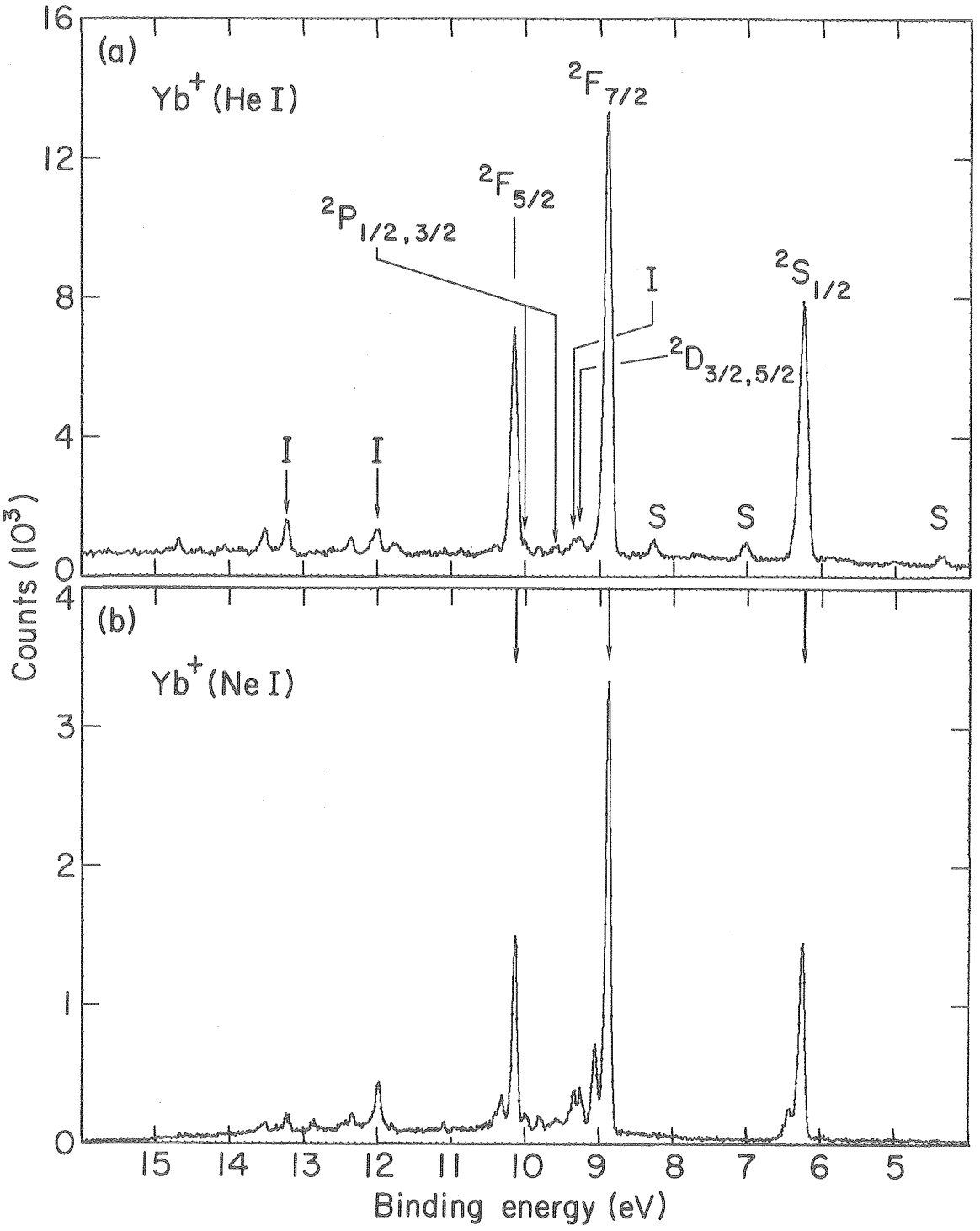
(a)
Yb+ (He I)
2F7/2
2F5/2
2P1/2,3/2
I
2S1/2
2D3/2,5/2
I
I
S
S
S
(b)
Yb+ (Ne I)
Counts (10³)
Binding energy (eV)
XBL761-2030 A

Fig. 4

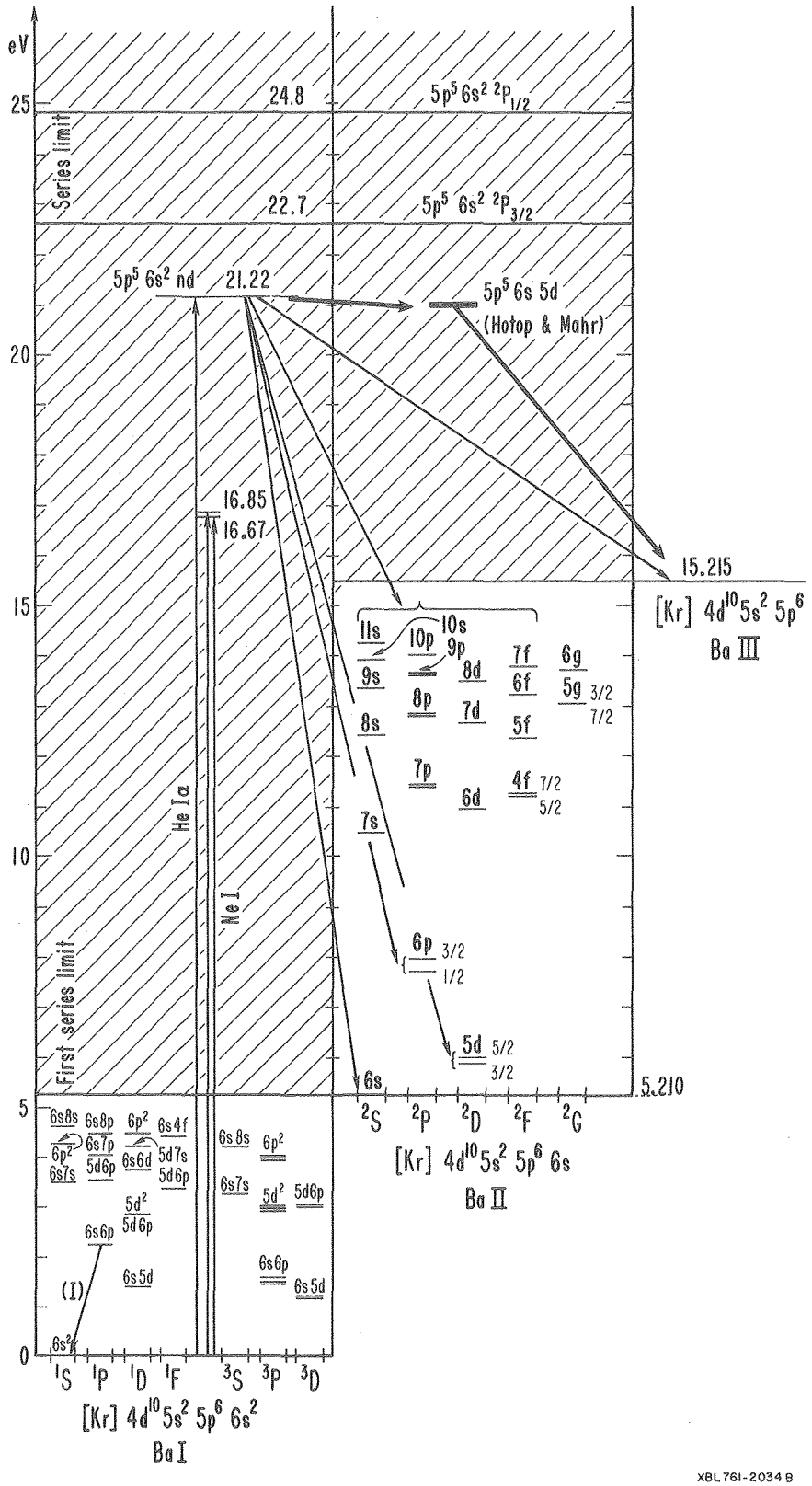

XBL 761-2034 B

Fig. 5

IV. LIFETIME OF THE XeII $5s5p^6\ ^2S_{1/2}$ STATE*

ABSTRACT

Synchrotron radiation affords the possibility of lifetime measurements of excited ionic states following their selective excitation. We have used this method to determine the lifetime of the XeII $5s5p^6\ ^2S_{1/2}$ state as 34.4(6) nsec. Multi-configuration Hartree-Fock calculations yield a value of 9.5 nsec, indicating the importance of relativistic effects in such a system.

---

*Paper published with co-authors M. G. White, E. D. Poliakoff, G. Thornton, and D. A. Shirley, J. Phys. B. 11, L719 (1978).

Electron-electron correlations in atoms and molecules lie at the frontier of our understanding of the properties of matter. Correlation effects are not only difficult to calculate, requiring computational methods beyond the Hartree-Fock level, but they are also hard to measure, because most spectroscopic parameters are only indirectly sensitive to electron correlation. Electron spectroscopy, on the other hand, provides rather direct insight into correlation effects, because removal of an electron from an N-electron system yields "correlation satellites" in the (N-1) electron system. Of special interest are states of nominal configuration $nsnp^6$ formed by removal of a valence s electron from a closed-shell atom. Excitation of a pair of electrons to configuration of the form $ns^2np^4n'\ell$ costs little in energy: thus a large degree of configuration mixing is expected.

Fluorescence de-excitation of the ionic "$nsnp^6$" state to the ionic ground state, following photoionization, provides further insight into the structure of the nominal $nsnp^6$ state because its lifetime is sensitive to its composition. With the availability of pulsed vacuum ultraviolet synchrotron radiation at the Stanford Synchrotron Radiation Laboratory (SSRL), and the development of a new apparatus that allows spectroscopic studies of gaseous samples above the LiF cutoff, we have undertaken a lifetime measurement of such a state in Xenon.

The XeII $5s5p^6\ ^2S_{1/2}$ state is a particulary desirable candidate for study because it has been the subject of a great deal of recent experimental and theoretical effort and its lifetime has not been previously determined experimentally. Many-body and relativistic effect have

been found to play a significant role in this state, as manifested in photoelectron spectroscopy by satellite structure[1-3] and asymmetry parameter (β) variations.[4] In order to describe these phenomena adequately, it has been necessary to include both electron correlation and relativistic effects.[5-7] To date, however, only configuration interaction has been incorporated in the calculation of the fluorescent lifetime. The results given below show the need to include relativistic effects in any model used to describe such a system.

The experiments were carried out on the "8° line at SSRL. The timing characteristics and most of the apparatus have been described previously.[8] However, in order to extend the usable energy range above the LiF cutoff (11.8 eV), a thin (1500 Å) Al window (Luxel Corp.) was incorporated into the apparatus. This made available radiation in the region 17 eV < $h\nu$ < 35 eV. The Xe sample (99.995%) was introduced through a leak valve to give a nominal chamber pressure of 5 microns. Outgassing from the walls caused the pressure to rise slightly during the experiment. Single photon counting was carried out with an EMR-510G photomultiplier, mounted perpendicular to the synchrotron beam, by the use of standard pulse-counting techniques. The bandpass of the excitation monochromator was set at 2 Å.

The $5s5p^6\ {}^2S_{1/2}$ state is the lowest excited state of XeII[9]; therefore, the only possible fluorescence populates the spin-orbit split ground state of $5s^25p^5$, $^2P_{3/2}$ (1100 Å) and $^2P_{1/2}$ (1244 Å). The threshold for the $5s5p^6\ {}^2S_{1/2}$ falls at 529.6 Å.[9] At longer wavelengths only a small signal, attributable to residual gases was observed, while

at threshold a sharp increase in signal was seen which appeared to decrease slowly at lower wavelengths, in agreement with the photoionization cross section for this state.[10]

A typical decay curve, taken at 526 Å, is shown in Figure 1. A least squares fit of the data yields a lifetime of 34.4(6) nsec. The analogous level in KrII ($4s4p^6$) was determined by Irwin et al,[11] using beam-foil excitation, to have a lifetime of 0.33(4) nsec, while the $3s3p^6$ state in ArII was measured by Lawrence[12] with electron impact excitation to have a lifetime of 4.8(1) nsec.

Multi-configuration Hartree-Fock calculations by Hansen[13] yield a lifetime for the XeII $5s5p^6(^2S_{1/2})$ level of 9.5 nsec. The apparent discrepancy with the experimental value of 34.4 nsec is a result of the non-relativistic treatment of the ionic state wavefunctions. In this calculation the ^2S excited state wavefunction was approximated by the mixing of the $5s5p^6(^2S)$ (61%) and $5s^25p^4(^1D)5d(^2S)$(39%) states. This treatment ignores the admixtures of other configurations of even parity and the same J (=1/2) which would result by the inclusion of relativistic effects. Recently, XeII energy level calculations by El Sherbini and Zaki[14] show an additional 4% mixing of the $5s^25p^45d(^4P)$ state, and the photoemission work of Adam et al,[2] Süzer and Hush,[1] and Gelius[3] show several weak satellite lines associated with the $(5s)^{-1}$ hole state attributable to the $5s^25p^4ns(^2P, ^4P)$ and the $5s^25p^4nd(^2P, ^4P, ^4D)$ configurations. These terms can only be correlated to the ^2S hole state through spin-orbiting coupling. In addition, the contributions to the transition moment from the two configurations used by Hansen largely cancelled

each other. Hence, the small admixtures of other states could lead to a substantial change in the calculated lifetime.

Motivated by the results reported here, Hansen[15] has recently recalculated the XeII $5s5p^6\ ^2S_{1/2}$ state and included relativistic effects. Using three different methods of calculation, he reports values of 34.1 ns, 32.7 ns, and 37.1 ns, in excellent agreement with the experimental value.

Hansen's results[13] for the analogous states in KrII and ArII are 6.6 nsec and 5.0 nsec respectively. These are set out, with the experimental values, in Table I. The agreement with the experimental result for ArII is quite good, indicating that relativistic effects are less important in this case, as expected. For KrII, the experiment has recently been repeated using beam foil spectroscopy and although the results are not yet conclusive, they do cast some doubt on the earlier measurements (Kernahan 1978).

In summary, we have made the first measurement of the lifetime of the XeII $(5s5p^6)\ ^2S_{1/2}$ state and found it to be 34.4(6) nsec. The difference between this and Hansen's MCHF result indicated the need for a more sophisticated, multi-configuration, Dirac-Fock calculation. Inclusion of relativistic effects are justified by the success of Hansen's most recent calculation.[15] In the future we hope to utilize synchrotron radiation to unambiguously determine the lifetimes of the analogous states in Kr and Ar.

REFERENCES

1. S. Süzer and N. S. Hush, J. Phys. B 10, L 705 (1977).

2. M. Y. Adam, F. Wuilleumier, N. Sandner, V. Schmidt, and G. Wendin, Journal de Physique, 39, 129 (1978).

3. U. Gelius, J. Elect. Spec. and Rel. Phen., 5, 985 (1974).

4. J. L. Dehmer and Dan Dill, Phys. Rev. Lett., 37, 1049 (1976).

5. W. R. Johnson and K. T. Cheng, Phys. Rev. Lett., 40, 1167 (1978).

6. W. Ong and S. T. Manson, J. Phys. B11, L65 (1978).

7. G. Wendin, Physica Scripta, 16, 296 (1977).

8. E. Matthias, R. A. Rosenberg, E. D. Polakoff, M. G. White, S.-T. Lee and D. A. Shirley, Chem. Phys. Lett., 52, 239 (1977).

9. C. E. Moore, Atomic Energy Levels, NBS Circular PO-467 (Washington; U.S. Government Printing Office), p. 118 (1958).

10. T. Gustaffson, Chem. Phys. Lett., 51, 383 (1977).

11. D. J. G. Irwin, K. A. Kernahan, E. H. Pinnington, and A. E. Livingston, J. Opt. Soc. Am., 12, 1396 (1976).

12. G. M. Lawrence, Phys. Rev., 179, 154 (1969).

13. J. E. Hansen, J. Opt. Soc. Am., 67, 754 (1977).

14. Th. M. El Sherbini and M. A. Zaki, J. Phys. B. 11, 2061 (1978).

15. J. E. Hansen, private communication (1979).

TABLE I. Calculated and experimental lifetimes for the ns np^6 state in ArII (n-3), KrII (n-4), and XeII (n-5).

Ion	Calculated[a]	Measured	Method
ArII	5.0	4.8(1)[b]	Pulsed electron impact
KrII	6.6	0.33(4)[c]	Beam-foil excitation
XeII	9.5	34.4(6)[d]	Pulsed-photon impact
	(34.1,32.7,37.1)[e]		

[a] Ref. 13

[b] Ref. 12

[c] Ref. 11

[d] Present work

[e] Ref. 15

FIGURE CAPTION

Fig. 1. Fluorescence decay curve of XeII $5s5p^6\ {}^2S_{1/2}$ fitted with a single exponential.

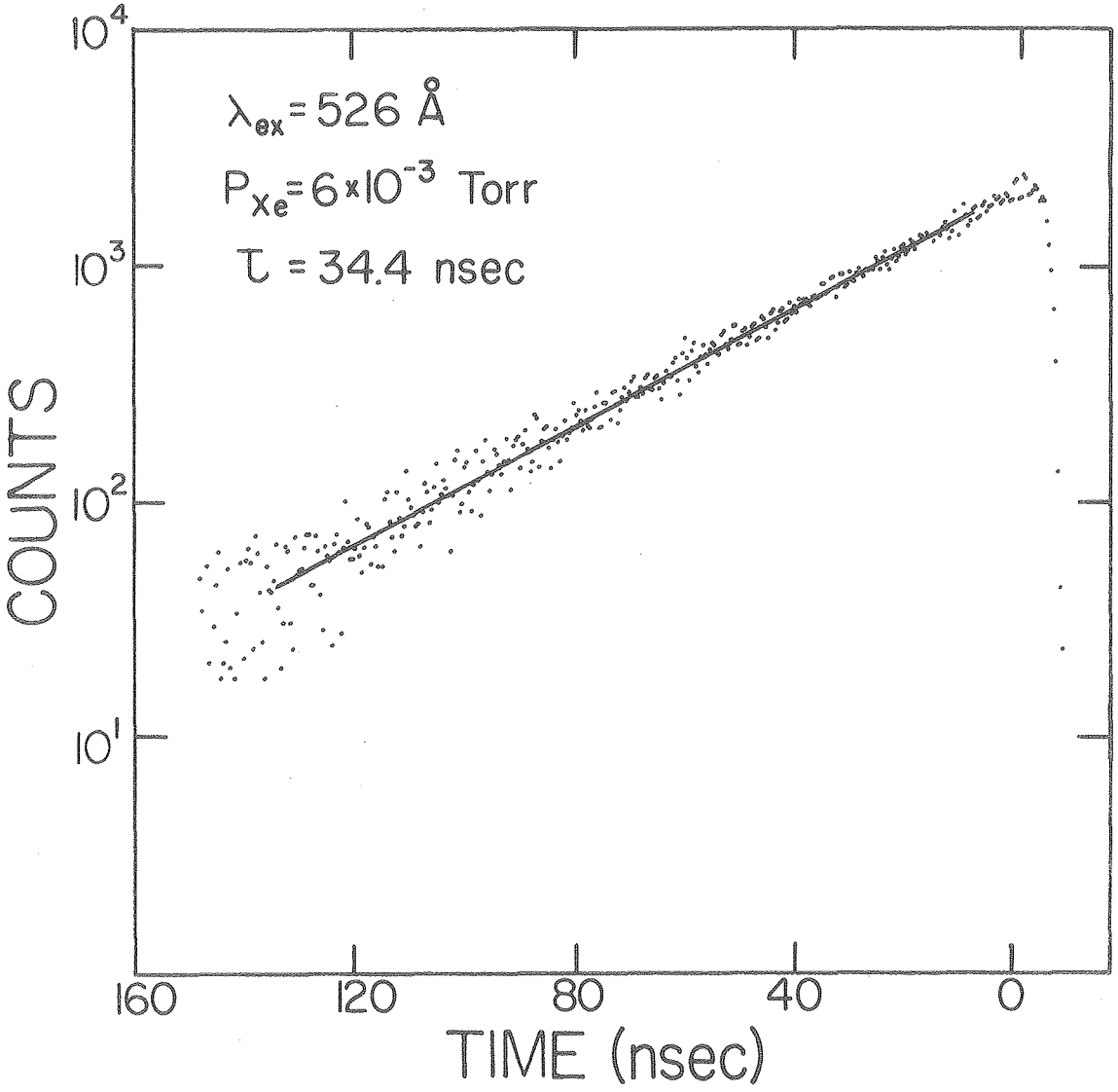
10^4
10^3
10^2
10^1
COUNTS
λ_{ex} = 526 Å
P_{Xe} = 6 x 10^{-3} Torr
τ = 34.4 nsec
160
120
80
40
0
TIME (nsec)
XBL 784-7948

Fig. 1

V. RESONANCE ENHANCEMENT OF ELECTRON CORRELATION SATELLITES: THE PHOTOELECTRON SPECTRA OF ATOMIC Ba AT SELECTED AUTOIONIZING RESONANCES*

ABSTRACT

The photoelectron spectra of atomic Ba at two autoionizing resonances has been recorded using synchrotron radiation. There is experimental evidence to suggest that Auger-type decay is the dominant channel for interaction of the autoionizing level with the continuum.

---

*Work done in collaboration with M. G. White, G. Thornton, and D. A. Shirley.

The interaction of autoionizing levels with continuum states has been the subject of a great deal of experimental and theoretical effort following Fano's pioneering work in this field.[1] Interest in this area has been stimulated recently by the rich satellite structure exhibited in the photoelectron spectrum of Ba vapor upon excitation with He I (21.22 eV) radiation.[2-4] This structure is a result of the fortuitous overlap of the He I line with an autoionizing level of Ba I.[5] There are numerous possible transitions of the type $Ba[5p^6 6s^2] + h\nu \rightarrow Ba^*[5p^5 n\ell n'\ell' n''\ell'']$ possible in this energy region.[5] In order to systematically explore this interaction a tunable photon source in this energy range is required. Due to the low counting rates, a very efficient electron energy analyzer is also desirable. By utilizing the radiation available at the Stanford Synchrotron Radiation Laboratory (SSRL) in conjunction with a time-of-flight (TOF) photoelectron energy analyzer,[6] we have made the first measurements of the photoelectron spectra of atomic Ba at selected autoionizing resonances. This letter presents spectra taken at two of those resonances. This data implies that the dominant decay channel of the autoionizing level is via Auger decay, with Coster-Kronig transitions being preferred.

The experiments were performed at the 8^o line at SSRL. The Al window used to separate the experimental chamber from the beam line transmits photons in the energy range 7 eV < $h\nu$ < 34 eV. The basic apparatus consisted of the TOF analyzer, noninductively wound over the effusive beam source liquid nitrogen-cooled cold finger. The TOF analyzer and high temperature source are described in detail elsewhere.[6] The basic components of the TOF analyzer are a μ-metal shielded drift

tube, micro-channel plate detector, and a recently added retarding grid. By coincidencing the detected electrons with the pulsed synchrotron radiation, all electrons within a given time (energy) window are collected simultaneously. For the results reported here, it is important to note that this technique insures that fluctuation in light intensity and sample density will not affect the relative intensities observed in each spectrum.

The oven was operated at a temperature of $840^{\circ} \pm 20^{\circ}C$, as determined by an optical pyrometer, resulting in an estimated sample density of 10^{13} atoms/cm^3. A retarding field of 5 volts was used in these experiments which was found to give the best resolution without significant loss in intensity. Total counting rates varied from 5-35 sec^{-1} with an excitation band pass of 2.5 Å. The transmission of the TOF analyzer was found to be independent of energy for electron energies greater than 3 eV. Since the TOF analyzer was positioned at the "magic angle" (54.7°), the peak areas presented here are proportional to the partial ionization cross-sections.[7]

A total electron yield spectrum of Ba taken between 700 Å and 490 Å is shown in Fig. 2. All the major features of the absorption spectrum of Connerade et al.[5] are reproduced. A quantitative comparison is made difficult because the background has contributions from direct ionization, Rayleigh scattered photons, and detector dark noise. Also, the electron yield spectrum is convoluted by the transmission function of the Al window. However, the relative intensities of the peaks in the absorption and excitation spectra are comparable, which implies that most of the absorbed photons result in ionization.

Photoelectron spectra were taken at several of the peak positions in Fig. 2. The results reported here were taken at the two wavelengths indicated, 621.7 Å and 577.3 Å. Due to drifts in the zero point offset of the monochromator, we estimate an uncertainty of ± 0.7 Å in the absolute wavelength calibration.

According to Connerade et al.[5] there are several possible levels in the neighborhood of each of these lines. Examination of the photoelecgron spectra reveals extensive population of the nd levels, where n = 5 for the spectrum at 621.7 Å and n = 6 for the spectrum at 577.1 Å. This observation tends to support the assignment of the salient autoionizing levels to the first two members of the Rydberg series, $[\{5p^5 5d\ ^3P)6s\ ^2D_{3/2}\}nd]^o_{J=1}$ (series d in Ref. 5, n=5 (622.9 Å), n=6 (577.1 Å)). The following discussion should make this reasoning clearer.

In the dipole approximation, the photoionization cross-section of an atom in state i going to a final state of the ion in state j with a photoelectron of energy ε is proportional to:[8]

$$\sigma_j \alpha \left| < i \left| \sum_{n=1}^{N} \vec{r}_n \right| j, \varepsilon\ell > \right|^2 \qquad (1)$$

where $\vec{r}_n$ is the position vector of the n^{th} electron, $|i>$ is the wave function of the N-electron initial state, and $|j, \varepsilon\ell>$ is the wave function of the N-electron final state of the ion in state j plus photoelectron with energy ε and angular momentum ℓ. For Ba, $|i>$ may be given by (in LS coupling):

$$|i> = a_1 |\psi_{6s^2}> + a_2 |\psi_{6p^2}> + a_3 |\psi_{5d^2}> + \ldots . \qquad (2)$$

where the [Xe] core has been supressed. Multiconfigurational Dirac-Fock calculations by Rose et al.[9] indicate that $a_1^2 = .922$, $a_2^2 = .064$, and $a_3^2 = .014$. In the absence of autoionization, the final states, $|j, \varepsilon\ell >$ may be expressed by a single configuration, for example:[10]

$$|6d, \varepsilon\ell(^1P_1) > = \beta_1 \, |\psi_{6d}, \varepsilon\ell(^1P_1) > + \beta_2 \, |\psi_{5d}, \varepsilon\ell(^1P_1) >$$

$$+ \beta_3 |\psi_{6s}, \varepsilon\ell(^1P_1) > + \ldots . \qquad (3)$$

$$\beta_1 \sim 1 \quad \text{and all other} \quad \beta_j \sim 0.$$

Thus, in the off-resonant photoionization to the $|6d, \varepsilon\ell(^1P_1) >$ state, the main contribution to the peak intensity will come from the matrix element $< i|\vec{r}| \, \psi_{6d}, \varepsilon\ell(^1P_1) >$. In the off-resonant Ne I spectrum,[4] very little intensity ($\sim 0.7\%$) is found in the Ba^+ $(5p^6 6d)$ peak. Therefore, we may infer that $< i|\vec{r}|\psi_{6d}, \varepsilon\ell(^1P_1) > \sim 0$.

The spectrum taken at 577.3 Å (21.44 eV) reveals large population of the Ba^+ $(5p^6 6d)$ state. The cause of this may be found by again examining the form of the wave function

$$|6d, \varepsilon\ell(^1P_1) > = \beta_1 |\psi_{6d}, \varepsilon\ell(^1P_1) > + \ldots .$$

$$+ \beta_a | \, \phi_a \, > \qquad (4)$$

For brevity, states of the type B_a^{++} $(5p^6, \varepsilon\ell, \varepsilon\ell'(^1P_1))$ and B_a^{+} $(5p^5 \, n\ell n\ell', \varepsilon\ell'')$ were not included in Eq. 4, this should not effect any of the arguments presented here.

In eq.4 $|\phi_a\rangle$ represents the autoionizing level which has interacted with the continua. Upon examination of eqs. (3) and (4), it becomes apparent that the intensity of the Ba^+ $(5p^6 6d)$ peak for the 21.44 eV spectrum must be derived from the $\langle i|\vec{r}|\phi_a\rangle$ matrix element. The coefficient β_a is proportional to the matrix element $\langle 6d, \varepsilon\ell(^1P_1)\ |V|\phi_a\rangle$ where $V = \sum_{i,j} r_{ij}^{-1}$.[11] Thus β_a will be large for the Ba^+ $(5p^6 6d)$, Ba^+ $(5p^6 5d)$, and Ba^+ $(5p^6 6s)$ which may interact via direct Auger decay with the $\{(5p^5 5d\ ^3D)6s\ ^2D_{3/2}\}6d$ autoionizing level. Similarly, for the $\{(5p^5 5d\ ^3D)6s\ ^2D_{3/2}\}5d$ state, β_a will be large for the Ba^+ $(5p^6 6s)$ and Ba^+ $(5p^6 5d)$ states.

The preceding example was used in order to give a qualitative feeling for the results presented here, and is by no means rigorous. The complexity of the Ba system and the relatively broad (2.5 Å) photon source precludes a detailed analysis. In order to explain all the peaks in the spectra, a detailed calculation is needed using relativistic, multiconfigurational wave functions for both the autoionizing levels and the continua.

These results are consistent with arguments presented by Fano and Cooper,[2] and the formalism developed by Davis and Feldkamp[11] which was used to explain the absorption spectra of atomic Mn.[13] Similar arguments have also been invoked to explain electron energy loss[14] and photoemission[15] spectra of Ni metal. Wendin[16] has applied many body techniques and arrived at similar conclusions in regard to resonances in satellite structure. Population of satellite levels via autoionization has also been noted in the photoemission spectra of Xe and Kr[17] and spectra of Mg,[8] Ca,[19] Sr,[20] and Ba and Yb.[21] Analysis of

these spectra also imply that Auger decay is a preferred channel for autoionization.

Further proof of the importance of this mechanism in autoionization is offered by the He I spectrum of Ba.[4] Originally, we conjectured that the sudden increase in intensity [22] for the peak at 14.22 eV binding energy (labeled 10 in our work) seemed inconsistent with that peak being due to high Rydberg excitation, i.e., $B_a^+ 5p^6$ 11s, and that perhaps autoionization from the He I β line (537 Å) might play a role. However, Connerade et al.[5] assign the level at He I (584.3 Å) to excitation of an 11s electron which implies that the [$Ba^+ 5p^6$ 11s] assignment for the peak at 14.22 eV is correct and is consistent with the present results. Connerade et al. do not specify the symmetry of the core, a level containing large contributions from configurations of type $[5p^5\ 5d^2\ 11s]^o_{J=1}$ and $[5p^5\ 5d6d\ 11s]^o_{J=1}$ would be in line with the large intensities of the [$Ba^+ 5p^6$ 5d] and [$Ba^+ 5p^6$ 6d] levels.

Table 1

States of Ba^+ and Relative Peak Intensities Observed at the Two Autoionizing Resonances

Ba^+	State[a]	Binding energy (eV)	Intensity[b] 621.7 Å (622.9 Å)[c]	Intensity[b] 577.1 Å (577.3 Å)[c]
6s	$^2S_{1/2}$	5.21	100	100
5d	$^2D_{3/2,5/2}$	5.86	224	43
6p	$^2P_{1/2}$	7.72	26	(8)
	$^2P_{3/2}$	7.93	11	33
7s	$^2S_{1/2}$	10.46	(2)	14
6d	$^2D_{3/2,5/2}$	10.92	6	63
4f	$^2F_{5/2,7/2}$	11.2	(3)	22
7p	$^2P_{1/2,3/2}$	11.4	(2)	(2)
5f	$^2F_{5/2,7/2}$	12.3		12
8s	$^2S_{1/2}$	12.4		
7d	$^2D_{3/2,5/2}$	12.6		13
8p	$^2P_{1/2,3/2}$	12.8		(2)
5g	$^2G_{7/2,9/2}$	13.0		(2)
6f	$^2F_{5/2,7/2}$	13.2		

[a] The [Xe] core has been suppressed in this notation.

[b] Intensities are referenced to the Ba^+ 6s line, and have less than 5% error. Values in parenthesis have greater errors.

[c] Value in parentheses is based on that given in Ref. 5.

622.9 Å $\equiv [\{(5p^5 5d\ ^3P)6s\ ^2D_{3/2}\}5d]^o_{J=1}$

577.3 Å $\equiv [\{(5p^5 5d\ ^3P)6s\ ^2D_{3/2}\}6d]^o_{J=1}$

REFERENCES

1. U. Fano, Phys. Rev. 124, 1866 (1961).

2. B. Brehm and K. Höfler, Int. J. of Mass. Spec. and Ion Physics 17, 371 (1975).

3. H. Hotop and D. Mahr, J. Phys. B. 8, L301 (1975).

4. S.-T. Lee, S. Süzer, E. Matthias, R. A. Rosenberg, and D. A. Shirley, J. Chem. Phys. 66, 2496 (1977).

5. J. P. Connerade, M. W. D. Mansfield, G. H. Newson, D. H. Tracy, M. A. Baig, and K. Thimm, Phil. Trans. R. Soc. Land A 290, 327 (1979).

6. a) M. G. White, R. A. Rosenberg, G. Gabor, E. D. Poliakoff, G. Thornton, S. H. Southworth, and D. A. Shirley, submitted to Rev. Sci. Inst.

   b) R. A. Rosenberg, Ph.D. Thesis (1979).

7. J. Cooper and R. N. Zare, J. Chem. Phys. 48, 942 (1968).

8. D. R. Bates, Mon. Not. Roy. Astr. Soc. 106, 432 (1946).

9. S. J. Rose, N. C. Pyper, and I. P. Grant, J. Phys. B. 11, 755 (1978).

10. The method of Continuum State Configuration Interaction (CSCI), where the photoelectron is coupled to the configuration before the mixing, is used in this example. Coupling the photoelectron after the mixing is achieved is known as Final Ionic State Configuration Interaction (FISCI). Since Ba^+ is hydrogenic, FISCI is not thought to be important. In the absence of a resonance CSCI can usually be neglected so the two treatments should give equivalent results.

11. a) L. C. Davis and L. A. Feldkamp, Phys. Rev. B 15, 2961 (1977).

b) and Phys. Rev. A 17, 2012 (1978).

12. U. Fano and J. W. Cooper, Phys. Rev. 137, A1364 (1965).

13. a) J. P. Connerade, M. W. D. Mansfield, and M. A. P. Martin, Proc. R. Soc. Land. A 350, 405 (1976).

b) R. Bruhn, B. Sonntog, and H. W. Wolff, Phys. Lett. 69A, 9 (1978).

14. R. E. Dietz, E. G. McRae, Y. Yafet, and C. W. Caldwell, Phys. Rev. Lett. 33, 1372 (1974).

15. C. Guillot, Y. Ballu, J. Paigne, J. Leconte, K. P. Gain, P. Thiry, R. Pinchaux, Y. Petroff, and L. M. Falicov, Phys. Rev. Lett 39, 1632 (1977).

16. G. Wendin in "Photoionization of Atoms and Molecules," Proceedings of the Daresbury one-day meeting, 16 February 1978.

17. W. Eberhardt, G. Kalkoffen, and C. Kunz, Phys. Rev. Lett. 41, 156 (1978).

18. a) B. Breukmann, V. Schmidt, and W. Schmitz, J. Phys. B. 9, 3037 (1976).

b) V. Pejcev, T. W. Ottley, D. Rassi, and K. J. Ross, J. Phys. B 10, 2389 (1977).

19. V. Pejcev, I. W. Ottley, D. Rassi, and K. J. Ross, J. Phys. B. 11, 531 (1978).

20. M. D. White, D. Rassi, and K. J. Ross, J. Phys. B. 12, 315 (1979).

21. R. A. Rosenberg, S.-I. Lee, and D. A. Shirley, to be published.

22. Although the He I work was done at an angle of 90°, preliminary studies done by us at 584 Å and 54.7° qualitatively reproduce

the relative intensities observed, indicating that corrections for angular anisotropies are not of major importance. Also, note in this earlier work that the relative intensities of peaks 8, 9, and 10 were inadvertently given the values of 0.28, 0.40, and 0.65, respectively, in Table 1. They should be 28, 40, and 65.

FIGURE CAPTIONS

Fig. 1. Total electron yield spectrum of atomic Ba. The data has been smoothed with a spline fitting routine.

Fig. 2. Photoelectron spectra of atomic Ba taken at two autoionizing resonances. The assignments are from Ref. 5. The background has been subtracted and the data smoothed with a spline fitting routine.

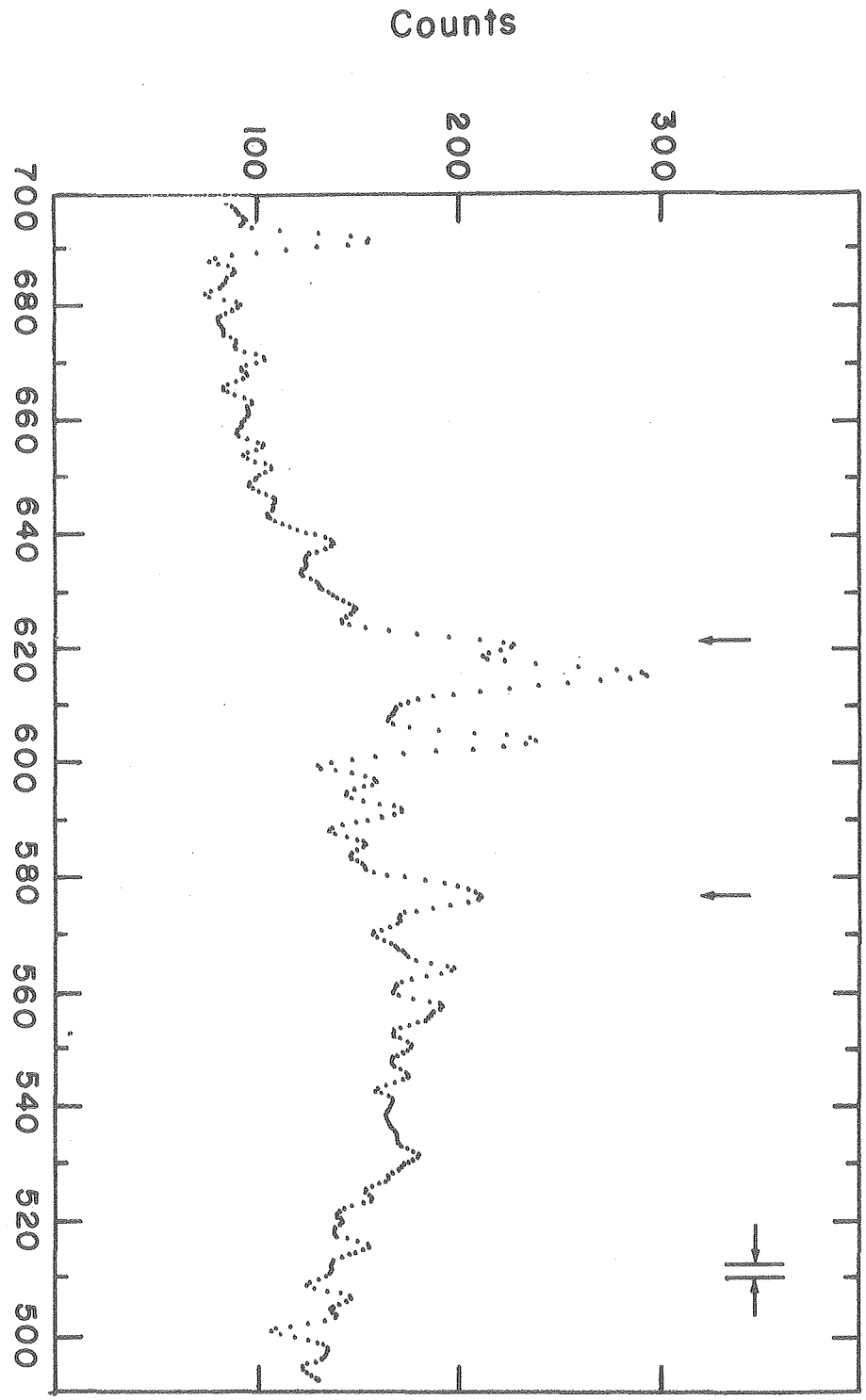

Fig. 1

XBL 793-8812

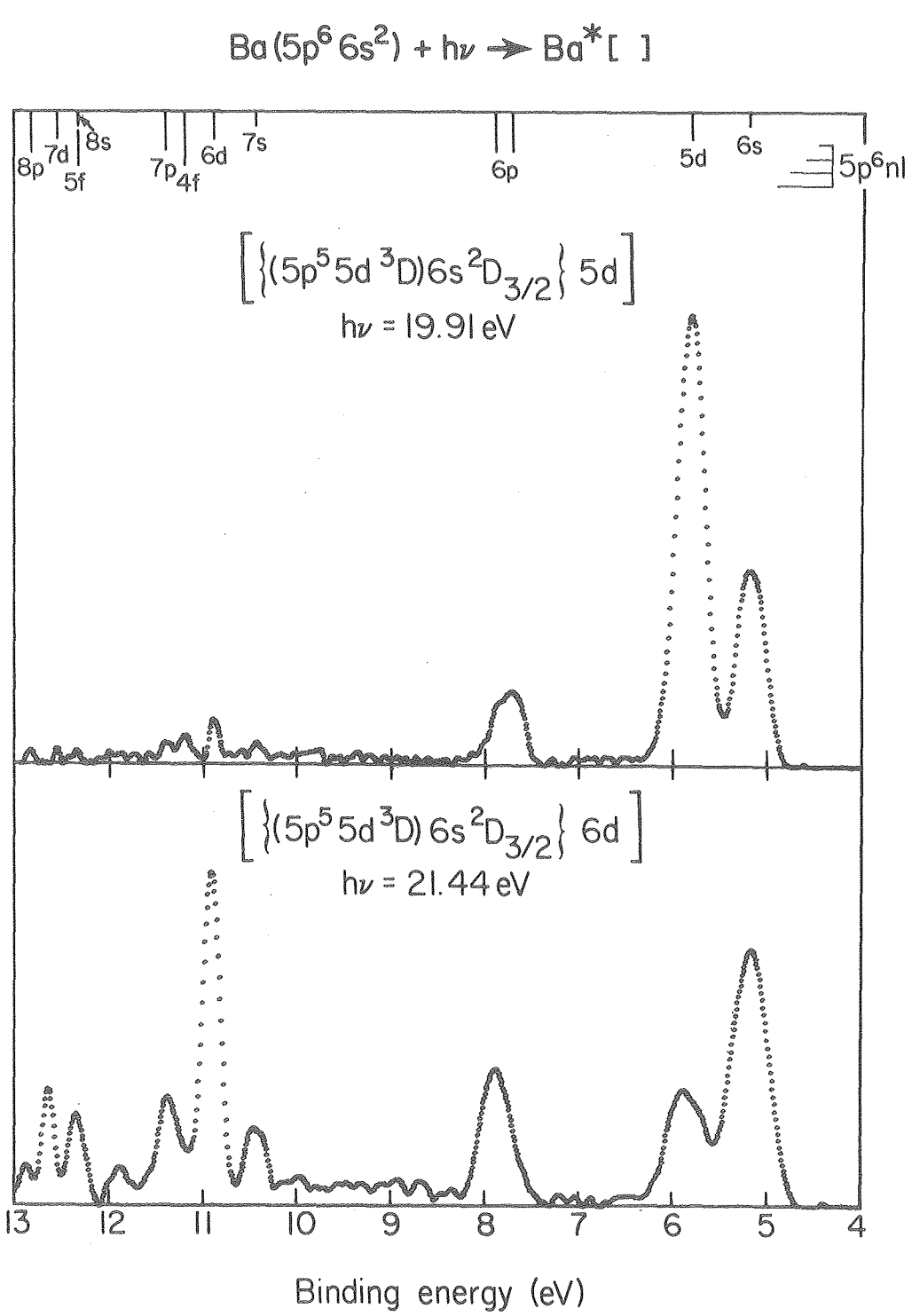

XBL 792-610

Fig. 2

VI. OBSERVATION OF A COLLECTIVE EXCITATION IN THE EJECTED ELECTRON SPECTRA OF Yb AND Ba*

ABSTRACT

Ejected electron spectra of Yb and Ba are presented. In both spectra, structure was seen which is attributable to autoionization to ground and excited states of M^+ (M = Ba or Yb), and to Auger decay of highly excited M^{*+} states to the ground state of M^{++}. In Yb, Auger decay was also observed to populate excited states of M^{++}. Both spectra are strongly affected by a collective resonance in the excitation of a 5p electron. For energies above the 5p ionization threshold, two-step autoionization to M^{++} was found to be dominant.

---

*Work done in collaboration with S.-T. Lee and D. A. Shirley

A. Introduction

Excitation of an atomic electron other than the most loosely bound one, or the simultaneous excitation of two or more electrons, can yield a set of energetically discrete excited states embedded in a continuum. Electron correlation may mix the discrete state with the continuum, leading to eigenstates with sufficient continuum character to produce spontaneous ionization or autoionzation. Spontaneous ionization can also occur following inner-shell ionization, as a result of interactions between singly and doubly charged hole states; autoionization in this case is usually referred to as the Auger effect.[1] Either autoionization or Auger electron spectra contain unique information about electron correlation effects analogous to satellite peaks in photoelectron spectra.[2,3]

Autoionization or ejected electron spectra can be excited and investigated in a number of ways, including photon impact,[4] electron impact,[4] ion impact,[5] and beam-foil spectroscopy.[6] Because of differences in the modes of excitation and variation of the selection rules, the different types of spectroscopy provide complementary information. A great deal of work has been done on the autoionization of rare gases, but relatively little on atoms of nonvolatile elements, such as metal vapors, in part because of the technical complexities.[7] Recently, we have found that the UV lamp in our photoelectron spectrometer can be used as an electron source. By using it in conjunction with an oven, we can thus readily study the autoionization electron spectra of high-temperature vapors.[7] In this paper we report measurements of the ejected electron spectra of Yb and Ba following the excitation or

ionization of one of the outermost $5p^6$ electrons.

The ejected electron spectra of the alkaline earths Mg,[8] Ca,[9] and Sr[10] have recently been analyzed. In addition, Aleksakhin, et al.[11] and Mehlhorn, et al.[12] have communicated preliminary results on the electron spectrum of Ba. To our knowledge the results given below are the first reported measurements of the ejected electron spectrum of Yb.

To ascertain the relevant levels which contribute to the autoionization or Auger decay, it is necessary to determine the energies of these levels. For Yb, the primary source of this information comes from the Yb I absorption work of Tracy.[13] These studies show the energies of the optically allowed transitions of the type $Yb[5p^6 4f^{14} 6s^2] \rightarrow Yb^*[5p^5 4f^{14} n\ell n'\ell']_{J=1}$. Since all these levels lie in the continuum of Yb II, they may autoionize. The series limits of these lines $(Yb^+[5p^5 4f^{14} n\ell]_{J=3/2,1/2})$ lie in the continuum of Yb III and hence may Auger-decay.

The situation in Ba is much more complicated. Recent photoabsorption studies by Connerade, et al.[14] show the positions of numerous levels of the type $Ba^*[5p^5 n\ell n'\ell' n''\ell'']_{J=1}$, all of which may autoionize. Roig[15] has recently reported the UV absorption spectrum of Ba II, which gives the positions of many levels of the type $Ba^+[5p^5 n\ell n'\ell']$, which may Auger-decay; some of these levels serve as series limits in the work of Connerade, et al.[14] In addition to these photon impact studies, there have been electron impact/mass spectroscopic experiments performed on Ba and Ba^+;[16] these investigations yield complimentary results to the photoabsorption work, although they are inherently less sensitive.

Thus, even though Yb has f electrons and therefore more possible final states, the ejected electron spectrum is much simpler than that of Ba. This simplicity is a manifestation of the dominance of the so-called "giant resonance" for 5p excitation. This resonance (nominally $5p^5 6s^2 5d\ ^1P_1$) was first predicted by Wendin[17] and later observed by Tracy[13] in the 5p absorption spectrum of the lanthanides. As discussed by Connerade and Tracy,[18] the near degeneracy of the 6s and 5d shells in Ba and La effectively "shatters" this resonance and the oscillator strength is spread over many levels.

This paper deals with the various decay channels which may contribute to the observed spectra. Pertinent experimental details are given in Section B and results in Section C. The various mechanisms are discussed for each spectrum in Section D. Conclusions are given in Section E.

B. Experimental

The electron spectra were recorded using a Perkin-Elmer PS-18 photoelectron spectrometer modified for digital counting and high temperature studies.[19] The experimental procedures were similar to those employed in photoelectron spectroscopy[3b] except that the electron source was provided by the UV lamp operated in the electron mode. The operation and characteristics of a capillary discharge lamp as an electron source has been discussed by Lee, et al.[7]

The electron spectra were measured with the lamp adjusted to give an optimum compromise of resolution, signal intensity, and signal-to-background ratio.[7] Under these conditions the pressure in the lamp was held between 50 and 100 microns and that in the main vacuum chamber

was in the low 10^{-5} torr range. To ascertain that the spectra were independent of the ions present in the lamp, each metal vapor was studied with both He and Ne lamps. The spectra thus obtained were found to be identical except for slight variations in relative peak intensities, which were attributed to lamp fluctuations and variations of the analyzer transmission. The contribution to the spectra due to ionization by (He^+ or Ar^+) ion impact was thus estimated to be negligible. This is further substantiated by the fact that few ions impinged upon the anode of the lamp and subsequently made their way into the ionization chamber to cause ionization.[7] Calibration of the spectra was accomplished by referencing to the photoelectron lines of the metals, Xe, and/or N_2 with the lamp operated simultaneously in both photon and electron modes.[7]

C. Results

The ejected electron spectra of Yb and Ba are shown in Figs. 1 and 2, respectively. These spectra represent raw data with no smoothing, background subtraction, etc., and were recorded with an energy resolution of 1-2%. The nonlinear background is a result of the characteristics of the electron source.[7] Due to the complexity of the spectra, only the electron lines with appreciable intensities, i.e., larger than 1% of the most intense line, are identified and numbered in the figures. In many instances, as can be seen in the spectra, the width and profile of an individual line suggests it actually consists of several lines. The energies and relative intensities of the electron lines are collected in Tables 1 and 2. The intensities have been corrected for energy dependence only, and thus carry large uncertainties. They are included primarily for qualitative discussion.

D. Discussion

Following the electron impact excitation of one of the outermost core-like electrons in Ba or Yb, there are three possible ways to produce ejected electrons with discrete energies. They are designated e_1, e_2, and e_3 in Fig. 3 and correspond to the following autoionization processes:

$$M^*(5p^5 n\ell n'\ell' n''\ell'') \rightarrow M^+(5p^6 6s \text{ or } 5p^6 n\ell) + e_1$$

$$M^*(5p^5 n\ell n'\ell' n''\ell'') \rightarrow M^{*+}(5p^5 n\ell n'\ell') + e_2$$

$$M^{*+}(5p^5 n\ell n'\ell') \rightarrow M^{++}(5p^6 \text{ or } 5p^6 4f^{13} n\ell(Yb)) + e_3$$

Electrons e_1, e_2, and e_3 lie in different energy regions and can thereby usually be distinguished from one another. Generally speaking, e_2 type electrons are of extremely low energy, and the centers of electron groups e_1 and e_3 separated by the binding energy of M^+. Due to poor transmission of the analyzer at low energies we were unable to detect e_2 electrons.

This Section deals with the possible decay channels which account for the observed spectra. In both spectra, structure was observed which may be attributed to autoionization and Auger decay. Since the Yb spectrum lends itself relatively easily to interpretation, it will be discussed first.

1. Yb($5p^6 4f^{14} 6s^2$)

a. Autoionization (e_1 electrons, Fig. 3)

The 5p absorption spectrum of Yb I below the $(5p^5 6s^2)\,^2P_{3/2}$ threshold is dominated by two intense peraks at excitation energies (E_a) of 27.63 eV and 28.23 eV. Tracy has assigned these peaks to the

$5p^5(^2P_{3/2})4f^{14}6s^2 5d[1/2]_1$ and $5p^5(^2P_{3/2})4f^{14}6s^2 5d[3/2]_1$ levels of Yb I.[13] Autoionization of these two states to the ground state of Yb II, $(5p^6 4f^{14}6s^2\ ^2S_{1/2})$ will give rise to two electron peaks at energies of E_a - B.E.(6s), where B.E.(6s) is the binding energy of a 6s electron (6.25 eV[20]). These energies correspond to peaks 23 and 24 in Fig. 1. In addition, it is possible for these levels to autoionize to excited states of Yb II, such as $5p^6 4f^{13}6s^2\ ^2F_{7/2,5/2}$, $5p^6 4f^{14}5d\ ^2D_{5/2,3/2}$, and $5p^6 4f^{14}6p\ ^2P_{3/2,1/2}$. Such transitions account for the observed intensity between 17 eV and 20 eV in Fig. 1. It is also possible to identify some of the less intense peaks in Fig. 1 with weaker features observed in the absorption spectrum. These assignments are summarized in Table 1.

In the region between the $5p^5\ ^2P_{3/2}$ and $^2P_{1/2}$ thresholds lies the so-called "giant resonance" $(5p^5(^2P_{1/2})6s^2 5d[3/2]_1$ (33.29 eV, 1.4 eV FWHM).[13] Decay of this state to the ground state of Yb II should yield an e_1 electron of energy 27.04 eV. Since the resonance is so broad, it is possible that the weak feature (peak 27) at 27.33 eV is a result of this decay. Since the absorption peak is so intense, it seems surprising that the corresponding electron peak is so weak. However, other experimental evidence suggests the reason for this is that the "giant resonance" decays primarily to the Yb II $(5p^5 6s^2\ ^2P_{3/2})$ state, with release of an e_2 electron. This state then Auger decays to ground and excited states of Yb III. The reasoning for this will become clearer in the next section.

b. Auger decay (e_3 electrons, Fig. 3)

Decay of the Yb II $5p^5 4f^{14} 6s^2\ ^2P_{3/2}$ (31.350 eV) state to the ground state of Yb III $5p^6 4f^{14}\ ^1S_0$ (18.44 eV[20]) yields an electron of 12.91 eV kinetic energy. This corresponds to the intense peak (13) in the electron spectrum. It is also possible to identify decay to excited configurations of Yb III, such as $4f^{13}6s$, $4f^{13}5d$, and $4f^{13}6p$. Using the Yb III energy levels given by Martin, et al.,[20] we have assigned most of the lower energy features to this process. This information is summarized in Table 1.

We note the absence of a peak corresponding to the transition $5p^5 4f^{14} 6s^2\ ^2P_{1/2} \rightarrow 5p^6 4f^{14}\ ^1S_0$ which should appear at 19.08 eV. Peak 14 at 13.47 eV may be assigned to the $5p^5 4f^{14} 6s^2\ ^2P_{1/2}$ state decaying to the $5p^6 4f^{13} 6s$ level.[21] However, the intensities of these peaks are much smaller than one would expect if the $5p^5 6s^2\ ^2P_{3/2}$ and $^2P_{1/2}$ levels were populated statistically. Statistical behavior would be expected if direct ionization (path B, Fig. 3) were the dominant mechanism by which the $^2P_{3/2}$ and $^2P_{1/2}$ states were populated. Consequently, excitation (path A, Fig. 3) followed by autoionization with ejection of e_2 electrons appears to be the dominant path.

The behavior has been observed to a lesser extent in the lighter alkaline earths, Sr and Ca ($np^6(n+1)s^2$), and is due to the collapse (or near degeneracy) of the nd into the (n+1)s shell as a result of np excitation or ionization. We note, however, the corresponding arguments do not apply to Mg, where 3s and 3d shells are involved, and consequently autoionization e_2 is not readily allowed on energy grounds. Therefore, the low energy electron spectrum of Mg^5 is dominated by the

$2p^5 3s^2$ autoionizing states as expected from direction ionization. As one proceeds from Mg to Ba, the effect becomes more pronounced[8-12] and at Yb there is little if any population of the $5p^5 6s^2\ ^2P_{3/2}$ state.

Such behavior is reasonable in light of the huge oscillator strength observed by Tracy for the giant resonance in Yb II.[13] It was noted above that the branching ratio for autoionization of this state to the ground state of Yb II was almost negligible. The only other non-radiative decay channel of this level is autoionization to the $5p^5 4f^{14} 6s^2\ ^2P_{3/2}$ level. Auger decay of this state leads to most of the observed low energy peaks in the spectrum.

Tracy commented on this aspect of the giant resonance in Yb.[13] Hansen[23] and Connerade, et al.[24] invoked a similar two-step autoionization process to explain the double ionization anomaly in Ba I when excited with He I radiation.

2. Ba($5p^6 6s^2$)

a. Autoionization

As mentioned previously, the Ba I 5p absorption spectrum is immensely complex. In order to assign this spectrum, Connerade, et al.[14] grouped the lines into twelve series. The series limits were found from levels observed in the 5p absorption spectrum of Ba II.[15] The lowest of these autoionizing levels, and one of the most intense, lies at 17.87 eV above the ground state. Autoionization of this state to the ground state of Ba II yields an e_1 electron with 12.66 eV kinetic energy, coinciding with peak 31 in Fig. 2. It is also possible to identify peaks corresponding to decay of this level to specific excited states of Ba II; i.e., $5p^6 5d\ ^2D_{5/2,3/2}$ and $5p^6 6p\ ^2P_{3/2,1/2}$. The $5p^6 6p\ ^2P_{1/2}$ state is not

identified in our spectrum; however, it does appear clearly in the work of Aleksaksin, et al.[25] The relative intensities of these satellites is in qualitative agreement with recent photoemission work on Ba I.[26]

We also believe that the intense peaks at higher energies than peak 31 are due to autoionization to the ground state of Ba II. According to the absorption data of Roig,[15] it is also possible to identify most of these lines with Auger transitions (see Table 2). The assignment of these peaks to autoionization is supported by the fact that peaks 22-30 are of relatively low intensity and thus are probably due to some second-order process (such as the satellite lines mentioned earlier). The abrupt rise in intensity at peak 31 implies that a new channel has opened. Since peak 31 has been identified as a primary autoionizing transition, the implication is that the other strong higher energy peaks occur via this mechanism. This type of "two region" behavior was seen earlier in the spectrum of Yb and has also been observed in Ca[9] and Sr.[10] Aleksakhin, et al.[11] invoked similar reasoning in their discussion of Ba. Unfortunately, the relatively poor electron energy resolution and the large density of autoionizing states in this region[14] ($19\ eV < h\nu < 22\ eV$) precludes assignment of the lines in the corresponding electron spectrum ($14\ eV < E < 17\ eV$) to individual autoionizing transitions.

b. Auger decay

Based on energy considerations, it seems likely that most of the peaks 1-22 are due to Auger transitions. All of these peaks are also seen in the electron impact work of Mehlhorn, et al.[12] who used 2 keV electrons for excitation. They reported binding energies for the $5p^5 6s^2\ ^2P_{3/2}$ and $^2P_{1/2}$ states of 22.75(5) eV and 24.76(2) eV, in good agreement with our values based on the positions of peaks 15 and 22 (22.79(9) eV, 24.76(9) eV). As mentioned earlier, the assignment of these states is nominal since the near degeneracy of the 5d levels effectively "smears out" these states as is indicated by the large number of peaks (states) in this region.

Peaks 1-3 appeared as very intense structure in the He I photoelectron spectrum of Ba.[27] At that time it was postulated that path A (Fig. 3) was the primary mechanism by which the $5p^5 n\ell n'\ell'$ states were populated. These states lie at ∿15.8 eV above the ground state of Ba II. This is the same energy as the first autoionizing threshold observed by Peart, et al.[16b] in electron impact mass spectroscopic studies on Ba^+. Multi-configurational Hartree-Fock calculations by Hansen[28] assigned these levels to the $5p^5 5d(^3P)6s\ ^2P$ configuration, and they are the lowest lying autoionizing levels for Ba II. This conclusion is supported by multi-configurational Dirac-Fock calculations of Connerade, et al.[24] Roig observed weak structure as low as 14.7 eV, but his spectrum was complicated by excitation from the metastable $5p^6 5d\ ^2D_{5/2,3/2}$ levels.[15]

Thus, the first peaks in the ejected electron spectrum come at energies corresponding to the first possible Auger states in Ba II.

Most of the other peaks, 4-22, are due to Auger decay of higher-lying levels. In order for these states to be populated via autoionization of Ba I (step A, Fig. 3), autoionizing levels with Ea > 21.0 eV are required. Decay of these levels to the ground state of Ba II would yield electrons with Ee > 15.8 eV. It is interesting to note that the ejected electron spectrum shows very little intensity after this threshold. This implies, as noted earlier in Yb, that once the Auger channel becomes energetically possible, the Ba I $5p^5n\ell n'\ell'n''\ell''$ levels preferentially populate these Ba II $5p^5n\ell n'\ell'$ states (e_2 electrons) at the expense of the Ba II $5p^6n\ell$ states (e_1 electrons).

This explanation is also consistent with the relatively large ratio (R) of Ba^{++}/Ba^{+} ions induced by He I radiation (21.2 eV), R = 2.4(6)[29] as compared to that induced by Ne I radiation (16.8 eV), R = .25(5),[29] as well as the ratio induced by He metastables,[30] $2\,^3S$ (19.8 eV), R = .010(5), and $2\,^1S$ (20.6 eV), R = .018(6). The He I radiation coincides with an autoionizing level above the first $(5p)^{-1}$ threshold, while the Ne I radiation is both off resonance and below this threshold. While there are a number of strong autoionizing states capable of being populated by the He metastables, they all lie below the first $(5p)^{-1}$ threshold.

Because the e_2 electrons populating the Ba II $5p^5n\ell n'\ell'$ are very low in energy, it is possible that some of the Auger decay is influenced by post-collisional interaction (PCI) effects.[31] It is not possible to assess the magnitude of the effect in the spectra presented here; it may be responsible for shifting some of the Auger peaks in energy and causing them to be asymmetric.

E. Conclusions

Ejected electron spectra of Ba and Yb have been presented. These are the first such spectra of Yb. Analysis of the spectra shows autoionization to both ground and excited states of M^+ ($5p^6n\ell$), Auger decay to the ground state of M^{++} ($5p^6$), and for Yb, Auger decay to excited states of M^{++} ($5p^64f^{13}n\ell$). The evidence indicates that autoionization to the ground and excited states of M^+ ($5p^6n\ell$) is only appreciable below the first $(5p)^{-1}$ ionization threshold. Above this level, autoionization proceeds primarily in a two-step manner: first, to the highly excited M^+ $5p^5n\ell n'\ell'$ states and then Auger decay to the ground state(s) of M^{++}.

If this hypothesis is correct, then mass spectroscopic studies done at some of the stronger Ba I autoionizing resonances above the first $(5p)^{-1}$ threshold, should yield an even larger ratio of M^{++}/M^+ then the value of 2.4(6) observed by Brehm and Bucher using He I radiation[29] (this is a relatively weak resonance in the absorption spectrum). This effect should be especially dramatic at the energy of the "giant resonance" in Yb I.[13] In order to characterize this process further, studies using variable energy electrons and photons are required. We have recently begun such work on Ba, using synchrotron radiation.

REFERENCES

1. P. Auger, J. Phys. Radium. 6, 205 (1925); Ann. Phys. (Paris) 6, 183 (1926).

2. U. Fano, Phys. Rev. 124, 1866 (1961); U. Fano and J. W. Cooper, Phys. Rev. 137, A1364 (1965).

3. a. R. L. Martin and D. A. Shirley, Phys. Rev. A13, 1475 (1976); b. Ş. Süzer, S.-T. Lee, and D. A. Shirley, Phys. Rev. A13, 1842 (1976).

4. For example, see K. Siegbahn, C. Nordling, G. Johansson, J. Hedman, P. F. Hedén, K. Hamrin, U. Gelius, T. Bergmark, L. O. Werme, R. Manne, and Y. Baer, ESCA Applied to Free Molecules (North-Holland Publishing Co., Amsterdam, 1969).

5. P. Ziem, G. Wüstefeld, and N. Stolterfoht, Abstracts of 2nd Inter. Conf. Inner Shell Ioniz. Phenomena, Freiburg, W. Germany, April, 1976; D. J. Pegg, H. H. Hazelton, R. S. Thoe, P. M. Griffin, M. D. Brown, and I. A. Sellin, Phys. Rev. A12, 1330 (1975).

6. R. Bruch, G. Paul, and J. Andrä, Phys. Rev. A12, 1808 (1975) and references therein.

7. S.-T. Lee, R. A. Rosenberg, E. Matthias, and D. A. Shirley, J. Electron Spectrosc. and Rel. Phen. 10, 203 (1977).

8. a. B. Breukmann, V. Schmidt, and W. Schmitz, J. Phys. B 9, 3037 (1976). b. V. Pejčev, T. W. Ottley, D. Rassi, and K. J. Ross, J. Phys. B 10, 2389 (1977).

9. V. Pejčev, T. W. Ottley, D. Rassi, and K. J. Ross, J. Phys. B 11, 531 (1978).

10. M. D. White, D. Rassi, and K. J. Ross, J. Phys. B 12, 315 (1979).

11. I. S. Aleksakhin, A. S. Borovik, and I. P. Zapesochnyi, JETP Lett. 26, 314 (1977).

12. W. Mehlhorn, B. Breukmann, and D. Hausamann, Physica Scripta 16, 177 (1977).

13. D. H. Tracy, Proc. R. Soc. Lond. A. 357, 485 (1977).

14. J. P. Connerade, M.W.D. Mansfield, G. H. Newsom, D. H. Tracy, M. A. Baig, and K. Thimm, Phil. Trans. R. Soc. Lond. A. 290, 327 (1979).

15. Randy A. Roig, J. Opt. Soc. Am. 66, 1400 (1976).

16. a. Sadayuki, Okudaira, J. Phys. Soc. Japan 29, 409 (1970);

b. B. Peart, J. G. Stevenson, and K. T. Dolder, J. Phys. B 6, 146 (1973).

c. B. Peart and K. T. Dolder, J. Phys. B 1, 872 (1968).

17. a. G. Wendin, Phys. Lett. 46A, 119 (1973);

b. G. Wendin, Vacuum Ultraviolet Radiation Physics, (Vieweg-Pergamon, 1974), p. 235.

18. J. P. Connerade and D. H. Tracy, J. Phys. B 10, L235 (1977).

19. Ş. Süzer, M. S. Banna, and D. A. Shirley, J. Chem. Phys. 63, 3473 (1975).

20. W. C. Martin, R. Zalubas, and L. Hagon, Atomic Energy Levels — The Rare-Earth Elements, Nat. Stand. Ref. Data Ser., Nat. Bur. Stand. (U.S.), 60 (1978).

21. It is also possible that peaks 14 and 15 result from the Auger decay of states resulting from the $5p^5 4f^{14} 6s5d$ configuration. However, the energies of these levels are not known.

22. W. Schmitz, B. Breukmann, and W. Mehlhorn, J. Phys. B 9, L493 (1976).

23. J. E. Hansen, J. Phys. B 8, L403 (1975).

24. J. P. Connerade, S. J. Rose, and I. P. Grant, J. Phys. B 12, L53 (1979).

25. Peak 29 in Ref. 11. Note that the energies given in Ref. 11 seem to be systematically ∿.2 eV too high. This conclusion is based on a comparison with the present results and those given in Ref. 12.

26. R. A. Rosenberg, et al., to be published.

27. a. S.-T. Lee, Ş. Süzer, E. Matthias, R. A. Rosenberg, and D. A. Shirley, J. Chem. Phys. 66, 2496 (1977).

b. H. Hotop and D. Mahr, J. Phys. B 8, L301 (1975).

28. J. E. Hansen, J. Phys. B 7, 1902 (1974).

29. B. Brehm and A. Bucher, Int. J. Mass Spec. and Ion Phys. 15, 463 (1974).

30. K. Gerard and H. Hotop, Chem. Phys. Lett. 43, 175 (1976).

31. For example, see V. Schmidt, N. Sandner, W. Mehlhorn, M. Y. Adam, and F. Wuilleumier, Phys. Rev. Lett. 38, 63 (1977).

32. C. E. Moore, Nat. Bur. Stand (U.S.A.) Circ. 467, Vol. 3 (1962).

Table 1. Energies, Intensities, and State Assignments of Peaks Seen in the Ejected Electron Spectrum of Yb.

No. of Peak	Kinetic[a] Energy (eV)	Relative[b] Intensity	Assignment[c]
1	3.26	26	Yb II $(^2P_{3/2}) \rightarrow [4f^{13}(^2F_{7/2})6P_{3/2}]_{J=2,5}$ (3.23)
2	4.03	21	Yb II $(^2P_{3/2}) \rightarrow [4f^{13}(^2F_{7/2})6P_{1/2}]_{J=3}$ (4.00)
3	4.79	12	
4	5.90	13	
5	6.30	37	Yb II $(^2P_{3/2}) \rightarrow [4f^{13}(^2F_{5/2})5d_{5/2 \text{ or } 3/2}]_{J=4 \text{ or } 1}$ (6.27)
6	6.57	21	Yb II $(^2P_{3/2}) \rightarrow [4f^{13}(^2F_{5/2})5d_{5/2}]_{J=2}$ (6.53)
7	7.33	53	Yb II $(^2P_{3/2}) \rightarrow [4f^{13}(^2F_{5/2})6S_{1/2}]_{J=2,3}$ or $[4f^{13}(^2F_{5/2})5d_{5/2}]_{J=0}$ (7.33)
8	7.56	23	Yb II $(^2P_{3/2}) \rightarrow [4f^{13}(^2F_{7/2})5d_{5/2}]_{J=3,4,5}$ (7.58)
9	7.96	44	Yb II $(^2P_{3/2}) \rightarrow [4f^{13}(^2F_{7/2})5d_{5/2}]_{J=1,2,6}$ (7.99)
10	8.57	100	Yb II $(^2P_{3/2}) \rightarrow [4f^{13}(^2F_{7/2})5d_{3/2}]_{J=3,4}$ (8.59)
11	9.26	5	
12	10.8	5	
13	12.92	93	Yb II $(^2P_{3/2}) \rightarrow 4f^{14}\ ^1S_0$ (12.91)
14	13.47	27	Yb II $(^2P_{1/2}) \rightarrow [4f^{13}(^2F_{7/2})5d_{3/2}]_{J=2,3}$ or $[4f^{13}(^2F_{5/2})5d_{5/2}]_{J=0}$ (13.50)
15	14.00	11	
16	14.73	7	Yb I $5p^5(^2P_{3/2})6s^2 7d[1/2]_1 \rightarrow 5p^6 7d\ ^2D_{5/2,3/2}$ (14.81)
17	15.98	3	Yb I $5p^5(^2P_{3/2})6s^2 6d[1/2]_1 \rightarrow 5p^6 6d\ ^2D_{5/2,3/2}$ (16.00)
18	16.34	3	
19	17.39	29	Yb I $5p^5(^2P_{3/2})6s^2 5d[1/2]_1 \rightarrow 5p^6 4f^{13}6s^2(^2F_{7/2})$ (17.47)
20	18.09	13	Yb I $5p^5(^2P_{3/2})6s^2 5d[1/2]_1 \rightarrow 5p^6 4f^{13}6s^2(^2F_{5/2})$ (18.07)
21	18.61	38	Yb I $5p^5(^2P_{3/2})6s^2 5d[3/2]_1 \rightarrow 5p^6 6p(^2P_{1/2})$ (18.62)
22	19.32	16	Yb I $5p^5(^2P_{3/2})6s^2 5d[3/2]_1 \rightarrow 5p^6 4f^{13}6s^2(^2F_{7/2})$ (19.32)
23	21.30	16	Yb I $5p^5(^2P_{3/2})6s^2 5d[1/2]_1 \rightarrow 5p^6 6s$ (21.38)
24	21.96	15	Yb I $5p^5(^2P_{3/2})6s^2 5d[3/2]_1 \rightarrow 5p^6 6s$ (21.98)
25	22.97	1	
26	24.26	3	Yb I $5p^5(^2P_{3/2})6s^2 7d[1/2]_1 \rightarrow 5p^6 6s\ ^2S_{1/2}$ (24.31)
27	27.33	3	Yb I $5p^5(^2P_{1/2})6s^2 5d[3/2]_1 \rightarrow 5p^6 6s$ (27.04)

a) Absolute energy uncertainty of ±0.04 eV.
b) Corrected for 1/E transmission dependence of analyzer - Peak 10 = 100.
c) Based on the energy levels given in Refs. 13 and 20. The value in parenthesis is the optical value from these sources; where more than one final state is indicated, the average value has been given. In addition to the states listed, states of configuration $5p^64f^{13}6s5d$ could also contribute to peaks 19-22.

Table 2. Energies, Intensities, and Assignments of Peaks Seen in the Ejected Electron Spectrum of Ba.

No. of peak	Kinetic Energy[a] (eV)	Relative intensity[b]	Observations, assignments[c,d]
1	5.80	28.0	R
2	5.85		R } $C_{i,j}$
3	5.93		
4	6.09	20.1	R
5	6.10		R
6	6.31	4.	R
7	6.43	30.	R, C_h
8	6.57	6.	R
9	6.76	11.	R
10	6.81		R } C_g
11	6.95	6.	R
12	7.06	40.	R } C_f
13	7.29	4.	
14	7.48	78	R, C_e
15	7.58	95	R, C_d
16	8.31	53	R, C_c
17	8.41	13.	R
18	8.65	19.	R
19	8.82		R
20	9.10	14.	
21	9.29		R
22	9.55	100.	R, $C_{a,b}$
23	9.88	16.	R
24	9.99		R, $5p^5 6s^2 5d\ {}^3P_1 \rightarrow 5p^6 6p\ {}^2P_{3/2}$ (9.9)
25	10.42	14	
26	10.63		R
27	11.09	15	
28	11.22		R
29	12.00	6	$5p^5 6s^2 5d\ {}^3P_1 \rightarrow 5p^6 5d\ {}^2D_{5/2}$ (11.96)
30	12.10	7	R, $5p^5 6s^2 5d\ {}^3P_1 \rightarrow 5p^6 5d\ {}^2D_{3/2}$ (12.06)
31	12.71	58	R, $5p^5 6s^2\ {}^3P_1 \rightarrow 5p^6 6s$ (12.66)

No. of peak	Kinetic energy[a] (eV)	Relative intensity[b]	Observations, assignments[c,d]
32	13.00	3.	R
33	13.25	7.	R
34	13.54	5.	R
35	13.81	8.	R
36	13.96		R
37	14.12	28.	R
38	14.39	3.	R
39	14.73	10.	R
40	14.91	26.	R
41	15.27	22.	R
42	15.53	1.	R
43	15.72	3.	R
44	16.14	18.	R

[a] Absolute energy uncertainty of $\pm$ .09 eV

[b] Corrected for 1/E transmission of analyzer. Peak 22 = 100.

[c] R indicates a BaII energy level observed by Roig[15] that is capable of producing an Auger electron of this energy. C_s indicates series limits observed by Connerade et al.[14] which could also result in the same Auger decay; the s subscript indicates the series in Ref. 14.

[d] Assignments based on the optical values from Refs. 14 and 32; optical value is in parenthesis.

FIGURE CAPTIONS

Figure 1. Ejected electron spectrum of Yb following excitation or ionization of a 5p electron.

Figure 2. Ejected electron spectrum of Ba following excitation or ionization of a 5p electron.

Figure 3. Energy level diagram depicting the various excitation and decay channels discussed in the text, M = Yb ($5p^6 4f^{14} 6s^2$) or Ba ($5p^6 6s^2$).

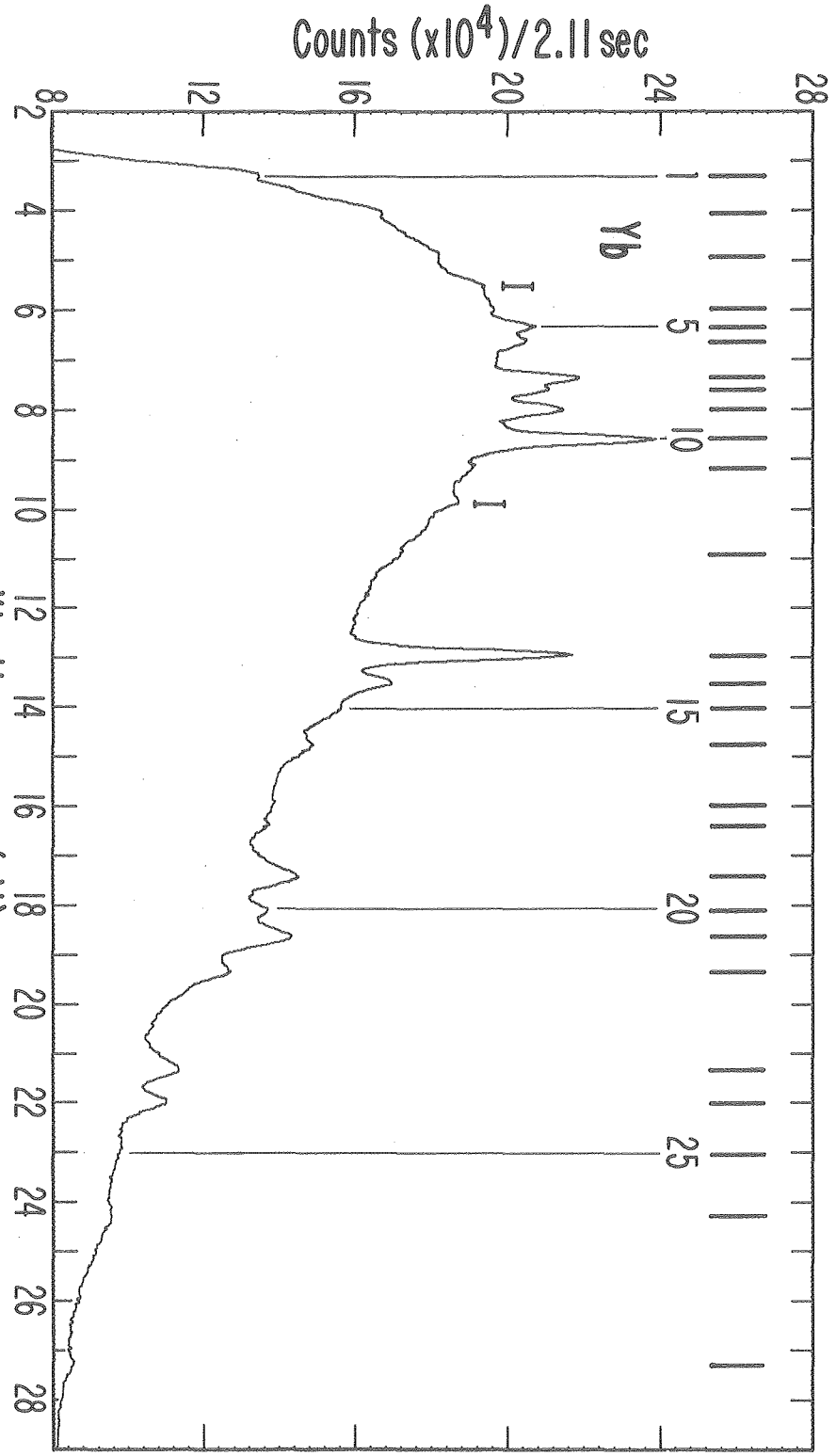

Fig. 1

XBL 763-2573

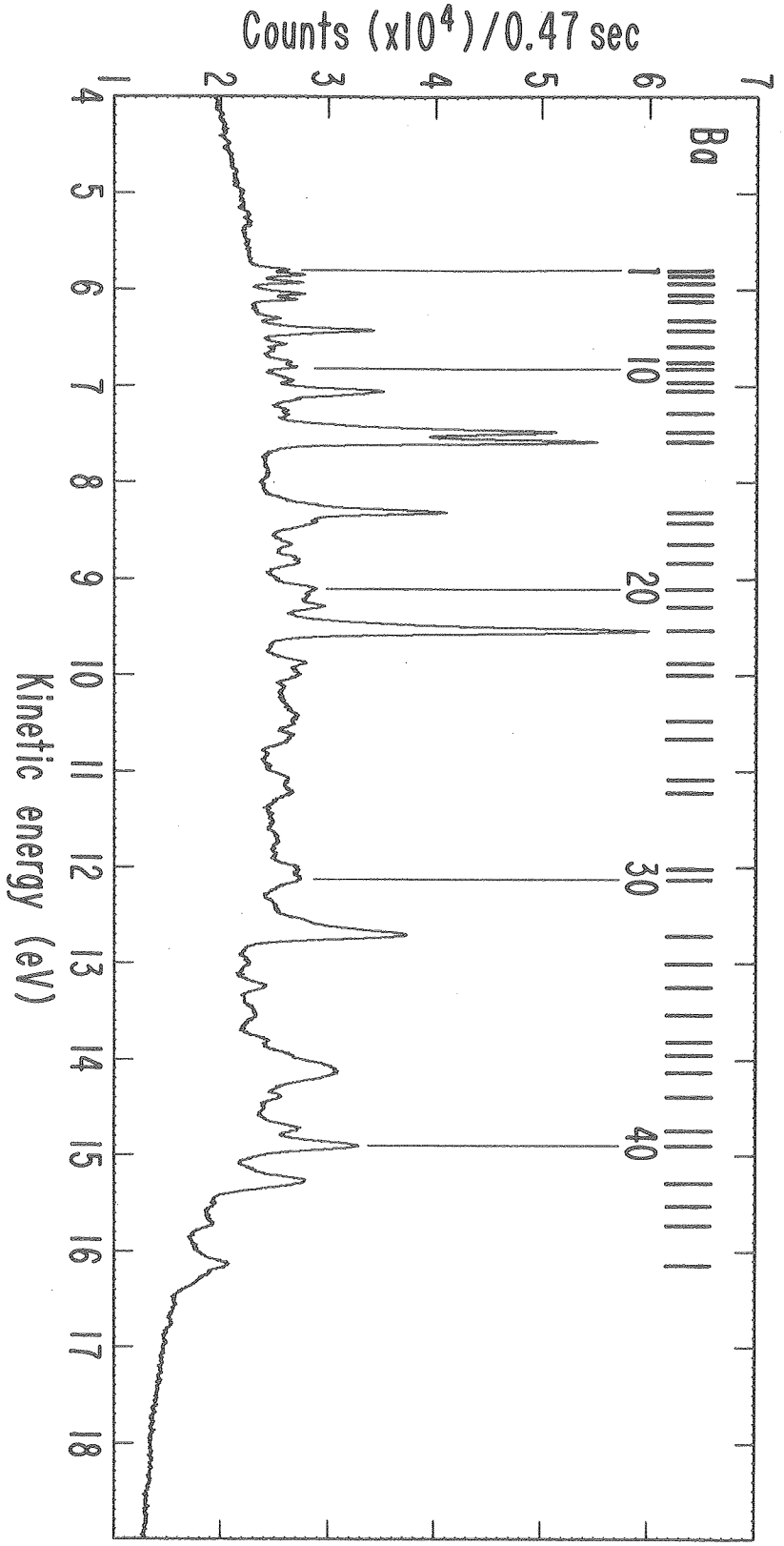

Fig. 2

XBL 763-2476

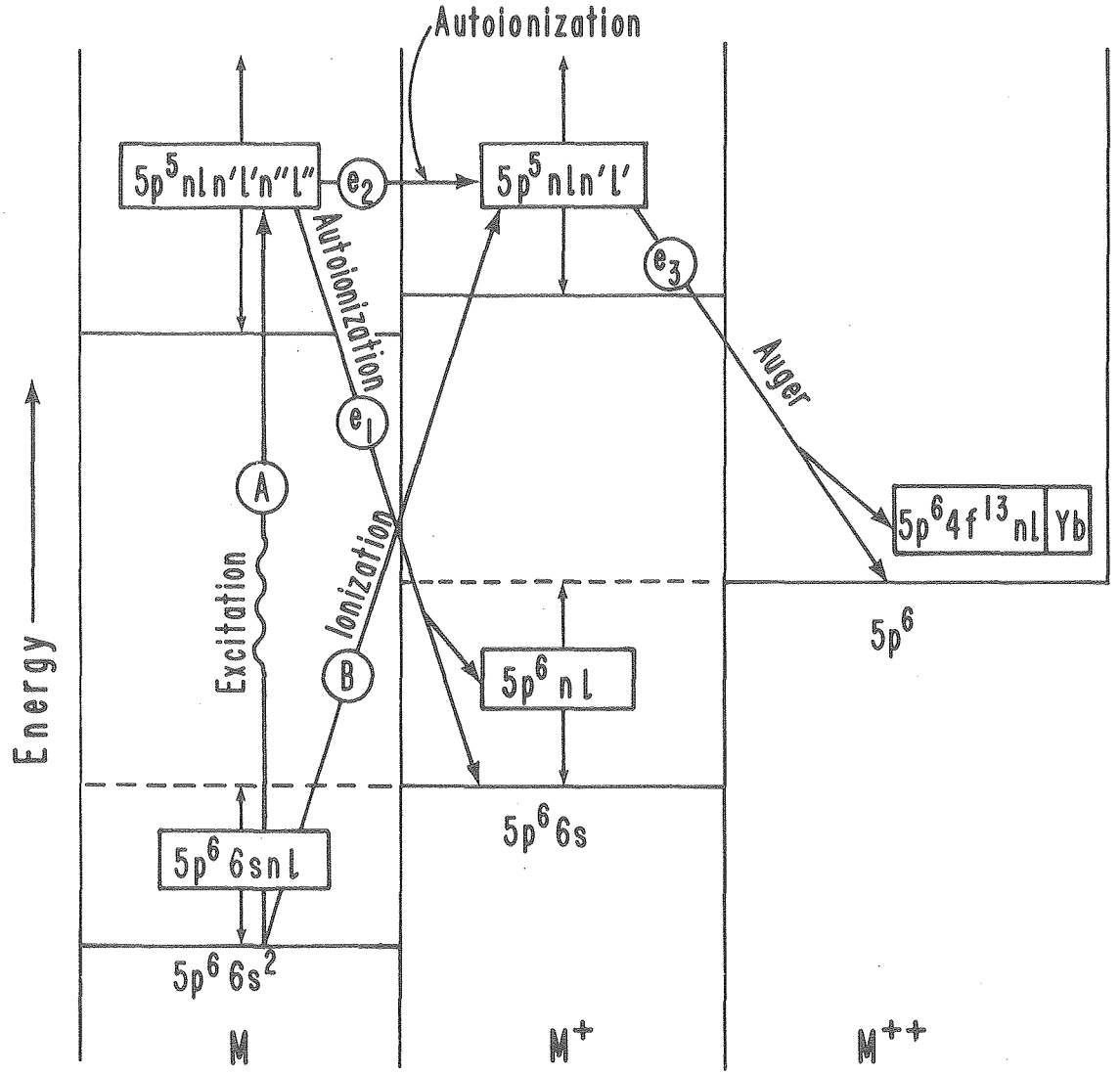

XBL 794-1342

Fig. 3

ACKNOWLEDGEMENTS

The material in this thesis contains contributions from many sources. I would like to take this opportunity to remember and thank the many people who supported and encouraged me in this effort and whose presence helped to make it a very rewarding experience.

First of all, I would like to acknowledge the help of my family and in particular my parents, who have always encouraged my graduate education. However, I still don't think they believe me to be much of a threat to them at pinochle.

I would like to thank my research director, David Shirley, for providing an atmosphere in which it was possible to carry out state-of-the-art research. His busy schedule as head of MMRD left him less time than he would have liked for research-related activities; when time permitted, discussions with him showed a keen scientific insight and proved very rewarding. He encourages independent and original action and rarely imposed his desires, except in-certain-instances.

The success of many of the experiments described here would not have been possible without the expert and enthusiastic support of the technical staff at LBL. In matters of trouble shooting electrical problems, Joe Katz has no peer; I know of no other person who you could call up late at night with a potentially disastrous problem and who could tell you which PC board to pull and which op-amp to change. George Gabor was instrumental in the design and fabrication of the TOF analyzer, and Reed Brandon assisted in much of the assembly. The advice of Dick Escobales and Warren Harnden proved invaluable as far as mechanical

design problems were concerned. Gene Miner managed to make a half-decent draftsman out of me, in spite of myself. Ed Voronin, Larry Ornelas, and Charley Taylor machined and advised on the machining of many of the mechanical parts used in this work.

Despite our rocky beginning, most of the staff at SSRL were very supportive. In particular, I would like to single out Ben Salzburg for always taking an interest in the success of all the experiments and for going to great lengths to see that they worked.

In a group as large and diverse as ours, I've had the pleasure of meeting and working with a great number of interesting people. In the process of initiating gas phase VUV research at SSRL, Mike White, Erwin Poliakoff and I had to overcome many difficulties; I would like to thank these gentlemen for their assistance and their friendship. Lately, Steve Southworth has proven to be a worthy addition to our little group, and with the aid of Dennis Lindle and Paul Kobrin should be able to uphold our "tradition". I owe a debt to Dr. Shuit-Tong Lee for introducing me to research and to Dr. Geoff Thornton for providing able assistance under difficult circumstances. Special thanks go to Dennis Trevor and lately to Jim Pollard for providing invaluable technical advice in many diverse areas. It has also been my pleasure to work with visiting scientists: Prof. Eckart Matthias, who actually got us started at SSRL, Prof. Osama Daboussi, and recently Dr. Vic Rehn. Other people who I have associated with in various capacities and would like to remember include Dr. Rich Martin, Dr. Sefik Süzer, Dr. Bernice Mills, Dr. Rick Streeter, Dr. Read McFeely, Dr. Steven Kowalczyk, Dr. Jo Stöhr, Dr. Paul Wehner, Dr. Stan Williams, Prof. Rand Watson, Mr. Dave Denley, Mr. Ken Mills,

Mr. Steve Kevan, Mr. Rich Davis, Mr. Jim Tobin, Mr. Chris Parks, and Danny (the accountant) Rosenblatt.

I would like to thank Crystal Llewellyn for rushing through many orders for me, Jerry Miranda for able assistance in preparing many of the illustrations included here, and Frances Cotter for typing much of this manuscript.

Many friends have helped me by boosting my morale when it needed it and coming to my aid when necessary. I owe a lot to John Neal for taking care of my dog when I was at SSRL and being a trusted advisor at home. I would like to thank the people who let me stay in their homes during my SSRL ventures; the people at Four Oaks, Michal J., Michael O., Joani, and Mary Mullen; Phil and Jesse Moon-Cook; and Steve Beitler. I would like to thank Jeff and Nancy Millman and John and Cindy Courtright for just being them.

I have reserved this final space to thank two beautiful ladies, Mrs. Wini Heppler and Mrs. Karen Janes. They form the nucleus of our group and somehow manage to hold everything together. Without them many deadlines would not have been met and the atmosphere would not have been nearly as cheerful.

. . . . . and of course, thank you Dirac.

This work was supported by the Division of Chemical Sciences, Office of Basic Energy Sciences, U.S. Department of Energy, under contract no. W-7405-Eng-48.

Some of this work was performed at the Stanford Synchrotron Radiation Laboratory which is supported by the NSF grant no. DMR 73-07692 AO2, in cooperation with the Stanford Linear Accelerator Center.

U.S.GPO:1979-689-058(F)31

TECHNICAL INFORMATION DEPARTMENT
LAWRENCE BERKELEY LABORATORY
UNIVERSITY OF CALIFORNIA
BERKELEY, CALIFORNIA 94720